Development of a Low-Cost Automated Sample Presentation and Analysis System for Counting and Classifying Nematode Eggs

A thesis presented in partial fulfilment of the requirements for the degree of

Master of Engineering

In

Mechatronics

At Massey University, Manawatu,
New Zealand.

Benjamin Pedersen

2017

Abstract

This thesis discusses the concept development and design of a low-cost, automated, sample presentation system for faecal egg counting, and classification. The system developed uses microfluidics to present nematode eggs for digital imaging to produce images suitable for image analysis and classification. The system costs are kept low by using simple manufacturing methods and commonly available equipment to produce microfluidic counting chambers, which can be interfaced with conventional microscopes. This thesis includes details of the design and implementation of the software developed to allow capture and processing of images from the presentation system. This thesis also includes details on the measures taken to correct for the optical aberrations introduced by the sample presentation system.

Acknowledgements

I would like to extend my deepest thanks my supervisors: Professor Robert Hodgson, Professor Donald Bailey, Ralph Ball, Professor Bill Pomroy. The support and guidance you provided throughout this project is greatly appreciated.

I would also like to thank the large number of people who supported and assisted with the development of this project.

Ian Thomas, and all the technicians at massey for their never-ending aid in almost all aspects of this project.

Dr Rob Ward, for his constant support, and for providing a substantial amount of the equipment used in the experimentation.

Dr Katherine Holt, for all pollen related assistance.

Dr Francis Reininger, for his assistance with optics.

Dr Andrea Bubendorfer, and Dr Mike Arnold from Callaghan Innovation, whose expertise and assistance in microdevice fabrication was essential.

Anne and Barb for the crash course on egg counting, and substantial help with egg filtration.

Cameron Jewellery for time and materials supplied at no charge.

Mark Cherrill and the team at the University of South Australia, for their work in developing machined PMMA channels.

The Earle Creativity Trust, and the Ken and Elizabeth Powell Bursary, for the tremendous financial support they provided to this project.

Contents

List of Figures

List of Tables

Chapter 1. Introduction and Background

1.1 Introduction

Pastoral farming represents a considerable proportion of the agriculture, and economy in New Zealand. Nematodes and other helminth parasites have a recognised impact on production in pastoral operations. It is estimated that one-third of New Zealand's sheep production is dependent on anthelmintic-based control of nematode infection [1]. A nematode infection can reduce production and cause harm (potentially death) in vulnerable animals. Diminished production, combined with diagnosis and treatment costs cut into profitability.

Better monitoring of nematode burdens has the potential to reduce the overuse of anthelmintics and help to slow the development of resistance [2, 3], a phenomenon that can be likened to the consequences of the overuse of antibiotics in humans. The cost of anthelmintics to NZ farmers is currently estimated to be at least NZ$100M p. a.

Many methods exist for the detection of a nematode infection. These methods measure the size of the nematode burden on an animal in terms of how many parasites are present. This is normally done through a faecal egg count (FEC), the infection can be quantified by the number of oocysts (cells containing parasite zygotes) present per gram of faeces. A national survey of sheep and beef farmers in 2013 reported that 36% of farmers had used FECs at some stage to assist with their decisions about worm control in their sheep.

Predominantly FECs are conducted manually, most methods share a common set of steps which differ in implementation. Typically, faeces are: collected from an animal, transported to a lab, filtered by some means, placed into a counting chamber, and manually inspected. From sample collection to disposal, all stages require the services of a competent technician. To determine treatment options the result of a FEC must then be interpreted. A FEC provides information about the severity of an infection, but no other information is obtained. Additional processes must be performed to collect information about the species of the parasites present, increasing both costs and turnaround time.

Some work has been done on the detection and classification of nematode eggs using image processing [4-7]. These studies include both high and low resolution approaches to nematode egg detection and counting. When combined with microfluidics, image

processing may provide the foundations for a simple low cost automated assay for performing FECs.

This thesis will primarily discuss the development of a low-cost image processing and optofluidic based assay for the detection, feature extraction, and classification of nematode eggs. Other applications are also briefly discussed.

1.2 Research Aim

The aim of this research is to develop a low-cost automated sample presentation system for digitally imaging nematode eggs to facilitate subsequent counting and classification. There are several aspects to this system which include:

- Sample preparation and filtration
- Sample presentation mechanism
- Image acquisition process
- Feature extraction

A successful conclusion to this research will be observed when an automatic image presentation system, which produces images of suitable quality for feature extraction has been produced. This system must not substantially increase on the costs of current manual techniques while reducing operator involvement.

The quality of the digital image from the system will be assessed by examining the similarities of features extracted from images produced with the system described, and those collected manually.

1.3 Thesis Outline

Chapter One outlines the problem being solved, current methods, and technologies with possible applications to the problem.

Chapter Two provides a broad overview of the design concept which was developed, its components and describes some of the challenges presented.

Chapter Three details some of the physical principles to be considered in the development of the system.

Chapter Four discusses the manufacturing methods investigated for producing low cost microchannels to meet the system requirements.

Chapter Five describes the software developed for automation, data collection, image processing, and analysis.

Chapter Six is a summary of the work done, conclusions, discussion, and potential future work.

1.4 Problem Background

1.4.1 Nematology

As stated, parasitic infections in herd animals reduce production and profit in pastural farming operations. Treatment through anthelminthic medication, and diagnosis through FEC can be expensive.

Nematology is the study of nematode worms, which are a type of helminth parasite. These parasites are found in a variety of ecosystems, in this case they inhabit the digestive system of a host animal. Nematodes are considered parasites as for at least part of their life cycle, as both their environment and nutrition are provided by a host animal. Not all nematodes are parasitic to animals. According to [8] nematodes may be the most significant parasites in countries with climates like New Zealand.

A typical adult nematode can range from 1mm up to 8mm in length, they contract and expand their muscles sinusoidally to move through fluids, leading them to be considered aquatic animals.

1.4.1.1 Life Cycle

Nematodes have a six-stage life cycle (seen in Figure 1-1), and reproduce sexually. As such they are split into two distinct genders, with males containing the organs necessary to fertilise females. After copulation females produce eggs which typically contain a single embryo. Once the embryo has developed it will move into its four larval stages (L-1 to L-4), depending on species one of these will be the infective stage. The infective stage, is the stage in which a nematode can infect a host. Typically, an intermediate host will be infected by the first stage, while the definitive host can be infected by any of the first three stages. For a given species of nematode, the infective stage is the stage at which it infects a definitive host [8].

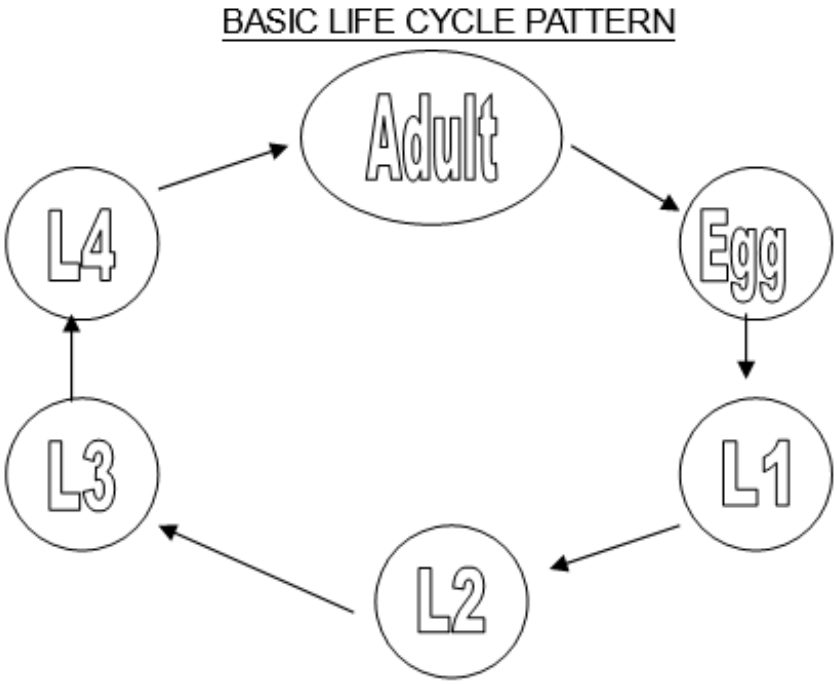

Figure 1-1, Nematode Life Cycle. [8]

As the nematode develops, it sheds its cuticle between larval stages. Between each growth stage there is a period of rest, followed by moulting. A nematode is considered an adult once it has passed through all the larval stages. The adult stage of a nematode will exist within a definitive host, however the larval development can occur in another environment.

Nematodes in the infective stage can gain entry to a host through a number of means. Depending on the nematode multiple means of entry may be available.

- Ingestion from the environment e.g. when an egg is ingested with feed.
- Skin penetration where a nematode can actively penetrate skin or membrane.
- Injection via another animal e.g. mosquito bite.
- Transplacental migration, when an infective stage nematode moves from the mother to child during pregnancy.

Upon entering the host, some nematodes migrate through its body to reach the location where they mature. In most cases this path is from the intestines into the blood stream or lymphatic system. If a nematode enters the host via injection, it can move directly from the blood stream to its destination. Often migration results in nematodes moving through the trachea or pulmonary system.

Not all nematodes migrate within the host, some (which the host ingests) instead inhabit the glands of either the stomach or intestine. A subset of these can pass through the mucosa layer and cause pathological issues as they develop.

1.4.1.2 Nematode Eggs

26

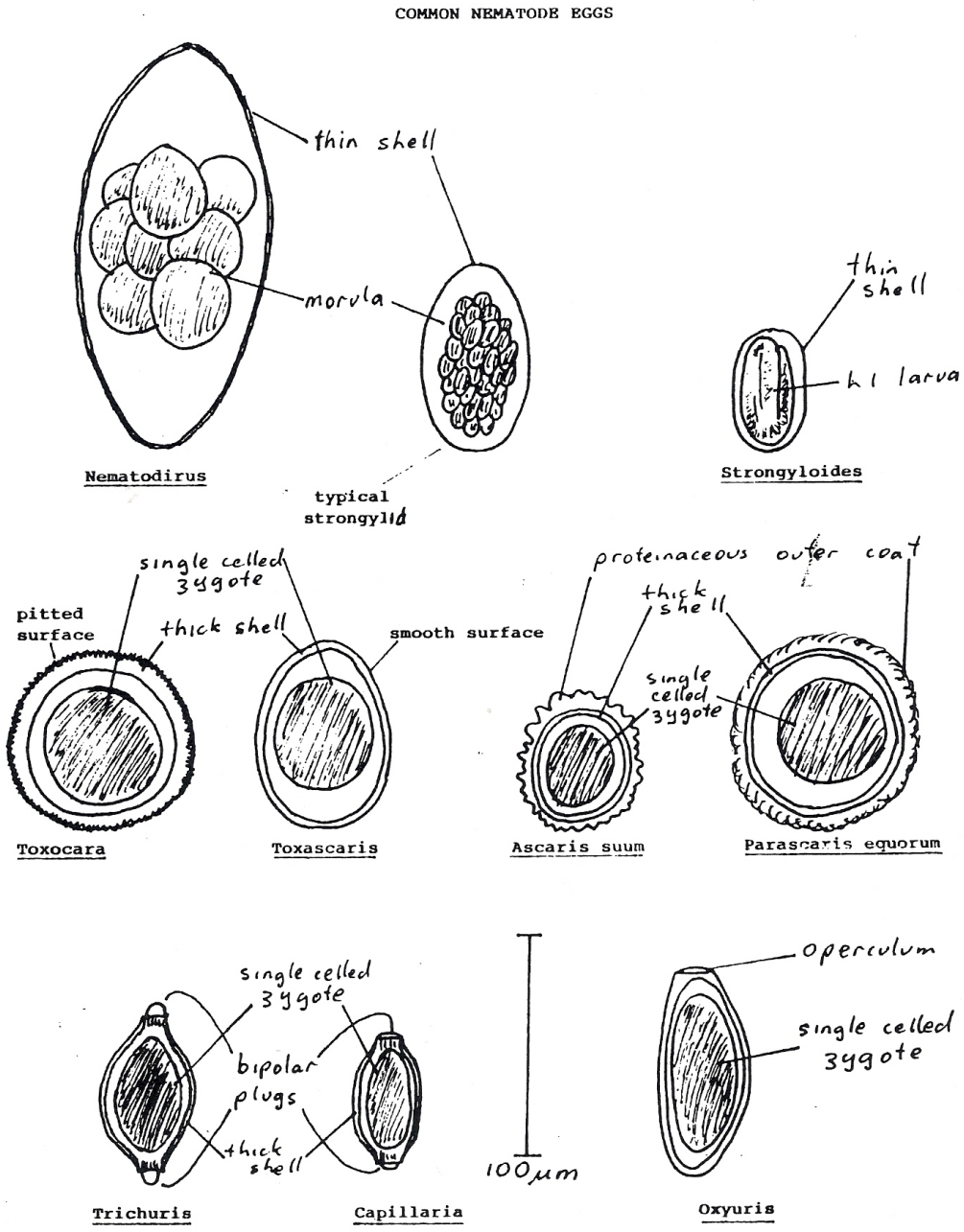

Figure 1-2, Variety of nematode eggs. [8]

Figure 1-2 shows some common nematode eggs. There is a large difference visually between nematode eggs of different species, some feature plug like structures on the ends, while others are simple prolate spheroids. Shell thickness and outer surface also vary between species.

Figure 1-3, Developed nematode larva, large number of internal cells causes the oocyst to appear opaque.

Figure 1-4, Nematode worm inside egg shell.

Nematode eggs also change in appearance as they develop. Figure 1-3 shows how repeated cell division can cause developed eggs to appear opaque. As the egg develops further, a matured worm can be seen formed inside the egg (Figure 1-4), while alive this worm will move within the confines of the egg.

1.4.1.3 Diagnosis

The parasitic burden on an animal can be determined through a FEC. This requires taking a sample of faeces directly from an animal, preparing it with filtration and dilution, then counting the oocysts with a microscope and counting chamber. Methods for performing a FEC range in complexity, duration, and accuracy. The largest difference between methods is how the sample is prepared. In some methods, such as the Kato-Katz method, staining is used to help distinguish oocysts from background objects. In other cases, centrifuge stages are added to improve filtration. The volumes of counting chambers and dilution factors also differ from method to method.

A representative subset of the available FEC assays are considered below. These represent the upper and lower limits of complexity and automation in commonly used FEC assays.

1.4.1.3.1 McMaster Method

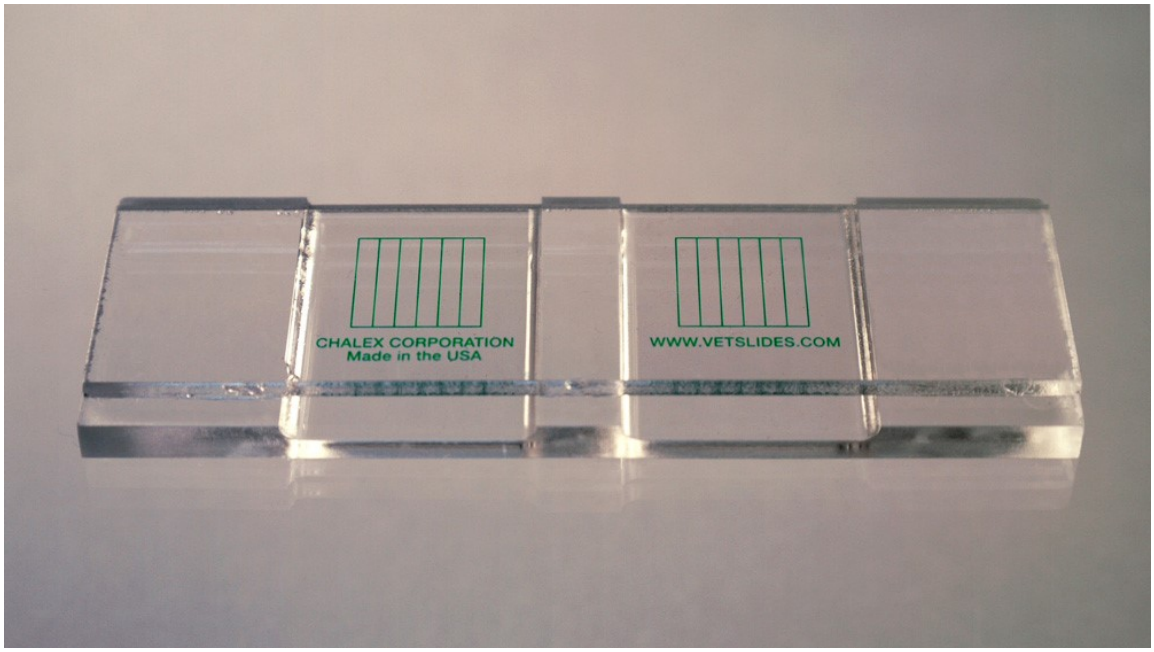

Figure 1-5, McMaster Counting Chamber (300uL) [9]

In the local Massey University School of Veterinary Science laboratory the favoured method for bovine and ovine FEC, is a modified McMaster method. This method is simple and fast at an average of six minutes per sample. Reference [10] shows that the McMaster method has low accuracy when the number of eggs per gram (EPG) is low. If testing for a severe infection, it can be argued that low sensitivity is not important.

The McMaster method takes advantage of the specific gravity of the oocysts. When placed in a saturated salt solution, oocysts will float while detritus will sediment. A microscope focused on the top layer of fluid will image eggs floating in the solution.

Few consumables are needed when performing a modified McMaster test, only the salt solution and pipettes are disposed of between samples. Most equipment, excluding the counting chambers could be found in any well-equipped laboratory.

The modified McMaster method used in the Massey University laboratory is as follows:

1. Faeces are collected from the animal.
2. Two grams of faeces are weighed out.
3. The faeces are strained through a 250µm pore sieve into 28ml of saturated NaCl solution.

4. While stirring, a few millilitres of the solution is pipetted to fill the counting chambers.
5. The counting chambers are viewed on a bright field microscope with 4x objective, and 10x eyepiece magnifications. The number of oocysts in both chambers are counted.
6. The number of oocysts is scaled by 50 for a final EPG figure.

The many modifications of the McMaster method make comparing results between labs difficult; subtle variations in technique may exist between laboratories and practitioners. For large scale comparative studies to be completed, a standardised method would be more appropriate.

1.4.1.3.2 FLOTAC

Figure 1-6, FLOTAC Counting Chamber. [11]

Like the McMaster method, FLOTAC is a flotation based assay. The major differences between the two are in the salt solutions, filtration process, and counting chamber (seen in Figure 1-6). Figure 1-7, shows the steps in the FLOTAC process. Several centrifuge steps and multiple fluid stages result in longer sample times. The longer processing time is offset by a much greater counting chamber volume of 5mL, and higher sensitivity.

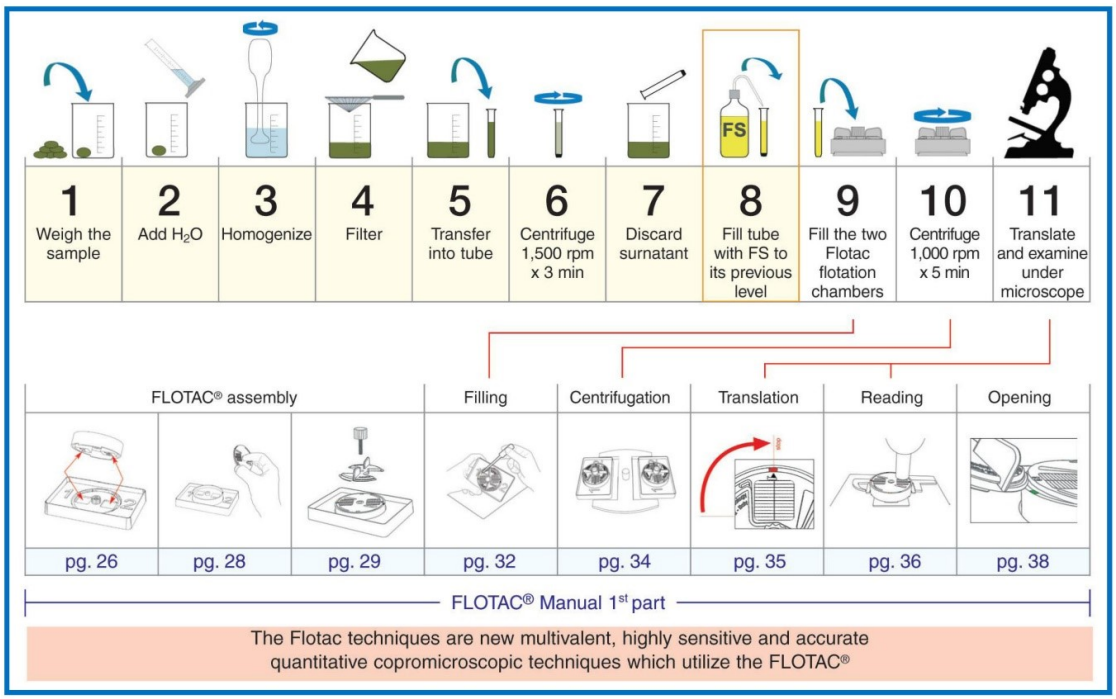

Figure 1-7, FLOTAC steps. [12]

1.4.1.3.3 FECPAK G2

Figure 1-8, FECPAK G2 complete unit. [13]

FECPAK G2 is another flotation based assay. The major advantages are, a set of equipment designed specifically for performing FECs (seen in Figure 1-8), and an

automated image capture device. Sample preparation is simplified through a set of vessels designed to aid in filtration. Imaging is automated by a device known as a 'MICRO-I', removing the need for a conventional microscope. These simplifications to the FEC process allow for users with a limited background in laboratory techniques to perform tests. The system is marketed as a self-service product, with a subscription business model.

The FECPAK G2 process is as follows:

1. Faeces is weighed into a bag
2. Water is added to the bag, which is then mixed to homogenise the solution.
3. This solution is added to a curved container.
4. The container is drained to sediment the oocysts.
5. The container is refilled with saline.
6. The saline solution is poured into a measuring cylinder and filtered.
7. Filtered solution is pipetted into a cuvette.
8. The cuvette is loaded into a cassette for imaging in the MICRO-I device.
9. The solution is imaged, and the images uploaded for analysis.
10. After analysis, the user receives an egg count via email.

1.4.1.3.4 Evaluation

One disadvantage of flotation based assays is damage to the oocysts. In saturated salt solutions, the osmotic gradient will eventually cause nematode eggs to implode, as such samples must be prepared and counted within a short period.

Study [14] is a detailed cost comparison between the Kato-Katz method (a staining based approach to FEC) and FLOTAC, in the context of human FEC. The results of the study show a full FLOTAC test can take up to 28 minutes (this period includes sampling and transport). The study explains that the largest cost factor is operator salary, highlighting potential cost benefits from automating aspects of the process.

Study [10] is a comparison between the McMaster method, FLOTAC, and FEKPAK. The results show that FLOTAC has a higher sensitivity at low egg counts, and an overall lower variance. As the volume of the McMaster counting chamber increases, the variance between tests decreases. This indicates that test accuracy is connected to sample volume.

In the case of the Kato-Katz method, [15] found the reproducibility too low to recommend it for use in human patient care.

An automated system could offer several advantages over the predominantly manual assays. Digital images of each egg could be stored and possibly utilised for quality assurance, or post processing. Being able to review analysis could assist in quality assurance, and allow for controlled comparative studies. Additional information relating to the development, viability, and taxa of eggs in the sample could also be collected from the same test.

An automated assay which could be performed in the same cycle time as current methods, with reduced operator involvement, while providing additional information about the infection would have considerable value.

1.4.2 Relevant Technologies

Many tools exist which could be applied to FEC. In recent years, developments in digital electronics have resulted in cheaper cameras and computer systems. This section discusses a number of technologies which could be applied in a cost-effective manner.

For the purpose of this discussion the technologies relating to the automation of egg counting have been split into two sections: Image analysis, and image capture. The image analysis section will discuss the methods and tools for extracting information from digital images of nematode eggs. The image capture section will discuss sample presentation methods, and imaging techniques.

1.4.2.1 Image Analysis

As early as 1996, Sommer showed how digital images could be used to detect and classify nematode eggs [4, 5]. He made use of both shape and texture features to determine the taxa of an egg from a single digital image. Since his initial studies a number of different approaches have been attempted. As digital cameras and technology reduce in cost, these approaches may provide a cost-effective means of automating the counting process in a FEC test.

1.4.2.1.1 Detection

Egg analysis from digital images can be considered as a two part problem, the first of these problems is the detection of eggs. Before further processing can be completed, eggs must be located with an image and distinguished from detritus and the background.

Depending on the filtering process a sample may contain numerous objects of varying sizes and morphologies. Exceptionally large and small objects can be filtered by size, and some properties unique to nematode eggs can be used to help distinguish them. The approach shown in [16] makes use of the elliptical Fourier shape descriptor shown in Figure 1-9. This descriptor takes advantage of the characteristic shape of many nematode eggs and provides a simple yet robust tool for discriminating between detritus and eggs.

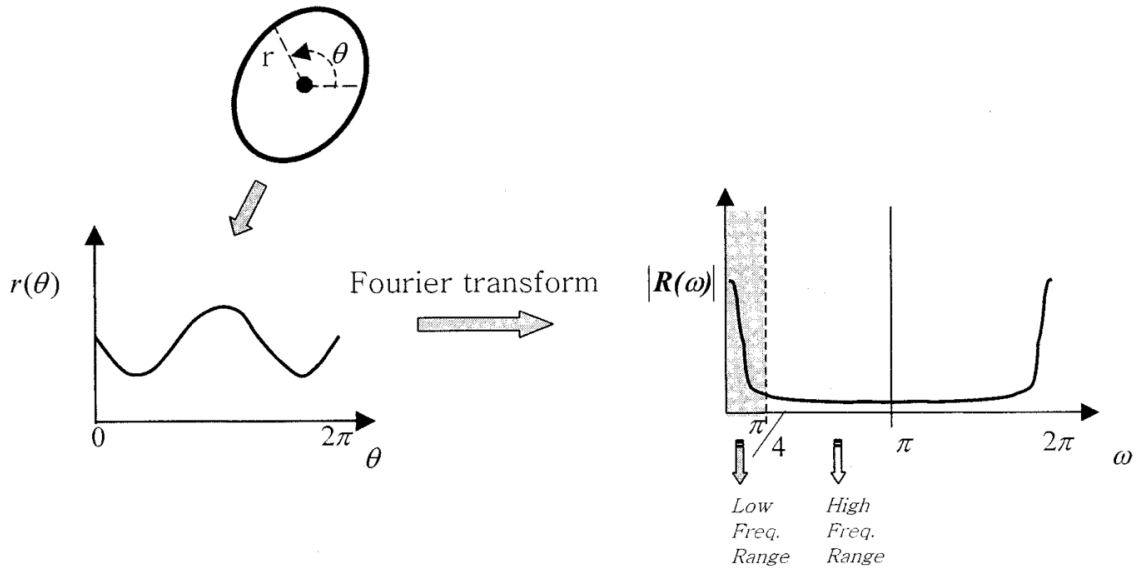

Figure 1-9, Fourier shape features. [16]

1.4.2.1.2 Features

Many other features have been used for detection and classification of nematode eggs. [17, 18] both use shape features for discrimination between taxa, while [7] uses Gray level cooccurrence matrix (GLCM) texture analysis. The GLCM [19] is a matrix produced by calculating how often a pixel of specified intensity occurs relative (spatially) to a pixel of another specified intensity. From the GLCM several features can be extracted which describe the texture, these include, contrast, correlation, and energy. [20] shows yet another approach, by examining the grey level cross sections of the eggs; the grey levels across the minor axis of the egg are measured, as shown in Figure 1-10.

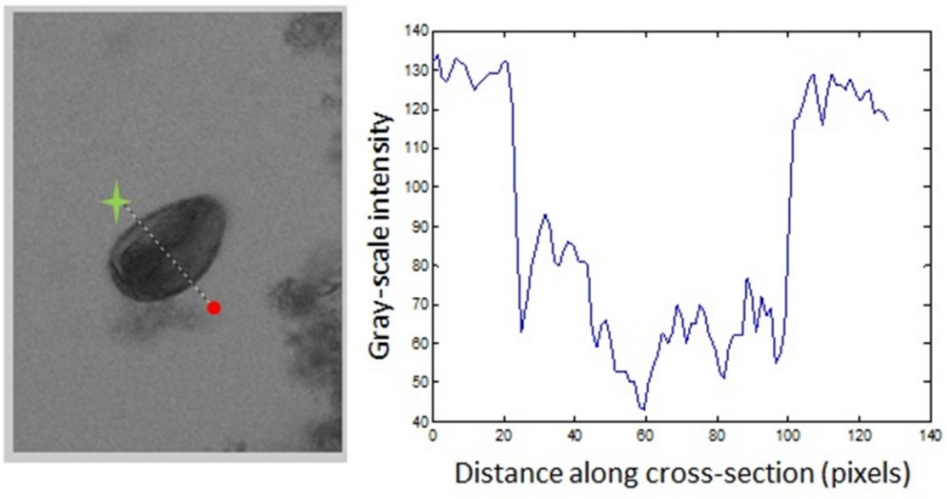

Figure 1-10, Gray level cross-sections from [20].

1.4.2.1.3 Classifiers

Each egg can be characterised by a list of features. With the use of a classifier these features can be used to determine the taxa of the eggs. Classifiers are statistical tools which attempt to map input data to output categories. In machine learning classifiers are often considered a form of supervised learning, meaning that a classifier is provided with a set of labelled data to train on. Once trained, a set of features can be provided to the classifier which will produce a label for the object.

A few different classifiers have been applied to nematode classification, [7] uses a k-nearest neighbours approach, [21] uses a neural network, [22] uses a support vector machine, and [6] an adaptive neuro-fuzzy inference system (a form of neural network which makes use of fuzzy logic). This literature shows that many classifier algorithms have been applied to digital images of nematode eggs. This suggests that an assay based on digital imaging could be utilised to collect species information and while performing a FEC.

1.4.2.2 Image Capture

The collection of images of a suitable quality is important. When processing a sample many eggs will need to be imaged, and to reduce costs the time spent imaging eggs should be minimised. The images captured must also provide enough information for feature extraction and classification. This section discusses several technologies for sample presentation, image capture, and improvements to image quality.

1.4.2.2.1 Extended depth of field

As resolution of an imaging system increases, the depth of field (DoF) will decrease. This means that for objects with a depth greater than the DoF, some part of the object will be out of focus. Extended DoF techniques allow for the collection of information that would typically be outside the DoF. There are a number of methods for doing this:

Wave front coding [23] can be used to extend the DoF through a combination of deconvolution, and modulation of the illumination. Additional elements are placed in the optical system which introduce variation in the optical path. The result is a blurred image with a point spread function independent of defocus. Image processing can be used to remove the constant blur from the image and increase the DoF.

Holography [24, 25] uses a coherent light source and beam splitter to produce a hologram of the object being imaged. Light scattered from the object (known as the object beam) and light separated by the beam splitter (reference beam) are combined on a recording medium to form a diffraction pattern. When the recorded surface is illuminated with the initial light source, a hologram of the object can be produced.

Focal stacking is a simpler technique than the previous two. Images are captured at a number of focal planes passing through the object. The set of these images can be combined through image fusion to form compound images, or used to build 3D models (shown in Figure 1-11).

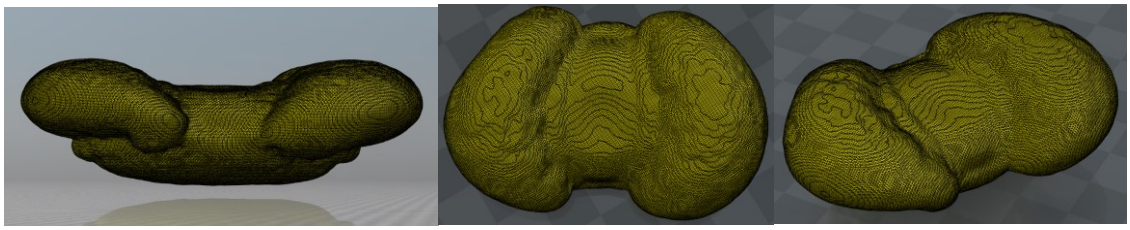

Figure 1-11, 3D surface from confocal image stack of Prumnopitys pollen.

Image fusion is the process of combining multiple images to form a single image containing the relevant information of the set. The wavelet-based fusion approach involves taking the wavelet transform of each image in the focal stack, selecting the relevant coefficients, and then performing an inverse transform to produce a fused image. Further details on this are described in Chapter 5.

1.4.2.2.2 Automatic Microscope

Collecting focal stacks of microscopic objects requires a machine which can move the specimen being imaged through the focal depth of the imaging system. Automated microscopes such as the one described in [26] manipulate the specimen with motors and actuators. These systems can locate and scan microscope slides without constant input from an operator, large sets of images can be acquired of all the objects on a slide. This technology could possibly be adapted for sample presentation and imaging in a FEC application.

1.4.2.2.3 Slanted microscope scanning

The three axis control needed for a focal stacking automatic microscope requires many of moving parts and high mechanical precision. [27] suggests a simple method for reducing the number of axis required when scanning. Rather than moving to an object and then moving the focal plane vertically through it, Fan and Bradley suggest tilting the imaging system relative to the specimen plane. A small tilt angle means that as the object moves through the field of view (FoV) of the imaging system, it will be imaged in a number of slices. The advantage of this is the removal of the vertical axis, and a reduction in scanning time as the object can be imaged in a single pass. Introducing a tilt between the imaging system and the microscope slide (or surface being scanned) will introduce optical aberrations to the imaging system [28, 29]. More detail on these aberrations is given in Chapter 3.

1.4.2.2.4 Slanted Microchannel

A tilted slide scanning system relies on mechanical movement of the specimen relative to the imaging system. The mechanical system has a number of limitations in: accuracy, repeatability, and settling time. A logical step forward in specimen presentation is the tilted microchannel. The tilted microchannel (shown in Figure 1-12) involves moving objects suspended in fluid through a small channel. The channel is tilted relative to the imaging system. As an object moves across the field of view it will be imaged a number of times, creating a focal stack.

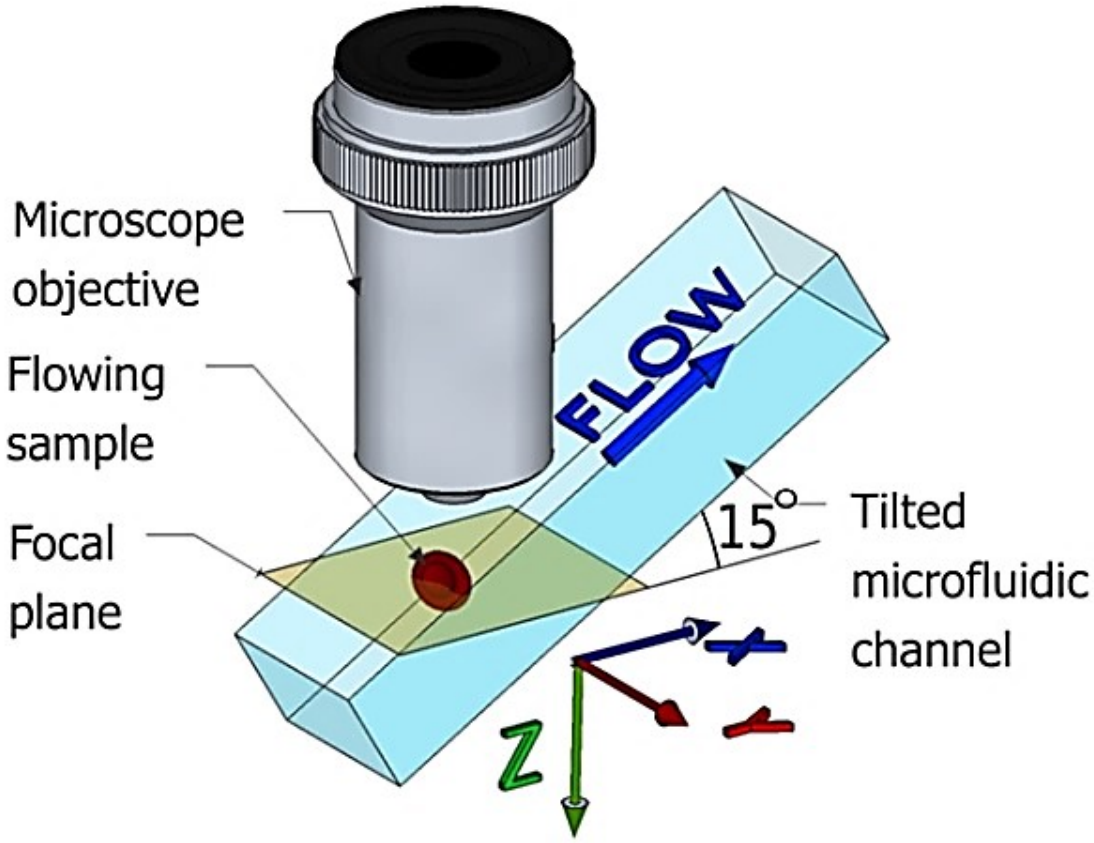

Figure 1-12, Slanted microchannel. [30]

The tilted microchannel was first proposed by [31] for use in cell analysis. Since then continued development has occurred in extended DoF, and 3D imaging applications [24, 30, 32, 33]. The tilted microchannel represents a compromise where the complexity of the system is decreased, in exchange for the addition of a microfluidic channel. The channel replaces the slide (or counting chamber) for sample presentation, and removes the need for high precision actuators. The microchannel dimensions enforce a fixed upper limit on the size of objects which can be imaged, blockages must be avoided as they can result in irreparable damage to the fluidic device. A pumping system is required to flow objects through the field of view, this is discussed in detail in Chapter 2. The tilted microchannel also introduces the same optical aberrations as the slanted scanning microscope, an in-depth description can be found in Chapter 3. As most FEC methods already involve filtration and suspension of the eggs in fluid, this microfluidics could easily be integrated into existing assays.

1.4.2.2.5 Varifocal Lenses

Rather than tilting the imaging system to eliminate the vertical axis when collecting focal stacks, an imaging system with a variable focal length could be implemented to the same effect [34, 35].

1.4.2.2.6 Flow Cytometry

As the name suggests, flow cytometry is the study of particles in fluid flows. There are many different approaches to this, some use lasers and analyse the light scattered from the particles others, such as the Coulter counter measure impedance changes as objects pass through a small pore. The Coulter counter works by immersing objects in an electrolytic fluid, then placing a potential difference across the fluid. The fluid is separated into two chambers of different potential, with a small hole between them. When an object moves through the hole the resistance between the two chambers is changed measurably. The change in resistance can be used to describe the object. Flow cytometry has been applied to nematology with a reasonable level of success [36]; imaging flow cytometry may be a suitable tool for FEC assays.

1.4.2.2.7 Fluorescence

[18, 37], discuss the use of fluorescence tagging in nematode egg detection. Some proteins bond to specific eggs and fluoresce under certain lighting, allowing eggs to be easily discriminated from the background and detritus. The downsides to this are that it adds complexity to the optical system and additional steps to a FEC procedure. As the aim is to produce a low cost system, it may be advantageous to avoid the use of fluorescence.

1.4.2.2.8 Portable imaging system

Some recent work has shown the advantages of a portable cytometer, and how cell phone cameras can be used as cheap alternatives to computers and external digital cameras [18, 38]. This may be a valuable way of further decreasing costs and improving portability. Development of software for a smartphone platform may increase the complexity of the system design. Given the time constraints of this project, this may be considered after feasibility has been confirmed.

1.5 Conclusions

The diagnosis and treatment of nematode parasites is important to the New Zealand economy. A number of diagnosis tools currently exist, however those with the most usage

are predominantly manual. These manual methods vary in both efficacy and duration. The duration is governed by the length of the filtration and counting processes. The time taken to complete a test determines most of the cost due to the technician's salary. Provided the capital expenditure to do so is not too large, automating some of these steps will create cost reductions.

An automated assay based on digital image processing may also provide additional information beyond the EPG count. Literature on the detection and classification of nematode eggs from digital images suggests that, provided images of suitable resolution are obtained, taxa information could also be collected. A number of approaches to sample presentation are also available. A tilted microfluidic channel could be implemented as a simple replacement for a counting chamber, provided the devices can be manufactured cheaply.

The next chapter will discuss how this information was applied in developing a low cost, automated method for the detection and classification of nematode eggs in faeces.

Chapter 2. Proposed System Design

2.1 Introduction

This chapter discusses the chosen concept selected for the development of a low cost automated FEC system. A list of constraints is presented, these are based on the McMaster method, and are used to benchmark the systems performance. Each of the components in the system are described, and reasons for their selections are given. Finally, the challenges in the design and how they were met are described.

2.2 Constraints

Of the three methods which were analysed in depth (FECPAK, FLOTAC, McMaster) McMaster had the lowest sensitivity and highest variance, this represents a good baseline of performance for a development system, as it is widely used. Based on this, the following constraints for the prototype system were developed:

- The system should require no user involvement in sample imaging, counting, and classifying.
- The system should process the same volume of fluid as a McMaster test in same period that is:
    - 300µL
    - 10 minutes (this constraint has been relaxed to 10 minutes for development, as it is not critical in assessing the performance of the imaging method.)
- The system should image all objects in the egg size range (60-200µm major axis)
- The system produce digital images of sufficient quality in resolution and focus, to enable the determination of taxa.
- Based on the images, the system should determine if an object is an egg.
- The capital cost of a complete system must not exceed that of a typical laboratory microscope.

2.3 Design

2.3.1 Components

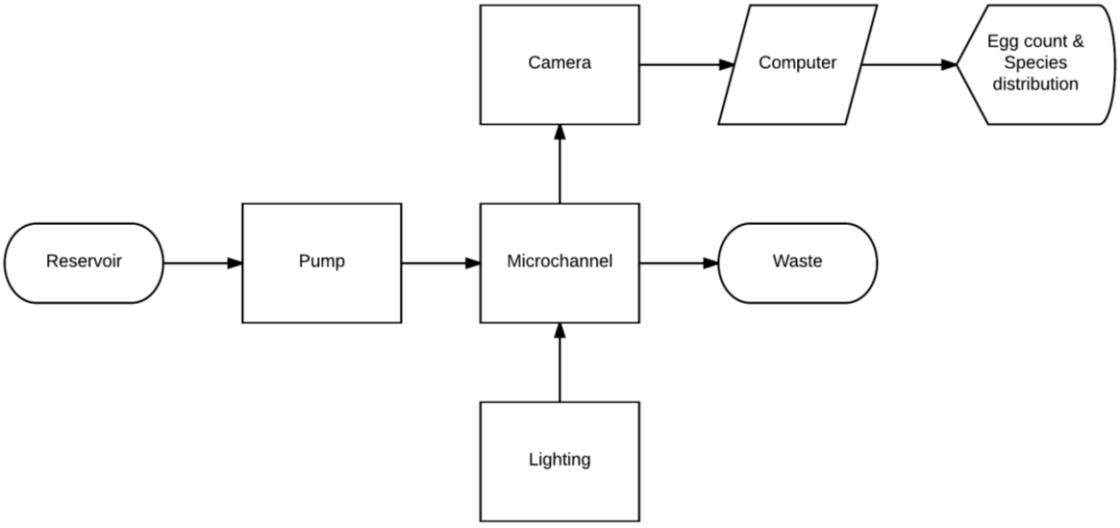

Figure 2-1, System block diagram.

Figure 2-1 is a block diagram of the system, each component will be discussed in detail in the remainder of this section.

2.3.1.1 Reservoir

Figure 2-2, Sample tube reservoir. [39]

PCR (Polymerase Chain Reaction) 5mL tubes were selected as sample reservoirs for the system. They were selected as they provide the same sample volume as a FLOTAC test. PCR tubes are also cheap, disposable, and common place in most laboratories. When interfaced with the pumping mechanism, fluid from the PCR tube flows into the microchannel, presenting any objects in solution to the imaging system. To simulate a McMaster test the reservoir was filled with 300µL rather than a full 5mL.

2.3.1.2 Pump

The pumping mechanism for the system is used to move sample fluid from the reservoir through the microchannel. To satisfy this the pump must be capable of constant flow rates as low as 30µL per minute. Disruptions and inconsistencies in flow rate will unnecessarily complicate the imaging process and should be avoided, however an adjustable flow rate is ideal for testing and development. Upon presentation to the camera the eggs in solution must be undamaged. The pump must fit within the budget constraints of the system. The feasibility of the following pump types was assessed:

- HPLC (High pressure liquid chromatography) pumps
- Peristaltic pumps
- Syringe pumps
- Pressure generators

Peristaltic pumps typically produce a pulsed flow profile, which would cause inconsistent imaging as the flow rate would fluctuate constantly. Like positive displacement pumps, peristaltic pumps can damage objects in the fluid. By the nature of how they function, peristaltic and positive displacement pumps are not appropriate for this application.

Syringe pumps typically consist of a leadscrew and electric motor. A syringe is fixed in place, and the piston is attached to the lead screw, as the motor turns, the piston is depressed generating flow. Syringe pump manufacturers claim flow rates in the order of microliters per hour [40], however these are heavily dependent on syringe size and motor control. The NE-1010 syringe pump (seen in Figure 2-2), uses a 200 step per revolution motor, in conjunction with a 1.27mm pitch lead screw. With a drive ratio of close to 2:1 this pump has a minimum step size of 3.18µm. The cross-sectional area of a syringe is usually much greater than a microchannel, meaning that this increment per step is greater in the channel. Low flow rates can be achieved by stepping the motor very infrequently, this would not be suitable for this application as samples need to move through the channel at a constant flow rate.

Figure 2-2, N1010 syringe pump. [40]

A syringe pump with a smaller step size was constructed and tested. This used a 0.5mm pitch lead screw (micrometer barrel), a 200 stepper motor, and a 1/4th micro stepping driver. This system had a step size of 0.625µm. Although capable of small steps, it was found that this pump performed inconsistently, and steps would vary in size. This is believed to be attributable to inadequate mechanical tolerances and the inherent inaccuracy of microstepping.

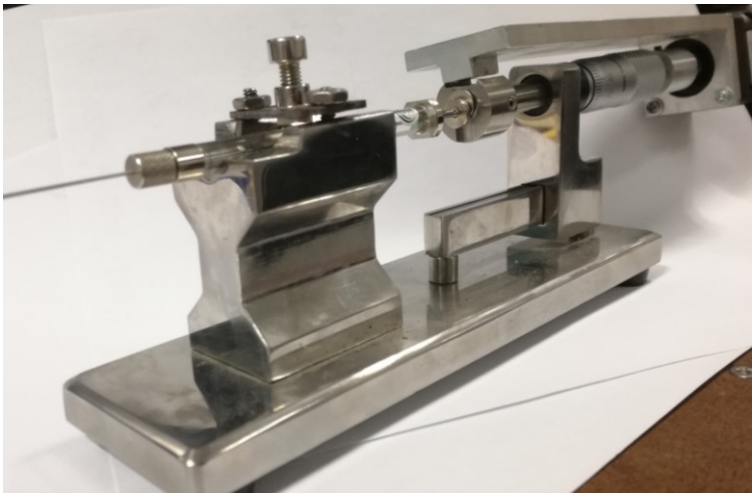

Figure 2-3, Automated micrometer syringe pump.

To avoid the inconsistencies and low precision of a syringe pump system, a pressure generator was tested. The Elveflow AF1 pressure generator is capable of up to 200mbar of pressure with a resolution of 12.2µbar. A pressure increase in a fluid reservoir relative to atmosphere can generate flow through the microchannel. If the pressure differential is constant the flow rate will also be. The AF1 has an adjustable flow rate, making it useful in the development process. The AF1 also interfaces well with PCR tubes providing both a flexible reservoir and flow rate in the desired range.

Figure 2-4, Elveflow pressure generator. [41]

By process of elimination the AF1 pressure generator was selected as the pumping system for the development due to the fact that it exceeds the requirements. For a system tailored to a specific application, the pumping system could be replaced with an elevated reservoir, the same pressure differential could be generated by the difference in height of the reservoir and waste outlet. This would significantly reduce costs.

2.3.1.3 Microchannel

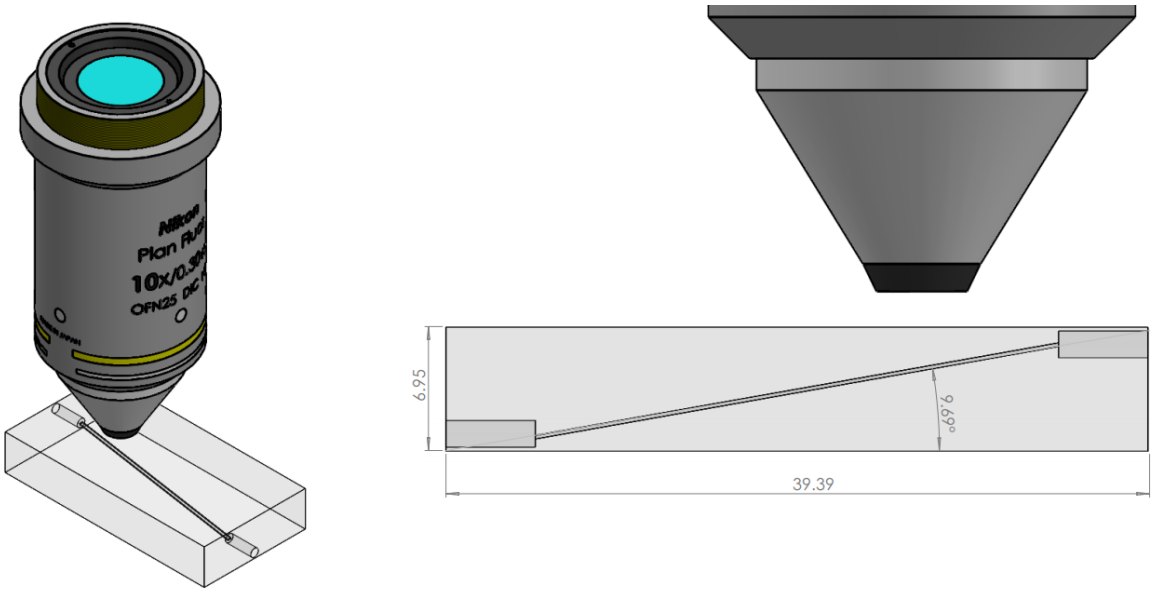

Figure 2-5, Tilted microchannel concept.

A simple titled microchannel was selected for this application, it provides the relative motion between camera and specimen required for focal stacking, while avoiding additional components and complexities. With a tilted microchannel other techniques,

such as hydrodynamic focusing, and motorised camera positioning are not needed. These simplifications help keep costs down, and improve reliability.

The downsides of a tilted microchannel in this application are fabrication difficulties, and the addition of optical aberrations to the imaging system. More details on this are presented in Chapters 4 and 3, respectively.

2.3.1.4 Lighting

For the sake of simplicity monochromatic LEDs were used for lighting. Monochromatic lighting removes chromatic aberrations for the system. LEDs were chosen for their high intensity and the short exposure times required for imaging objects in this application. Further details on this are presented in Chapter 3 (also see Appendix V).

2.3.1.5 Camera and optics

Figure 2-6, IDS USB3 Camera. [42]

The imaging system must adhere to the low-cost philosophy of the system, simple components were chosen, they consist of:

- Monochromatic digital camera
- Finite conjugate objective lens
- Condenser
- Monochromatic LED array

The optical aberrations caused by the tilted channel are dependant of the tilt angle, minimising this is important for producing quality images. The wider the field of view (FoV) the lower the tilt angle needs to be (seen in Figure 2-7 where theta is the tilt angle).

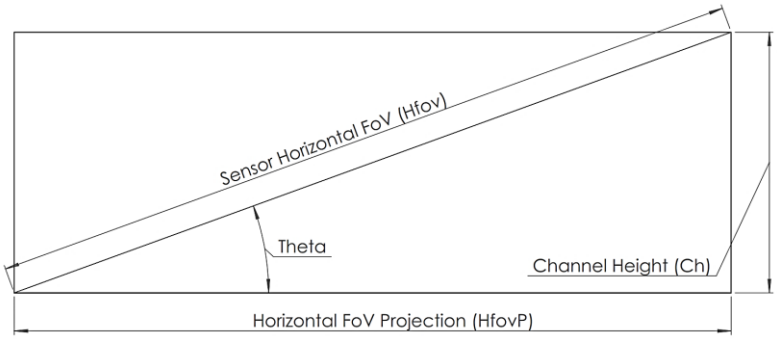

Figure 2-7, Sensor FoV relative to tilt angle.

The higher the field of view of the imaging system, the lower the magnitude of the aberrations. The camera must also have appropriate shutter speed for imaging fast moving objects, and a high enough frame rate to collect focal stacks. The camera should also be monochromatic.

An IDS UI-3360CP-M-GL camera (shown in Figure 2-6) was selected in conjunction with an Olympus 10x objective. The camera's 2:1 aspect ratio sensor is capable of 150fps, and constrains the tilt angle in this application to 11˚. According to [43] a 10x objective is sufficient for the feature extraction of nematode eggs.

2.3.1.6 Computer

An HP Z220 workstation computer was selected for the development of the system. It has performance commensurate with a typical lab computer, and all the required busses for communication with the other components (serial and USB3).

2.3.2 Design challenges

2.3.2.1 Micro channel fabrication

A tilted rectangular channel through a substrate complicates the manufacturing process, but removes the need for a counting chamber. The optical aberrations introduced by the tilted design must also be considered when selecting the channel material.

Placing the channel at an angle through a substrate means that simple top down manufacturing methods, such as conventional or chemical milling are unsuitable. Other techniques such as soft lithography and moulding need to be adapted to produce viable channels. A detailed breakdown of the manufacturing methods considered and their results is given in Chapter 4.

2.3.2.2 Optics

The tilted channel introduces aberrations to the imaging system by acting as a tilted plane-parallel plate. The introduced aberrations have a significant impact on image quality and must be corrected for. Chapter 3 discusses a low-cost solution to this in the given application.

2.3.2.3 Fluid mechanics

Objects flowing through the channel will experience unbalanced forces resulting in rotational motion. This motion causes issues when aligning the focal stack for image fusion. Chapter 3 provides details on this motion and how it can be measured. Chapter 5 shows how this can be partially corrected for though software.

2.3.2.4 Data management

Over 100GB of video can be examined in each run of the machine. For the system to function feasibly this data must be compressed and handled without introducing artefacts, or losing information. A method for handling this volume of data, which exploits the low concentration of egg objects within a sample is presented in Chapter 5.

2.4 Conclusions

A system is proposed, which uses a tilted microchannel and digital camera to collect focal stacks of nematode eggs from a fluid sample. This system uses digital image processing to extract quantitative features from egg images, to determine taxa and viability. The imaging, egg detection, and classification processes are all automated to reduce technician involvement and minimise costs. The system was designed with simplicity in mind so that it could be produced cost-effectively. This simple design represents a trade-off between mechanical complexity and fundamental image quality. The tilted channel meets the need for relative motion between the camera and sample stream, but introduces imaging aberrations which need to be corrected for to recover image quality.

Chapter 3. System Mechanics and Optics

3.1 Introduction

This chapters discusses the physical principles which govern the operation of the concept developed in the domains of: fluid mechanics, optics, and lighting. Fluid mechanics dictate the motion of the objects in the sample stream, while optics and lighting affect the quality of the images created.

Calculations in this chapter are based on the practical test system which was suboptimal, due to the limitations of the channel manufacturing method.

3.2 Mechanics

3.2.1 Introduction

The flow of a sample through the channel is controlled by a pressure generator. The pressure differential across the microchannel generates flow. This flow has a nonuniform velocity profile over the cross-section of the channel. The difference in velocity across an object in the flow stream generates a torque on the object. The torque causes additional motion of the object such as: rotation, tumbling and lateral movement (perpendicular to the direction of flow). The implications of these effects and relevant equations are presented in this section.

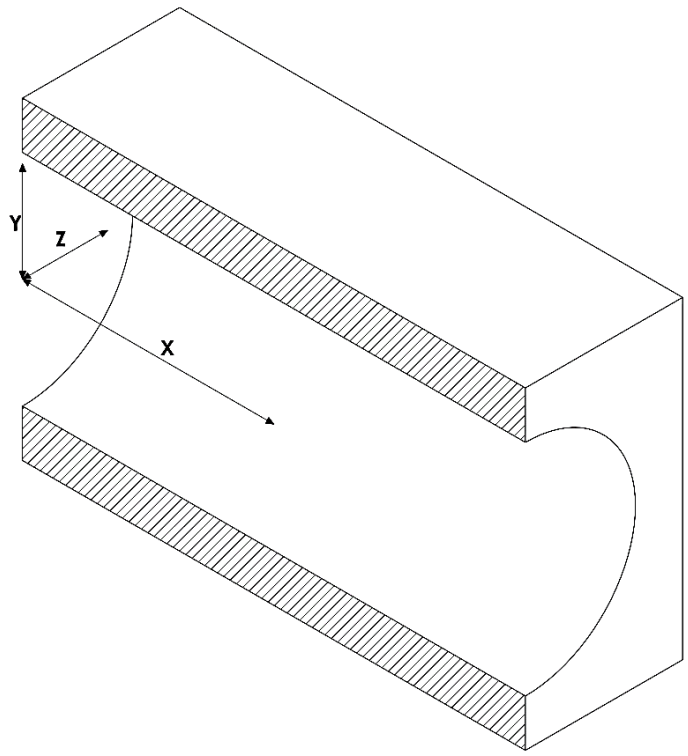

Figure 3-1, Circular channel section view.

Dimension housekeeping (shown in Figure 3-1):

- X-axis: Direction of fluid flow through channel
- Y-axis: 'Channel height'
- Z-axis: 'Channel depth'
- Channel cross-section refers to the YZ plane
- The optical plane can be considered the Z, X plane

3.2.2 Flow Regime

Several factors determine how the fluid flow in the channel behaves. Fluid flow through the channel is driven by a pressure differential. One end of the channel is at atmospheric pressure, while the sample reservoir is pressurised. This difference in pressure causes the sample to flow through the channel at a fixed rate.

The volumetric flow rate Q can be expressed simply as the sample volume V, over the processing period, T.

$$Q = \frac{V}{T} \tag{1}$$

The average linear flow rate u is the volumetric flow rate over the cross-sectional area of the channel.

For a rectangular channel:

$$u = \frac{Q}{Y\,Z} \tag{2}$$

$$u = \frac{Q}{\pi R^2} \tag{3}$$

The Reynolds number is a dimensionless quantity which describes the flow regime. A flow can be turbulent, transitional, or laminar. In microfluidics flows are typically laminar due to the small dimensions, volumes, and flowrates. For Reynolds numbers less than 2000, the flow is considered laminar, and above 4000 the flow will be turbulent. In microfluidics the Reynolds number is often below one.

$$R_e = \frac{\rho u D_H}{\mu} \tag{4}$$

Where ρ is the density of the fluid, and μ the dynamic viscosity. For square or circular channels, D_H (hydraulic diameter) is the width or diameter respectively. For other geometries equations exist to derive the D_H.

An aqueous solution of glycerol was the selected carrier fluid, and the viscosity and density at different mass fractions were obtained. These are listed in Tables 3-2 and 3-3.

Glycerol (%)	15˚C	15.5˚C	20˚C	25˚C	30˚C
50	1.12870	1.12845	1.12630	1.12375	1.12110
49	1.12600	1.12575	1.12360	1.12110	1.11845
48	1.12325	1.12305	1.12030	1.11840	1.11580
47	1.12055	1.12030	1.11820	1.11375	1.11320
46	1.11780	1.11760	1.11350	1.11310	1.11055

Table 3-2, Glycerol solution density, by concentration [44].

Glyc. % Wt.	Temperature (°C)										
	0	10	20	30	40	50	60	70	80	90	100
0*	1.792	1.308	1.005	0.8007	0.6560	0.5494	0.4688	0.4061	0.3565	0.3165	0.2838
10	2.44	1.74	1.31	1.03	0.826	0.680	0.575	0.500	—	—	—
20	3.44	2.41	1.76	1.35	1.07	0.879	0.731	0.635	—	—	—
30	5.14	3.49	2.50	1.87	1.46	1.16	0.956	0.816	0.690	—	—
40	8.25	5.37	3.72	2.72	2.07	1.62	1.30	1.09	0.918	0.763	0.668
50	14.6	9.01	6.00	4.21	3.10	2.37	1.86	1.53	1.25	1.05	0.910

Table 3-3, Glycerol solution viscosity, by concentration. [44]

Friction between the fluid and boundary surfaces causes a velocity gradient in the flow. This is known as shear flow and is shown in Figure 3-4.

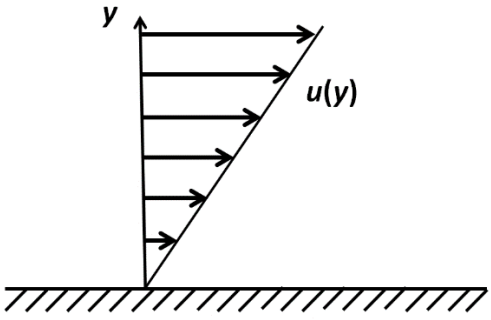

Figure 3-4, Shear flow profile [45].

Laminar flow in a microchannel results a shear profile known as Poiseuille flow (shown in Figure 3-5). The fluid in contact with the channel walls, has zero velocity, while the fluid in the center (farthest from the walls) has the maximum velocity, creating a parabolic profile.

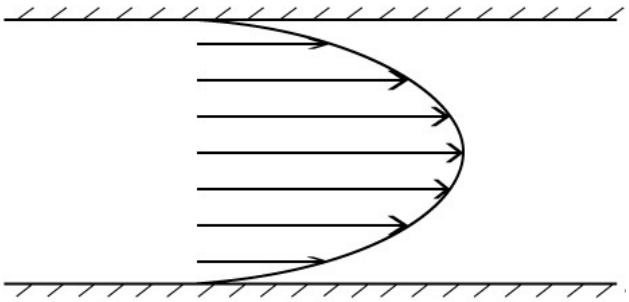

Figure 3-5, Poiseuille flow [46].

Frictional forces cause a pressure drop across the length of the channel. This pressure drop can be calculated as:

$$\Delta P = \frac{32\mu L v}{d^2} \tag{5}$$

Where L is the length of the channel, v is the average linear velocity, and d is the diameter of a circular section.

The linear velocity in the channel is independent of the X axis position, except for at the inlet and outlet regions of the channel, where the Poiseuille profile may not be fully established. The velocity at any point on the X, Y or X, Z planes is a function of the distance from the X axis. This can be expressed as:

$$v_r = \frac{\Delta P(R^2 - r^2)}{4\mu L} \tag{6}$$

Where R is the width of the channel and r is the distance from the center of the channel in the Y, Z plane. The peak velocity in the channel is simply given by.

$$v = \frac{\Delta P R^2}{4\mu L} \tag{7}$$

Shear rate is the rate of change of velocity between layers of fluid. This is at its highest at the channel wall. The shear stress in a fluid is simply the shear rate multiplied by the dynamic viscosity. Shear rate can be calculated by:

$$\gamma = \frac{4Q}{\pi r^3} \tag{8}$$

Or

$$\gamma = \frac{\Delta P r}{2\mu L} = \frac{dv}{dr} \tag{9}$$

3.2.3 Rotation of objects in a flow stream

The velocity profile in the flow stream causes objects to undergo additional motions. For a prolate ellipsoid (such as a nematode egg) the most significant of these is rotation in both the X, Y and Y, Z planes. This rotation is a periodic tumbling known as the Jeffery orbit [47], shown in Figure 3-6. The period of this rotation is characterised by the aspect ratio and shear rate of the flow stream [47-49].

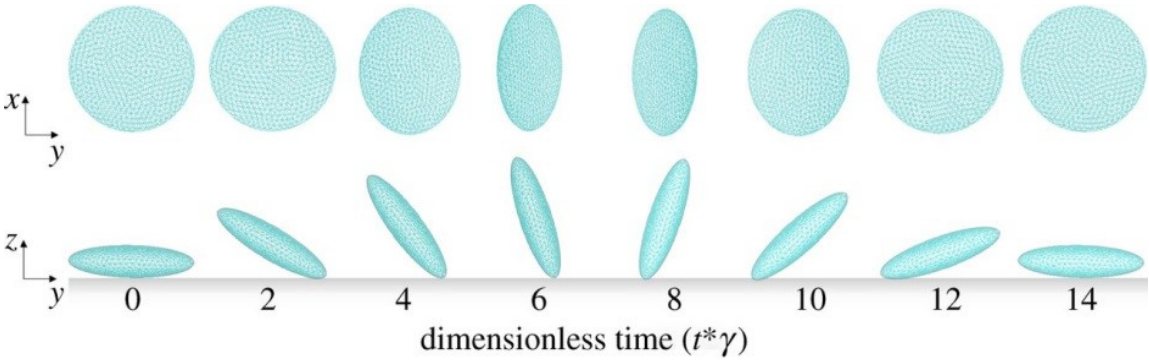

Figure 3-6, Jeffery orbit graphic [50].

$$T = {2\pi\left(r_e + {1}/{r_e}\right)}\Big/{\gamma} \tag{10}$$

Where T is the period of rotation, and r_e is the aspect ratio of the object.

For an object of known dimensions, an estimate shortest possible period of rotation (worst case) could be calculated using the shear rate at the wall of the channel (Equation 10). In the tilted channel microscope, the size and position of the object (assuming it is less than half the width of the channel) can be used to estimate the worst-case rotation.

Using Equation 6 to calculate the velocity at each end of the object. Assuming a constant velocity gradient, the difference between these two velocities over the height of the object will give the shear rate across the object (assuming constant shear).

$$\gamma = \frac{\Delta v}{\Delta h} \tag{11}$$

The period of rotation, can be multiplied by the frame rate, to estimate the number of frames taken to complete an orbit.

Deformable objects can exhibit different motions. In some cases, tank treading behaviour can be seen. This is when an object assumes an orientation where it will not rotate and moves laterally. Nematode eggs have high turgidity for the purpose of this analysis they are not considered deformable.

Objects can also migrate to the center of the channel they are flowing through. In this application the dimensions of the channel are not significantly larger than the object flowing though, so this effect was ignored.

3.3 Optics

3.3.1 Introduction

The tilted channel design makes use of the relationship between magnification and depth of focus. As magnification increases the depth of focus is reduced. To image sections of objects which are not inside the focal plane, a series of images can be collected as an object moves through the specimen plane of the imaging system, this is know as a Z-stack or focal stack. The Z-stack can be combined through image fusion to produce a compound image of the object.

The optical components of the system consist of:

- Objective lens
- Camera
- Lighting
    - Condenser
    - Filters
    - Aperture
    - Light Source
- Microchannel

The tilt on the microchannel introduces a number of optical aberrations into the imaging system. These aberrations affect the image formation and result in distorted images. Some distortions can be corrected for by software [27]. Some forms of image distortion, such

as the field curvature introduced by the objective lens, can be accepted as their effects are constant and known.

This section will outline the requirements for the imaging system, and discuss the reduction or removal of the aberrations introduced by the tilted channel.

3.3.2 Optical Prescription

Field of View

Field of View is the area visible to the imaging system. This can be expressed as the sensor width or height, over the magnification of the objective:

$$Horizontal\ FoV\ = \frac{S_h}{O_m} \tag{12}$$

$$Vertical\ FoV = \frac{S_w}{O_m} \tag{13}$$

Pixel size

The size of the pixels in the sensor along, with the resolving power of the optical components, determine the size of features which can be discriminated in an image. The pixel size also affects the level of noise in the image.

Numerical Aperture

In microscopy, numerical aperture (NA) is a dimensionless number that describes the cone of acceptance for a lens this is displayed in Figure 3-7. Numerical aperture is an indicator of the resolving power of the objective lens. Typically a higher magnification lens will have a higher NA. The NA of a lens also determines the depth of focus.

$$NA = n\ sin\emptyset \tag{14}$$

Where n is the refractive index (typically air), and $\emptyset$ is half the angle of the cone of acceptance (marginal rays).

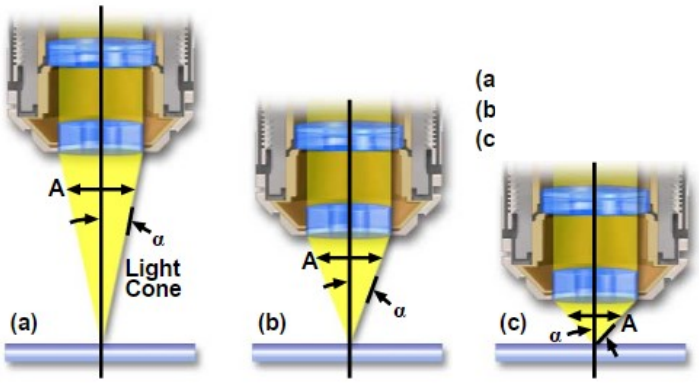

Figure 3-7, Numerical Aperture [51].

Diffraction limit

Optical systems have their resolving power limited by two mechanisms: aberration, and diffraction. Diffraction occurs because light waves through an aperture produce a diffraction pattern (Airy disk). The minimum distinguishable distance between two peaks indicates the resolving power of a diffraction limited system (shown Figure 3-8).

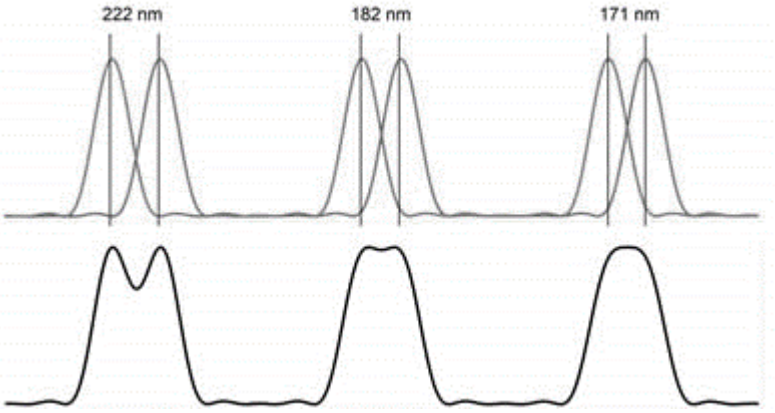

Figure 3-8, Diffraction limit (distinguishable points) [52].

The Rayleigh criterion can be used to calculate a theoretical diffraction limit for an optical system. This is derived from the NA and wavelength of illumination, λ.

$$R = \frac{0.61\lambda}{NA} \tag{15}$$

Depth of focus

Depth of focus is the distance along the optical axis (perpendicular to the image plane), which will be imaged in focus. In the tilted channel microscope, this corresponds to the

volume of fluid imaged per frame. This can be calculated from: NA, magnification, wavelength, refractive index, and resolving power.

$$D_{of} = \frac{\lambda n}{NA^2} + \frac{n}{O_m\, NA} e \tag{16}$$

Where e is the linear resolving power of the imaging system.

3.3.3 Aberrations

For optical imaging systems, aberrations occur when light rays do not focus to a point. Aberrations are caused by imperfections in the optical components. For a system to become diffraction limited, the magnitude of aberrations must be lower than the diffraction limit (resolution).

3.3.3.1 Monochromatic

Aberrations can be both chromatic, and monochromatic. Imperfections in the optical surfaces or aberration inducing components, cause image blurring to varying extents. Using higher quality optical components can mitigate this. Figure 3-9 outlines several common optical aberrations.

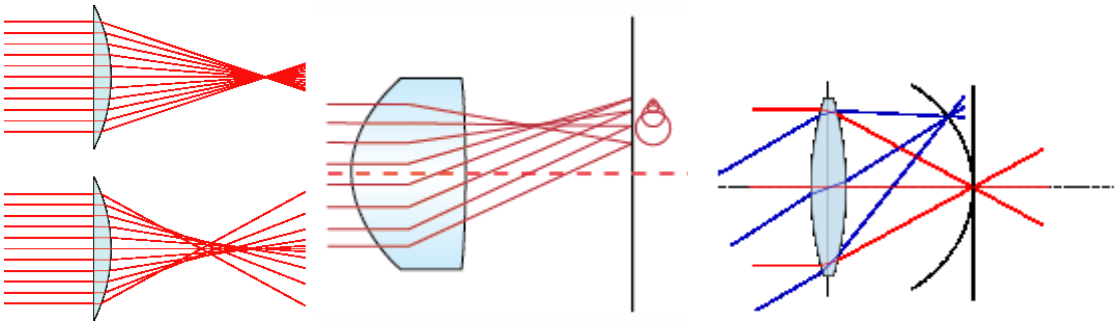

Spherical Aberration Coma Field curvature

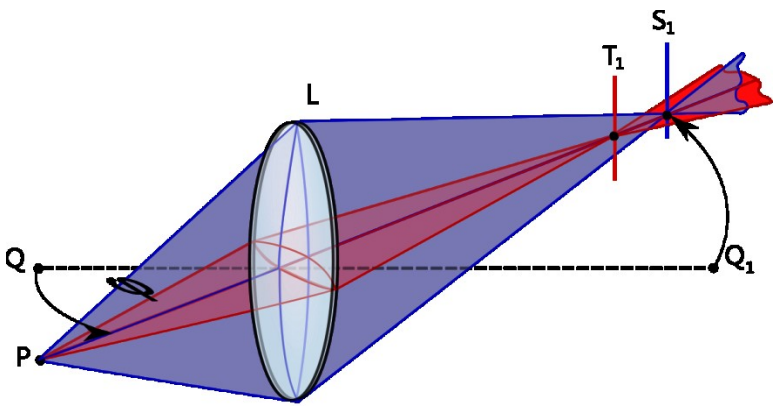

Astigmatism (Sagittal and Tangential)

Figure 3-9, Monochromatic Aberrations [53, 54].

3.3.3.2 Chromatic

Chromatic aberrations occur because different wavelengths of light are refracted to a different extent; different wavelengths will focus at different points. Using a monochromatic light source removes these aberrations. Examples of lateral and transverse chromatic aberrations are shown in Figure 3-22.

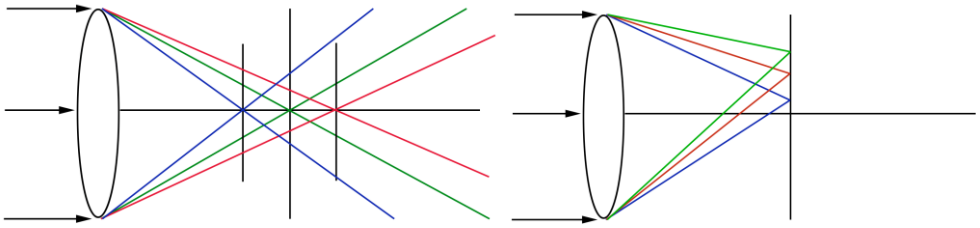

Lateral Chromatic Aberration Transverse Chromatic Aberration

Figure 3-10, Chromatic Aberrations [55].

3.3.3.3 Lens introduced aberrations

Aberrations can be introduced by all components in the optical system. Some are introduced by the objective lens, as is shown in Figure 3-11. Increasing blur is present towards the edges of the field of view, due to field curvature.

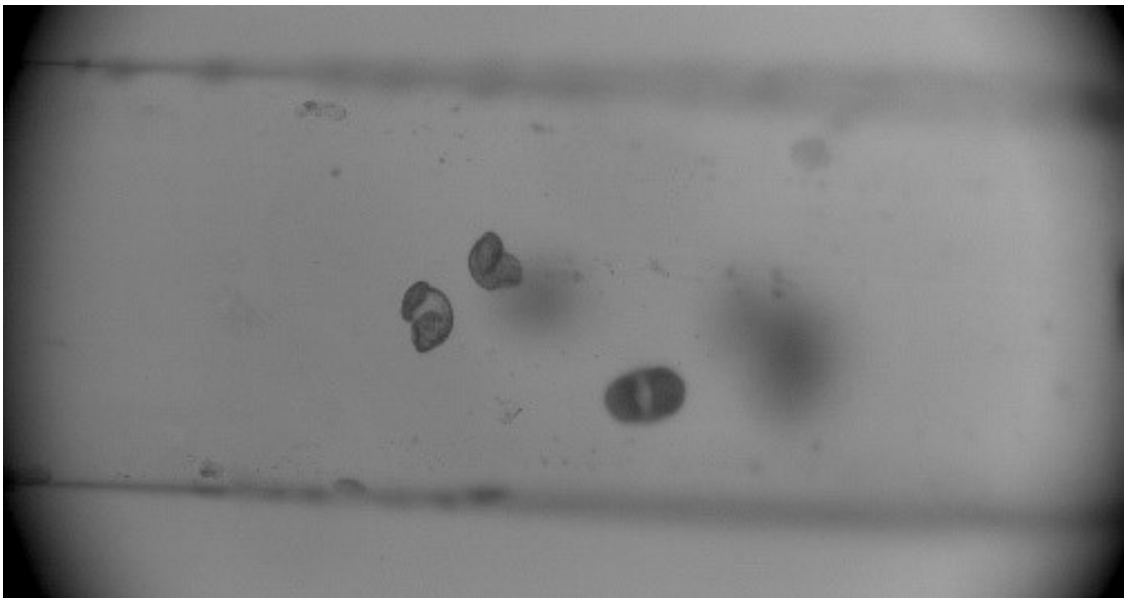

Figure 3-11, Non-uniform lens field. Field curvature causes increasing blur towards the edges of the image.

3.3.3.4 Tilted channel aberrations

The tilted microchannel introduces optical aberrations into the image forming system. This is mainly due to the material interfaces not being perpendicular to the optical axis. Light rays are refracted by this tilt causing the image to form improperly. A rectangular cross-section channel, shown in Figure 3-, acts as a plane tilted parallel plate.

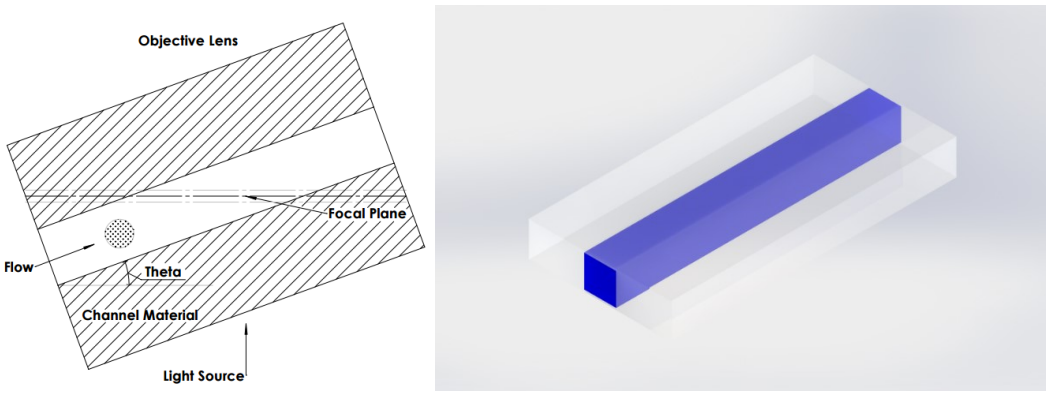

Figure 3-12, Tilted Channel design.

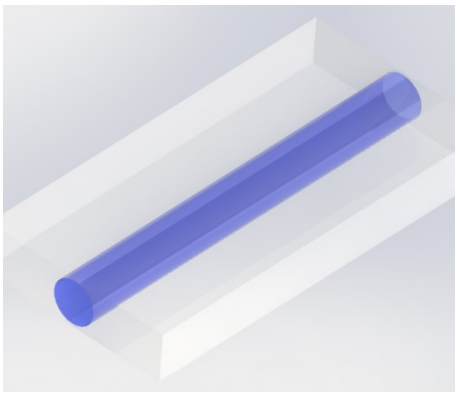

Figure 3-13, Tilted cylindrical micro channel.

A channel with a circular cross section (shown in Figure 3-13) acts as a tilted cylindrical lens. This adds additional aberrations, as the angle at each point in the image becomes a function of its position in the channel.

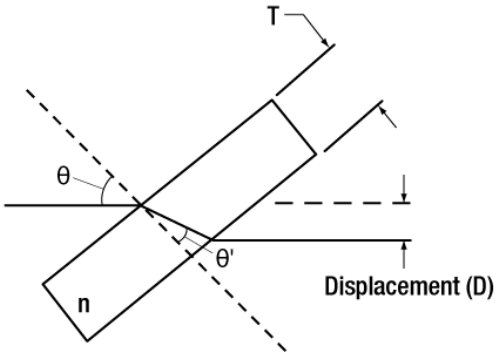

Figure 3-14, Plane tilted parallel plate for parallel wave fronts [56].

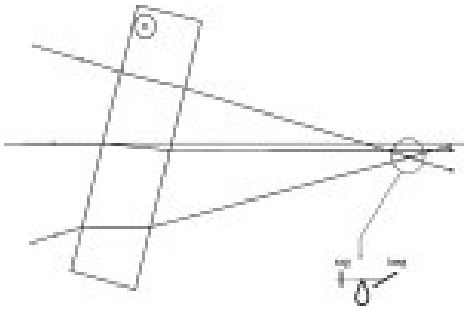

Figure 3-15, Tilted plane-parallel plate for a pencil of light [28].

When parallel light rays move through a plane tilted parallel plate, they are shifted based on the angle of the plate and difference in refractive index. All parallel rays are shifted equally by a fixed offset (Figure 3-). When a pencil of light is focused through a plane tilted parallel plate not all rays are shifted equally (Figure 3-15). Because the rays are not

parallel each ray has a different angle of incidence with the plate. The difference in shift results in defocus and aberrations in the formed image. The magnitude of the aberrations is related to the angle and difference in refractive index. In order for the tilted channel microscope to operate well, these aberrations need to be corrected for.

3.3.4 Correction Methods

Several methods for correcting the tilted plate aberrations were considered, these include:

- Adding a counter tilted plate.
- Adding an aperture stop.
- Wedge shaped blocks.
- Refractive index matching.

3.3.4.1 Counter tilted plate

A second tilted plate can be added between the channel and objective lens. To negate the refractions introduced by the previous plate, the counter tilted plate must be the same thickness, and have the opposite angle (shown in Figure 3-16).

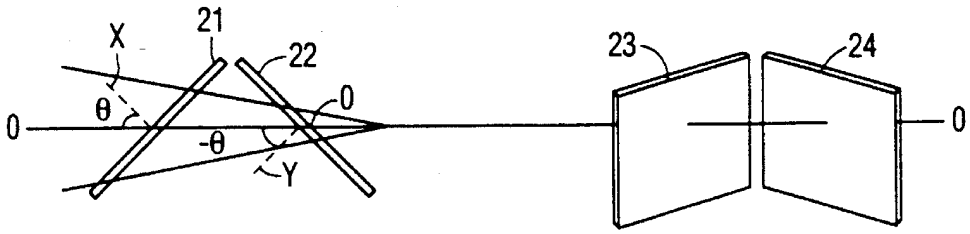

Figure 3-16, Counter tilted plate for aberration reduction [57].

The counter tilted plate has been implemented for use in digital displays to perform a similar function [57]. When applied in a tilted channel microscope, a counter tilted plate has several drawbacks:

- The addition of an extra plate between the sample and the objective requires a high working distance objective which adds to costs.
- The channel and substrate form a set of three layered plates, where the inside plate (fluid) has different properties. The same three-layer structure would need to be present in the counter plate.

The added complexity of this method makes it unattractive in this application.

3.3.4.2 Aperture stop

Reducing the aperture size of the objective lens reduces the resolving power of the microscope and extends the depth of field. If the resolving power is reduced sufficiently, the aberrations no longer determine the image quality. This effect is shown in Figure 3-17, where the objects shown without the aperture stop are more focused than those without, however the DoF is increased.

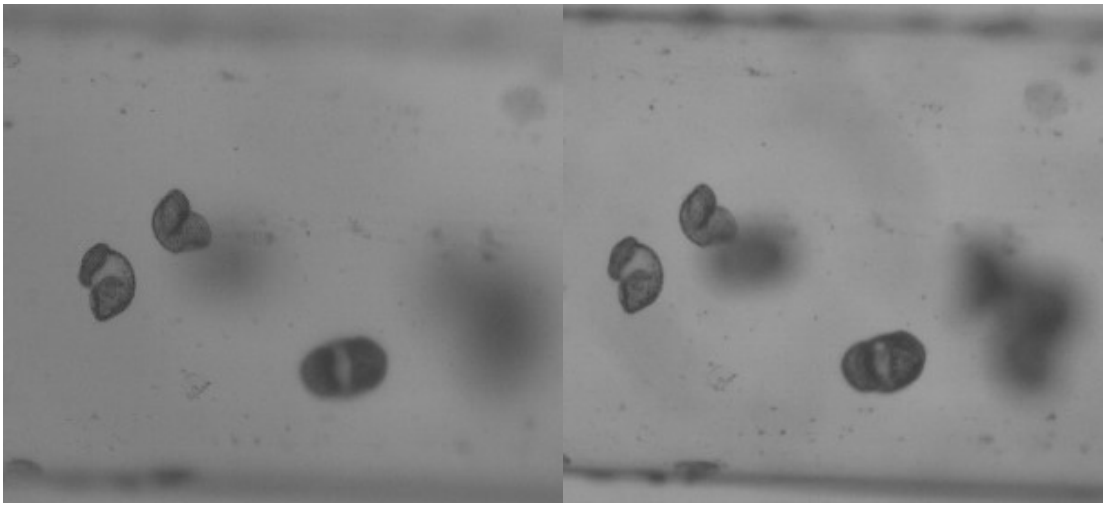

Figure 3-17, images captured at 10x magnification with and without a 1.6mm aperture stop. (left without aperture stop)

3.3.4.3 Wedge blocks

The thickness of the plane tilted parallel plate can be reduced by changing the design of the microchannel. Rather than a flat device being tilted, the channel can angle through the substrate. This design is akin to two triangular prisms separated by a plate. Drawings and renders of this are shown in Figures 3-18 and 3-19.

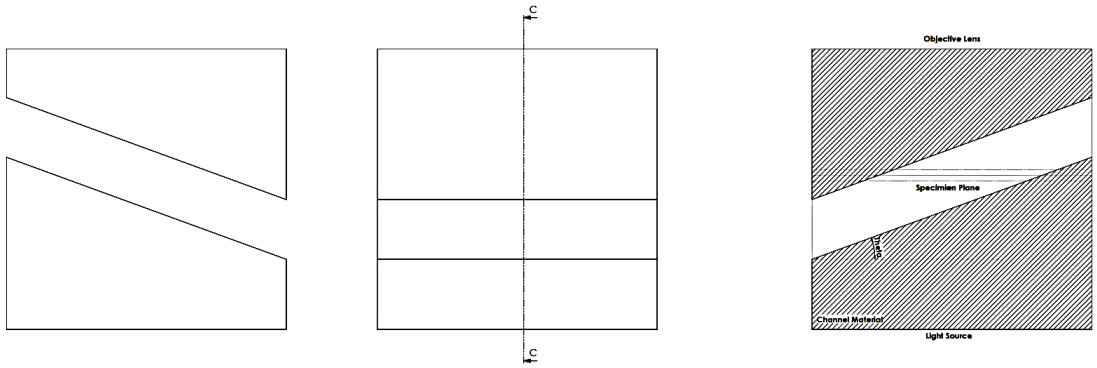

Figure 3-18, Wedge channel design drawings.

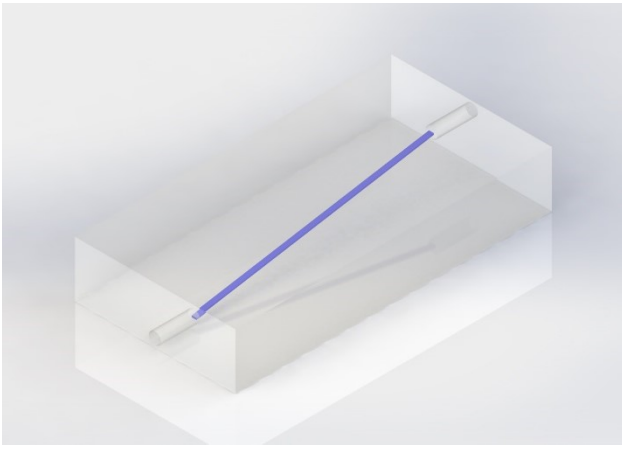

Figure 3-19, Wedge channel render.

As will be discussed in Chapter 4, a device as described above is more complicated to produce than a flat channel. The tooling required is also more difficult to produce. Cost and complexity are increased by these design changes, but image quality is improved.

3.3.4.4 Refractive Index matching

Refractive index (RI) matching can be used to reduce the magnitude of the aberrations caused by the tilted channel. The refraction at an optical interface is determined by Snells law.

$$n_1 \sin(\theta_1) = n_2 \sin(\theta_2) \tag{17}$$

Where n_1 and n_2 are the refractive indices at the interface, and θ_1 and θ_2 are the angles of incidence and refraction respectively. If both Refractive Indices are the same, then there is no refraction as the angles of incidence and reflection are the same.

In the wedge block channel design, the only angled interfaces are between the fluid in the channel and the substrate. If the fluid and substrate have matching refractive indices, the tilted interface will not cause aberrations.

RI matching has been heavily used in particle image velocimetry (PIV), where it is required to image through complex transparent geometry [58].

The materials and fluids which can be paired by refractive index are limited. Low cost microchannels of moderate geometry must be able to be produced from the material. While the fluid must be water soluble, and not contain a high salt concentration. The fluid must also be non-toxic, optically transparent at the illumination wavelength, and low cost.

Because of these constraints, PDMS was chosen as the substrate material, and a glycerol water solution as the carrier fluid. PDMS typically has a RI of 1.41, and a glycerol solution at 60% by weight matches this.

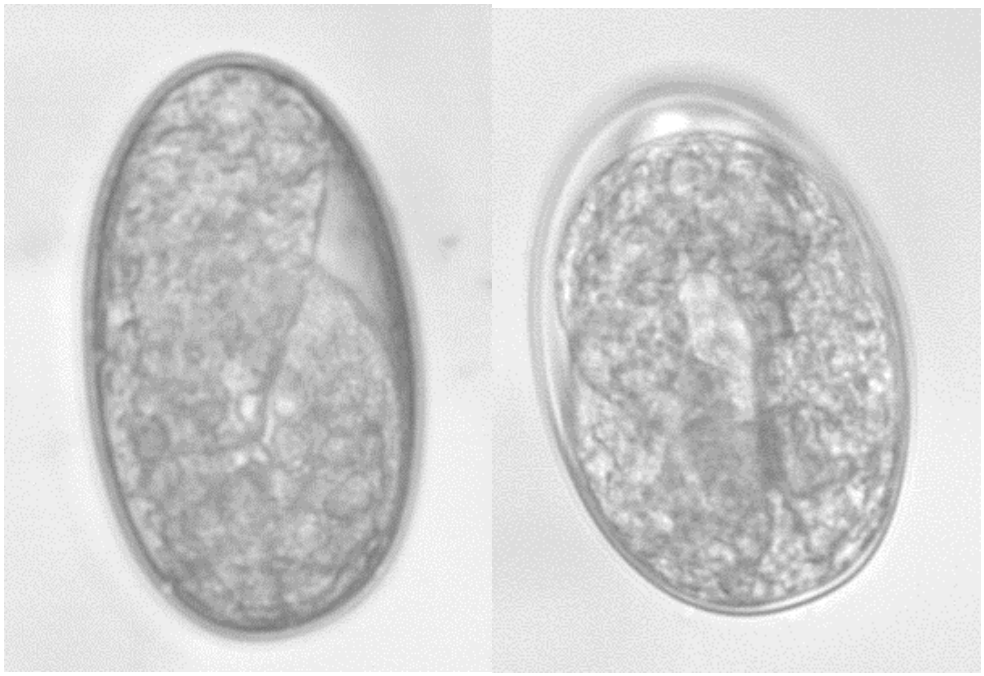

Figure 3-20, Microchannel and slide egg images, Images are not of the same object. (Microchannel Left, Slide Right).

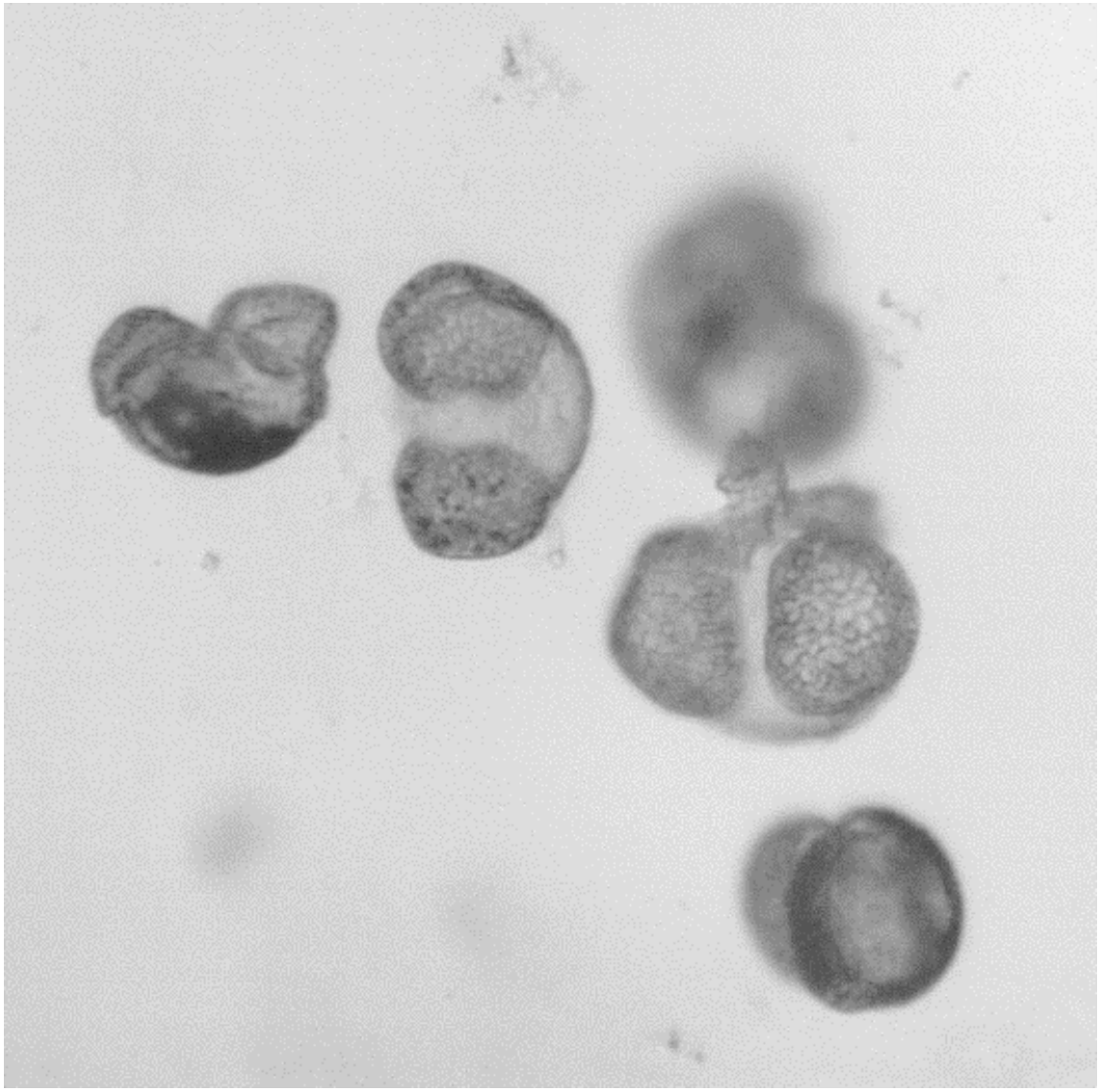

Figure 3-21, Pollen in RI matched wedge block channel.

Figure 3-, and Figure 3-20 show the level of image quality achievable when a wedge block design (hybrid PMMA/PDMS see Chapter 4) and refractive index matching are combined.

3.3.5 Ray Tracing

Zemax optical modelling software was used to produce ray traces of the tilted parallel plate. A model of a plane tilted parallel plate, using the same RI as PDMS was produced. A point spread function and spot diagrams were generated.

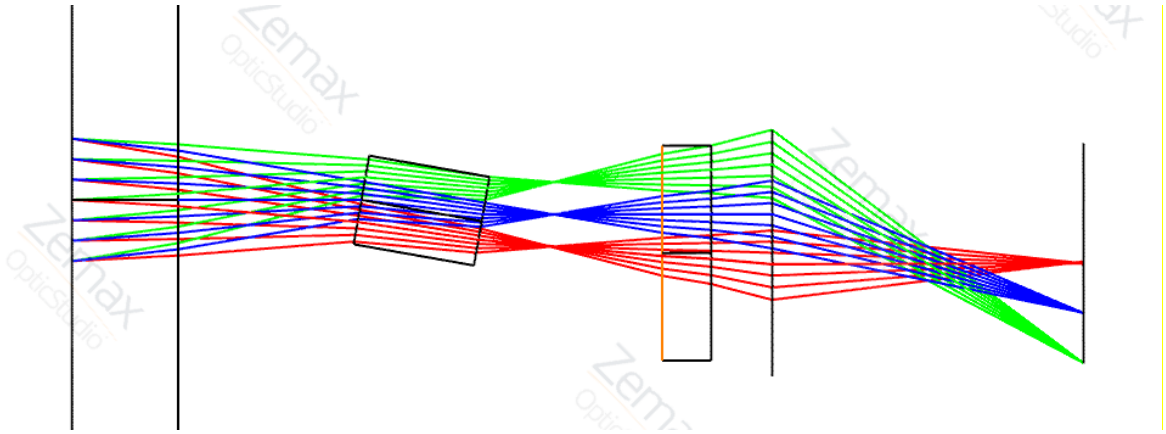

Figure 3-22, Zemax ray trace with tilted plate.

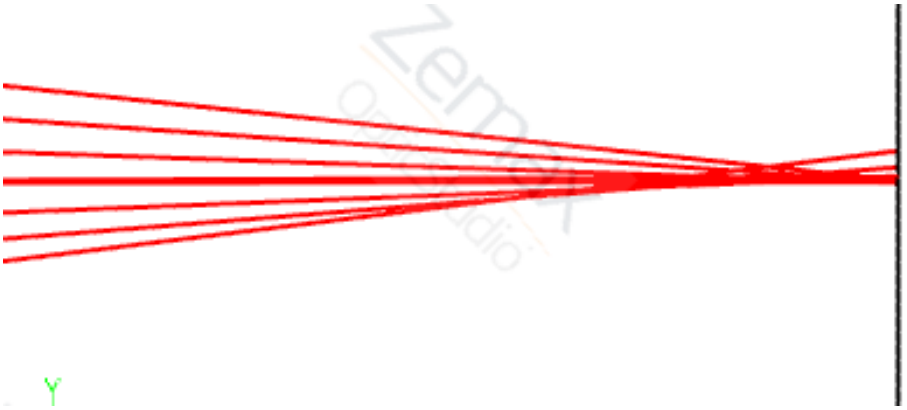

Figure 3-8, Defocus in ray trace (red rays from Figure 3-22).

3.3.6 Optical Limitations of Tilt Angle

The tilted channel aberrations are a function of the channel angle. Minimising the angle is important in ensuring that the optics are diffraction limited. The angle required is a function of channel height and the field of view of the sensor. The wider the sensor is, the longer the hypotenuse and the shallower the angle.

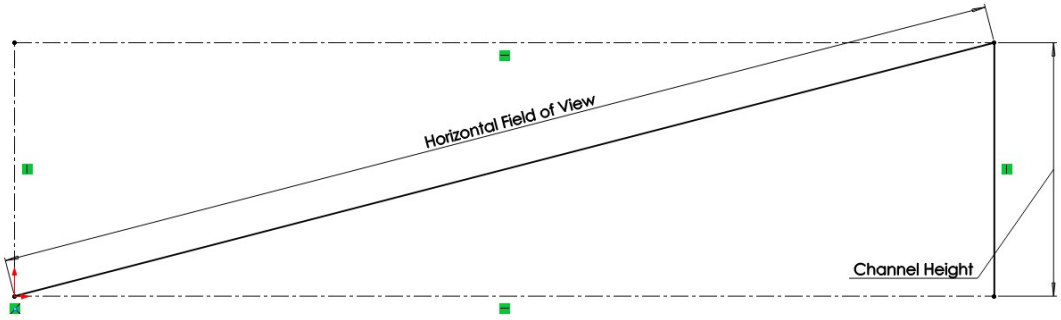

Figure 3-24, Simple channel geometry.

3.4 Lighting

Considerations of the following aspects were required when designing the lighting for the tilted channel microscope:

- Motion blur
- Chromatic aberrations
- Object fluorescence

Motion blur has a negative effect on image quality (as seen in Figure 3-25). To minimize this, the image must be exposed in a sufficiently short period; the exposure time should be shorter than the time taken for an object to move one pixel.

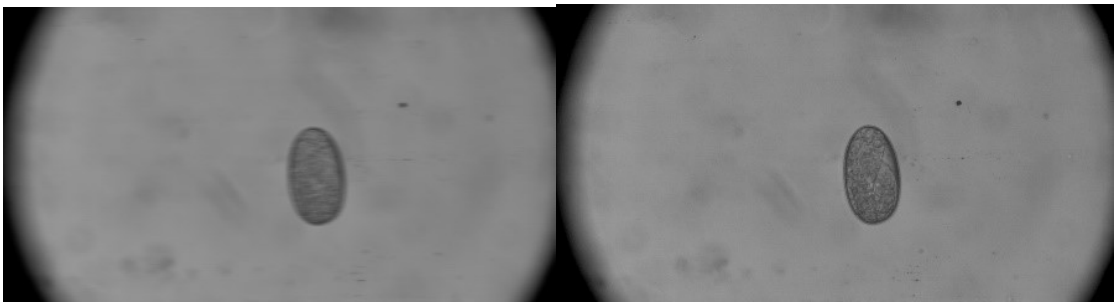

Figure 3-25, Egg image with and without motion blur.

Chromatic aberrations can be removed by using either a laser or monochromatic LED for illumination. The illumination wavelength should not cause the objects to fluoresce.

Both light field and dark field lighting were tested for this machine. While dark field provides good contrast and potentially more information, lower exposure times were achievable with bright field, resulting in less motion blur.

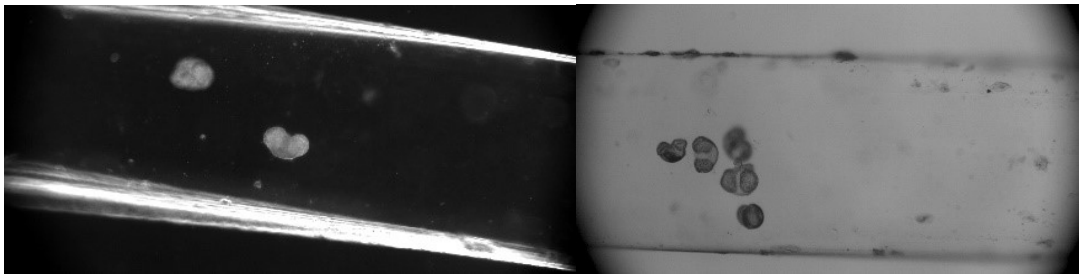

Figure 3-26, Bright and dark field pine pollen comparison.

3.5 Discussion

3.5.1 Fluid Mechanics Discussion

The rotation of objects as they move through the channel may offer some benefits. Surface features, which may have been occluded by object orientation, are revealed as the object rotates. This creates an opportunity to gather additional information on the object. Experimental work could be conducted to assess if this offers significant improvement in object detection and discrimination.

As the period of the rotation is connected to the shear rate, the object will rotate fastest when close to the wall. Only a small proportion of objects will travel here as fluid velocity at the wall is zero. Similarly, objects moving through the center of the channel can experience balanced shear across them and may not rotate at all. The majority of the objects in the channel will be decentred in some way, thus experience some rotation.

3.5.2 Optics Discussion

Magnification and the volume of fluid in focus have a strongly inverse relationship. For the specimen plane to cut through the entire channel as magnification increases, either the channel dimensions must decrease or the tilt angle must increase. As the tilt angle increases, the magnitude of the associated aberrations also increases. Although correction methods exist, it is likely to be impractical to correct for the aberrations as the angle becomes increasingly large. This all means that there is a theoretical upper limit on the level of magnification relative to the size of the objects of interest and to the efficacy of the correction method. Additional work could be completed to quantify this limit.

Chapter 4. Microchannel Fabrication

Microchannels are devices used in the study of microfluidics. They are designed to contain and manipulate fluids at small scales. Microchannels have applications in a variety of fields, from inkjet printers to complex lab-on-a-chip systems.

Typically microchannels are used to manipulate fluids in the nanoliter to microliter range, hence their dimensions can vary from tens of nanometers to hundreds of microns (10 nm – 500 um). Fluid manipulation at this size range has some advantages over larger scale experiments. Low fluid volumes and flow rates are associated with very laminar flow regimes, giving predictable mixing and behaviour. Small scale experiments also require less energy and materials than those at full scale.

Low scale experiments can be demanding to image, often requiring a high magnification microscope. When a microscope is involved, the optical properties, surface roughness, refractive index, and Abbe number, of the microchannel affect image quality.

Creating a microchannel suitable for this application was an iterative process, as the performance of each design helped further refined the requirements of the application. Designs which were initially considered favourable, were found to be impractical or overly complicated to produce.

A variety of materials and methods are available for fabricating microchannels. The materials and methods considered in this chapter are a subset of those which were available to the author and were selected based upon the financial and time constraints of the project. These materials are;

- Glass
- Poly(methyl methacrylate) (PMMA)
- Polydimethylsiloxane (PDMS)
- Cyclic olefin copolymer (COC)

This chapter will detail the requirements of a microchannel in this application, the available materials, and the fabrication methods which were trialled .

4.1 Flow Cell Requirements

For design testing and development, a microchannel needed to be produced which would meet the requirements of the system. These requirements were represented as the following set of criteria:

- Cost
    - Cost per unit
    - Capital cost of equipment
- Performance
    - Refractive index
    - Surface finish
    - Reliability
    - Re-useability
    - Interface
- Channel geometry
    - Channel angle (10-20 degrees)
    - Channel dimensions (100x100 to 200x500 um)
    - Channel profile (rectangular preferable)
    - Material thickness (top plate less than 2mm for objective working distance)
        - Top plate thickness
        - Bottom plate thickness

To select a channel design, material, and fabrication method, the following process was followed. An assessment was made if a particular material and methodology could be used to produce channels of the required size range, and geometry (depth, width, angle). This is followed by a simple cost analysis of the required equipment, cost per device, and device life span. Finally the fluids with possible refractive index matches to the channel are considered. If the refractive index matching fluids are unsuitable (dangerous to the user, or damaging to nematode eggs), the material is considered unsuitable. Simple and inherently low cost materials were trialled iteratively to both improve the channel design and find the most suitable fabrication method.

4.2 Materials

4.2.1 Glass

One of the materials considered was glass. Microchannels can be produced from glass through a process called chemical milling. Chemical milling is an etching process where a channel is formed by removing a controlled amount of material. Resistant masks are used to determine which sections of material are removed. After the etching process, a thin top plate is bonded over the channel to enclose it.

Some glass devices made by the University of South Australia (UoSA) and Dr Rob Ward, were trialled in the early stages of this project. These devices had a cross section of 500x50µm and a top thickness of 0.17mm (the same as a cover slip).

The chemical milling process cannot be used to produce angled microchannels as described in the previous two chapters. Chemically milled devices have limited dimensions due to the nature of how they are made. At an estimated cost of $300 per device, glass microchannels were too expensive to use as potentially disposable items in this application, however they were invaluable to the initial development stages of this project.

4.2.2 Cyclic olefin copolymer (CoC)

Cyclic olefin copolymer is a material which can be used to make microchannels of complex geometries through additive manufacturing (3D printing). The flexibility inherent in 3D printing channels was appealing and prompted further investigation. However it was found that the cost per device was high, due to the long manufacture times, and expensive equipment required.

It was concluded that, although microchannels of the required geometry could be produced by CoC, the costs were too high, and availability was too low to warrant further investigation.

4.2.3 PMMA

PMMA or Acrylic is commonly used to produce microchannels. PMMA has a refractive index of 1.49, and can be matched to high concentration salt solutions (sodium iodide, zinc iodide). Paracymene is also a refractive index match, however prolonged exposure results in damage to the PMMA.

PMMA channels can be produced in many ways. Due to their availability the following were considered in this project:

- Conventional milling.
- Laser etching.
- High speed milling.

Once a channel has been formed in a substrate, a top plate must be attached to seal the channel. The thickness of this top plate is important in this application, due to the limited working distance of high magnification objective lenses. The following bonding methods were assessed:

- Adhesive bonding (tape, and liquid)
- Solvent bonding
- Thermal bonding.

Some PMMA channels were produced by the UOSA using their high speed and precision milling equipment. The results of each of these methods, and how they lead to subsequent development will be discussed in the following sections.

4.2.3.1 CO2 Laser

CO2 laser cutters can be used to cut groves into PMMA plates. Once a top plate is bonded over these groves they act as microchannels [59]. CO2 laser cutters are commonly found in engineering workshops. To make use of this, a simple two plate design was trialled. This design featured a bottom plate with the microchannel etched into it by the laser, and a top plate with inlet and outlet ports drilled into it shown in Figure 4-1.

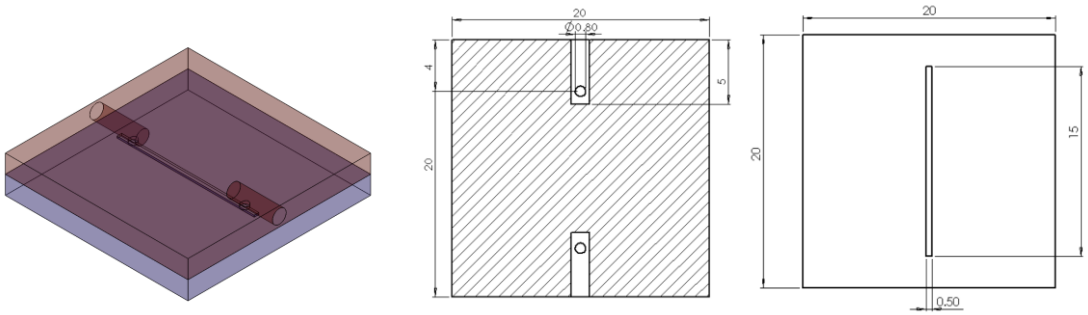

Figure 4-1, Channel plates design (top plate in red (shown in center), bottom plate in blue (shown on right)) units in mm.

Before a channel could be fabricated, it was necessary to assess how the laser cutter (an Epilog M2) would perform when attempting to cut small precise groves into PMMA plates. A simple experiment was performed, where a number of channels were cut at a variety of settings. The following parameters were varied to find the best options:

- Laser power
- Cutting speed
- Dots per inch (DPI)
- Direction

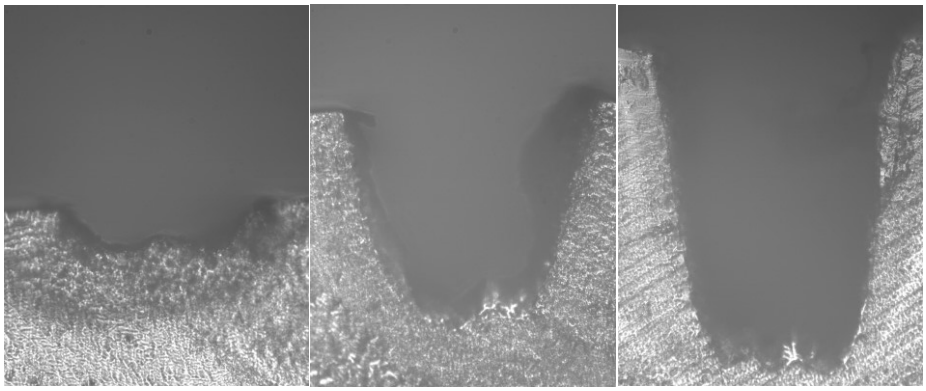

Figure 4-2, CO2 Laser channel profiles at 1200DPI, (left: 50% speed 2% laser power, Center: 50% speed 10% laser power, Right: 10% speed 6% laser power) (all cuts were horizontal).

Figure 4-2 demonstrates how the channel cross-section changes as laser power and speed vary. The laser cutter focuses the laser at a single point below the surface so the profile of the section is not square, resulting in unsatisfactory channel geometry. It should also be noted that the bottom section of the channel is not flat when cut in this manner. This irregularity could introduce aberrations to the optical system and as such is undesirable.

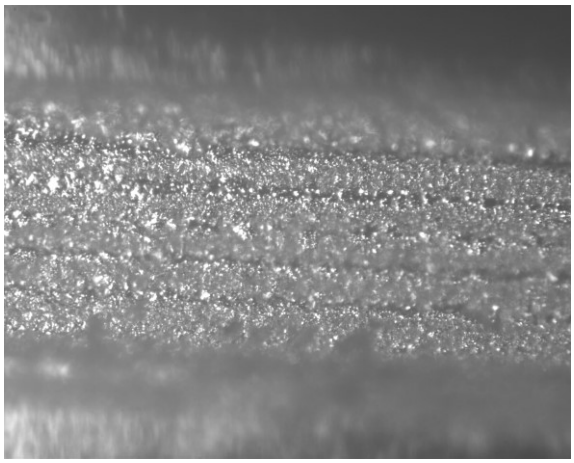

Figure 4-3, Surface finish of Horizontal cut at 50% speed 2% laser power, 1200DPI.

Figure 4-3, shows the bottom surface of a grove resulting from horizontal low power cuts. As to be expected from the previous images, the surface finish is rough. This roughness could be due to PMMA particles being deposited on the surface during the etching, or simply due to the laser not being focused at the bottom of the channel, and heating the surface inconsistently.

Decreasing speed while increasing power, results in smoother, squarer channels, however the channel depth is also increased. It should be noted that in the above Figure 4-2, the channel wall on the top is substantially smoother than the bottom. The channel floor (shown in of figure 4-3), shows several distinct notches. This may be due to the width of the laser beam and the several passes used to form the grove.

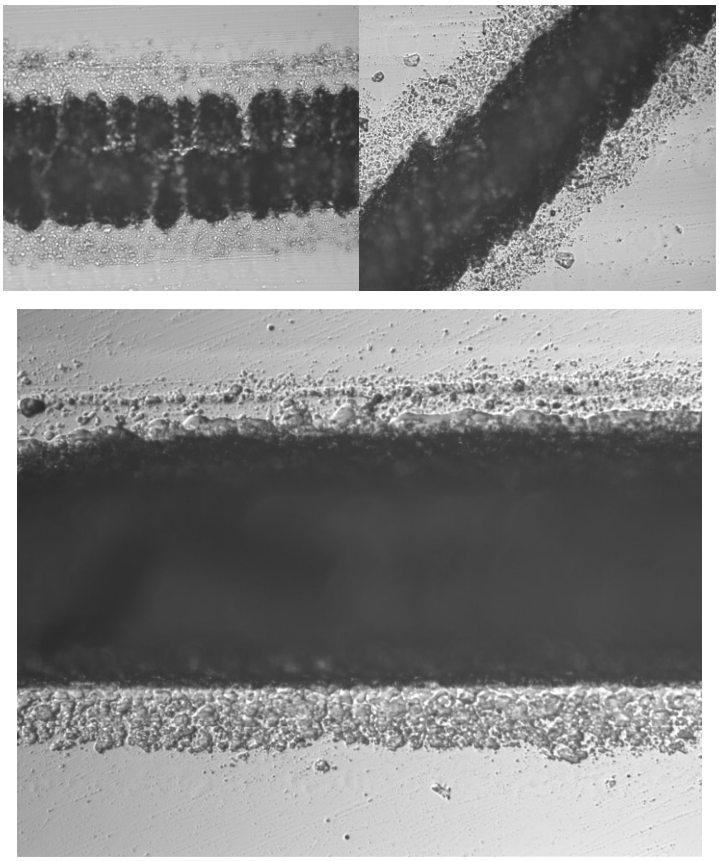

Figure 4-4, Top down channel profiles (Top left: vertical cuts on horizontal path, Top right: vertical cuts on diagonal path, Bottom: horizontal cuts on horizontal line)

Altering the direction of the laser scan relative to the cut resulted in much poorer channel cuts. Rather than taking long cuts along the major axis of the cut, the laser instead takes a number of short cuts which have the same length as the desired channel width. When cuts are taken at 45 degrees to the major axis of the channel, the results were improved although still inferior to a horizontal cut (this can be seen in Figure 4-4).

The above results, along with the difficulties in bonding PMMA surfaces, lead to the conclusion that this fabrication method would need significant improvements to produce useful channels with controllable dimensions. Several papers have demonstrated the use of low power lasers to produce channels. Further exploration of repeated passes at varying depth may be worth consideration, however time constraints dictated that laser cut channels were not explored further in this project.

4.2.3.2 Conventionally Milled channels

Several channels were produced through conventional machining, using a 0.127mm cutter (shown in Figure 4-5). These devices had a very rough surface finish due to the

lack of precision available with this tooling. The desired channel width was only several times the width of the cutter.

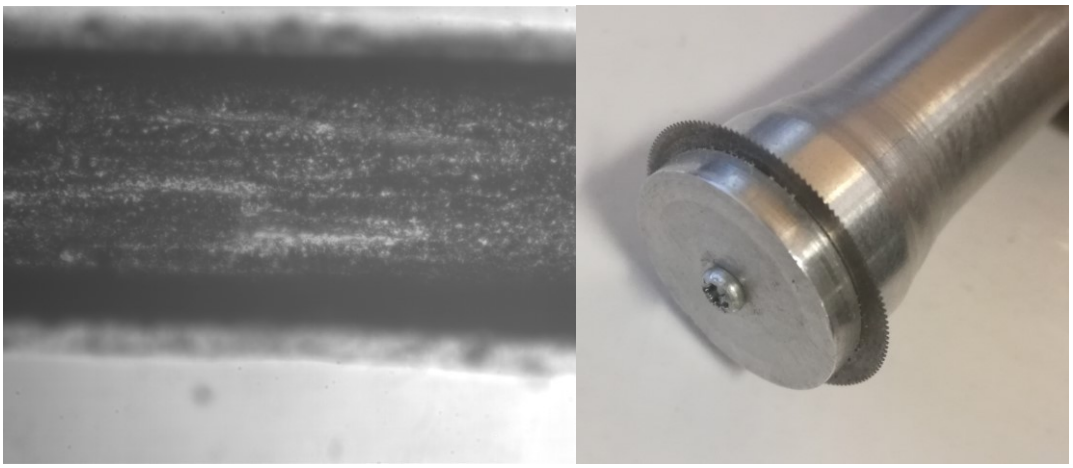

Figure 4-5, Machined surface finish and tooling.

4.2.3.3 Bonding PMMA

Several methods for bonding PMMA channels with thin top plates were trialled, however they proved unreliable and difficult to control. The methods examined were: adhesive bonding, solvent bonding (acetone, chloroform), and thermal bonding.

4.2.3.3.1 Adhesive bonding

Adhesive methods for bonding the two surfaces together made use of a transparent adhesive produced by Loctite (Loctite 406). Once applied between the two surfaces, the adhesive set holding them together. Several problems were experienced with this method, importantly, it was difficult to control the amount of adhesive applied. Too much adhesive resulted in leakage into the channel. An attempt was made to compensate for this by placing wells next to the channels where excess adhesive could pool (shown in Figure 4-6 and Figure 4-7). However, this did not eliminate the problem, excess adhesive would still enter the channel and potentially block it. On the other hand, too little adhesive resulted in a channel which was not entirely sealed, and could neither withstand pressurisation nor retain fluid.

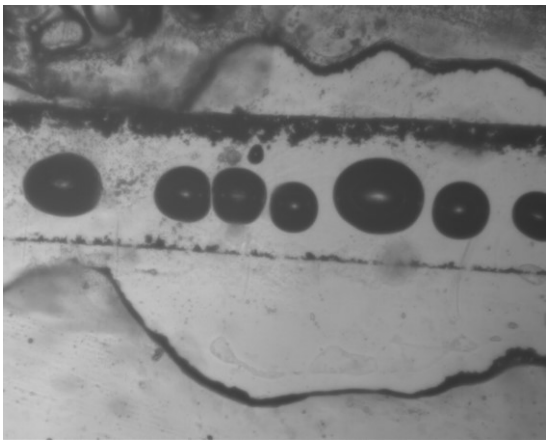

Figure 4-6, Adhesive well full after gluing.

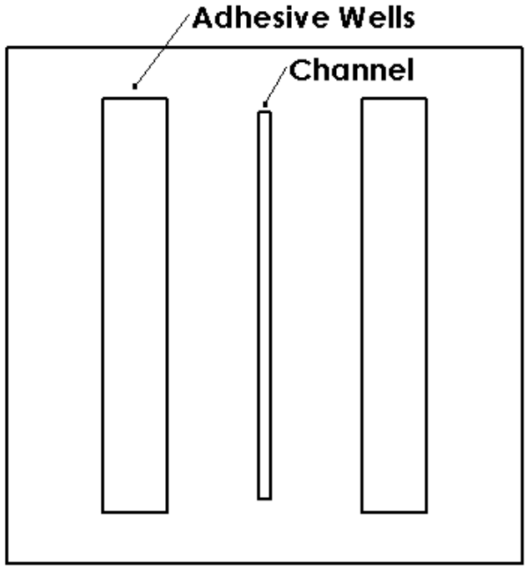

Figure 4-7, Adhesive wells, to prevent superfluous adhesive from entering channel.

Due to the limitations of the adhesive bonding approach, it was decided to investigate alternative methods of fusing the two surfaces together.

4.2.3.3.2 Solvent bonding

Two solvents, chloroform and acetone, were tested for bonding PMMA plates together. Under a fume hood, two PMMA surfaces were treated with the solvents and then held together to seal them. This method resulted in two plates which were loosely attached. Significant external force, or internal pressure could separate them. However, the seal was strong enough to introduce fluids to the channel. Upon inspection, the channels leaked where the surfaces were not bonded properly, and cracks had formed in and around the channel area. The cracks can be seen in Figure 4-8.

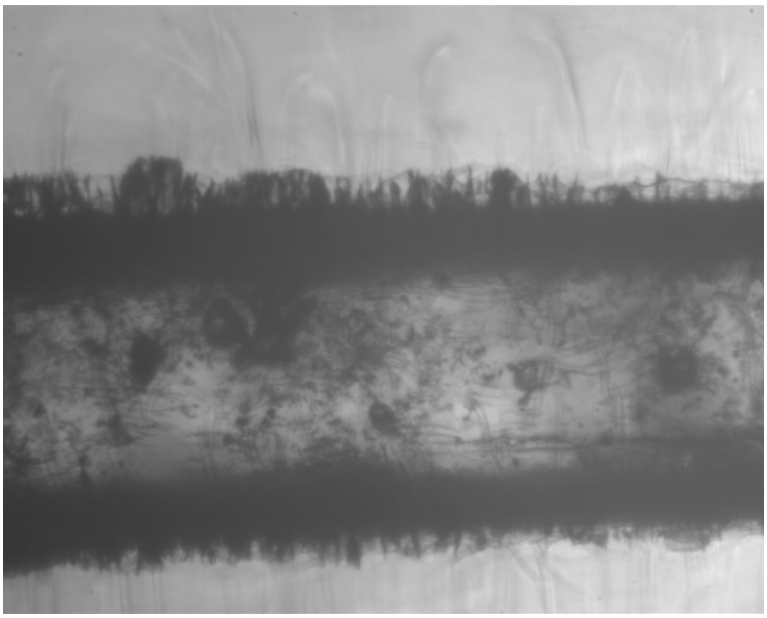

Figure 4-8, Cracks in and around channel from solvent bonding technique.

4.2.3.3.3 Thermal bonding

The glass transition temperature of PMMA is 105˚C. The author expected that two pieces of PMMA which were clamped together, and then elevated to this temperature would produce a sealed unit. Several attempts were made at this, the first failed as due to reduced clamping force when the plates became malleable. The second attempt, which successfuly bonded the two pieces, used a weight to provide a constant clamping force. Although bonded, these channels did not seal well. In a final attempt the pieces were placed in a vacuum oven at the glass transition temperature for 24 hours. The resulting pieces formed a sealed channel (shown in Figure 4-9), however this had poor performance and could not handle internal pressure, coming apart in its first use.

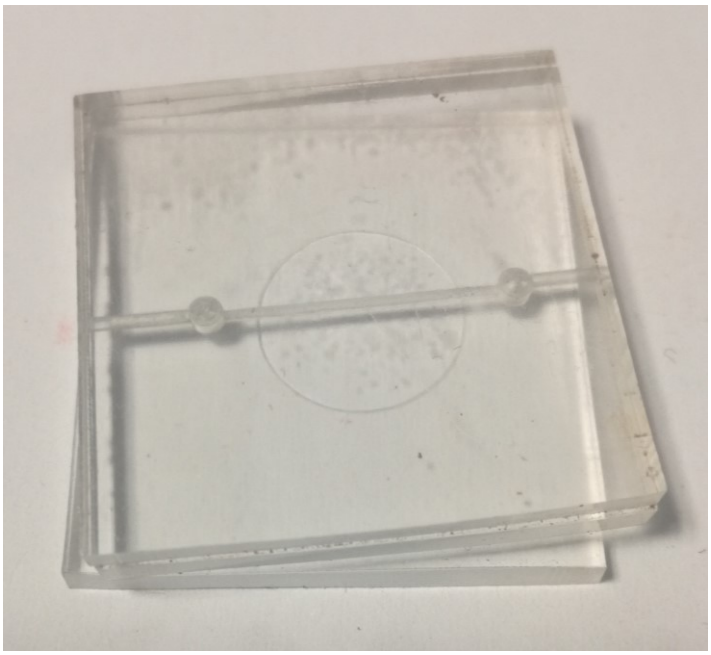

Figure 4-9, Thermally bonded channel from two pieces of PMMA.

4.2.3.4 UoSA Milling and adhesive tape

Although the above fabrication methods showed some promise, they were unlikely to produce channels which met the requirements of the project. Due to time constraints it was decided to forgo developing an in-house PMMA device, and to instead outsource the development to an outfit with more experience and superior equipment. To this end several devices were commissioned from the University of South Australia. They have the facilities for producing microchannels from both glass and PMMA.

Through consultation with the UoSA, the design shown in Figure 4-10 was selected. this design featured top and bottom plates of 3mm thickness, and a rectangular cross-section channel of 500x200µm. The 3mm top and bottom plate thickness was due to limitations in the fabrication technique, and was needed for the channel fittings.

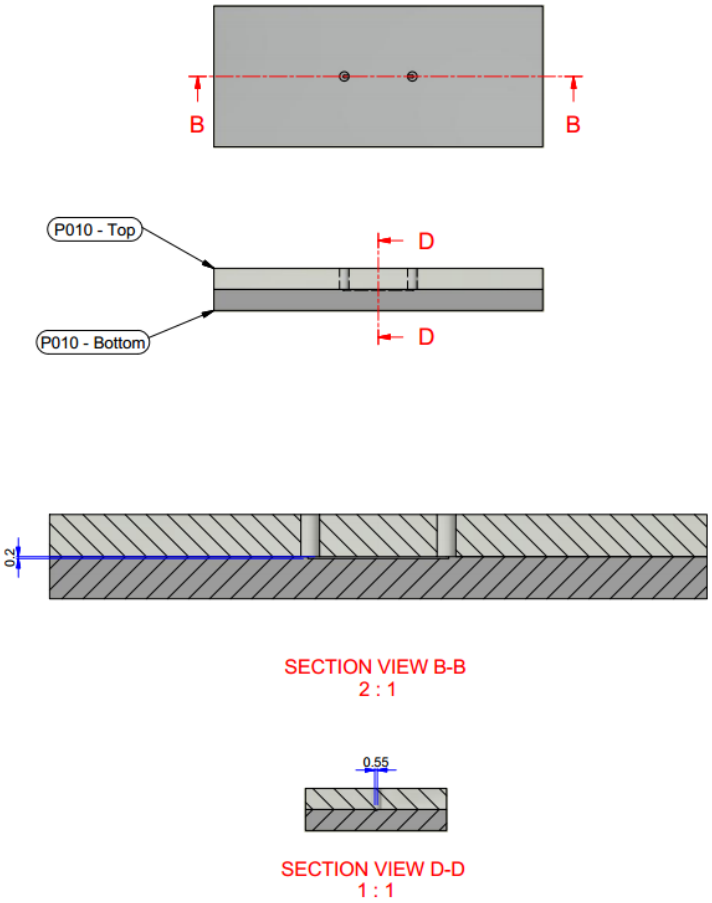

Figure 4-10, Design commissioned from UoSA (CAD drawings produced by Mark Cherill)

These devices use a twist-in fitting for rubber tubing called Radulok. The fitting is a simple shape milled onto the inside of the top plate of the fluidics device. This fitting is designed such that when pressurised the tubing pushes out against it, holding itself in place. The fitting is rated up to 200bar, a pin chuck is required to screw the tubing into the fitting (shown in Figure 4-11).

Figure 4-11, Radulok fitting in PMMA microchannel.

The surface finish of these channels was far superior to that produced using the laser cutter. The tools at the UoSA allowed for measurement of the channel profile. This is shown in Figure 4-12. Measurement showed that the largest irregularity in the channel surface was several microns in extent.

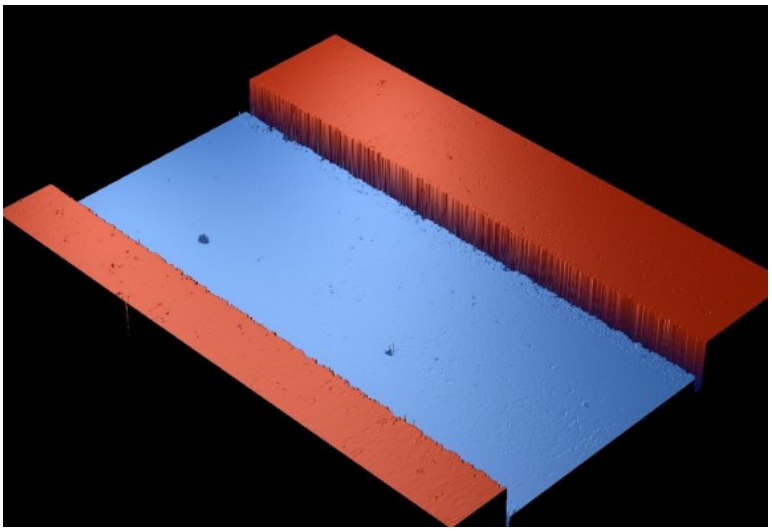

Figure 4-12, UoSA channel profile (Figure provided by Mark Cheril).

These channels were constructed using high-speed machining. Small cutters at low feed rates slowly machine away material to create a smooth channel profile. Thin and deep channels cannot be machined, due to the limited width to depth ratio of the tooling. After machining and testing, the channel is then bonded to a top plate with a thin adhesive tape.

These channels were a significant improvement on the in-house attempts to produce PMMA channels, however still had some impracticalities:

- Objects tended to clump around the edges of the channel (shown in Figure 4-13). This could be due to the thin adhesive tape layer or the very rectangular channel profile.
- The channels also could not be tilted through the substrate without significant alterations to the manufacturing process.
- At a cost of several hundred dollars per device, the PMMA devices did not offer significant advantages over glass channels.

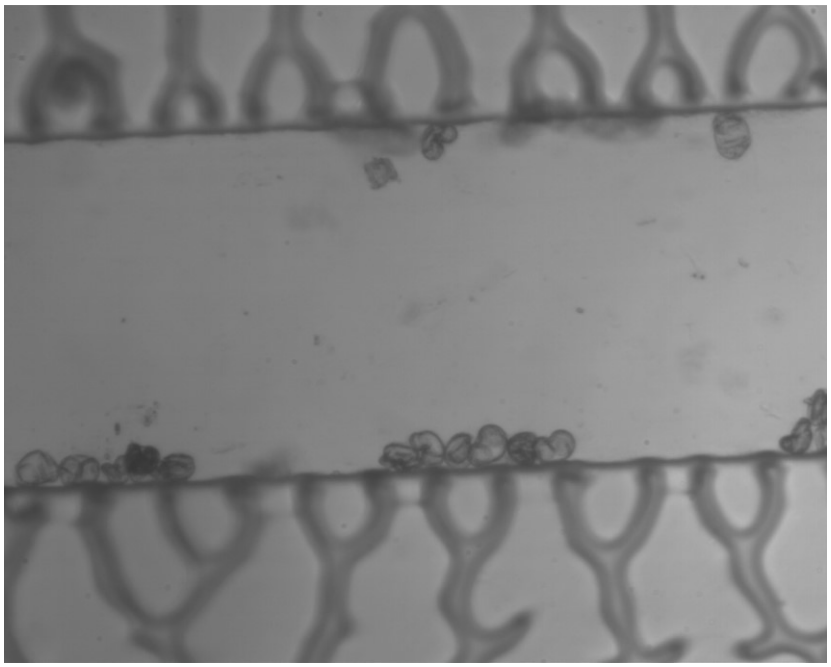

Figure 4-13, Pine pollen clumping at channel walls. (4X objective magnification)

The UoSA did present an alternative design (shown in Figure 4-14), which would allow for a tilted channel. However, due to the time constrains, and the success of PDMS devices, this was not further explored.

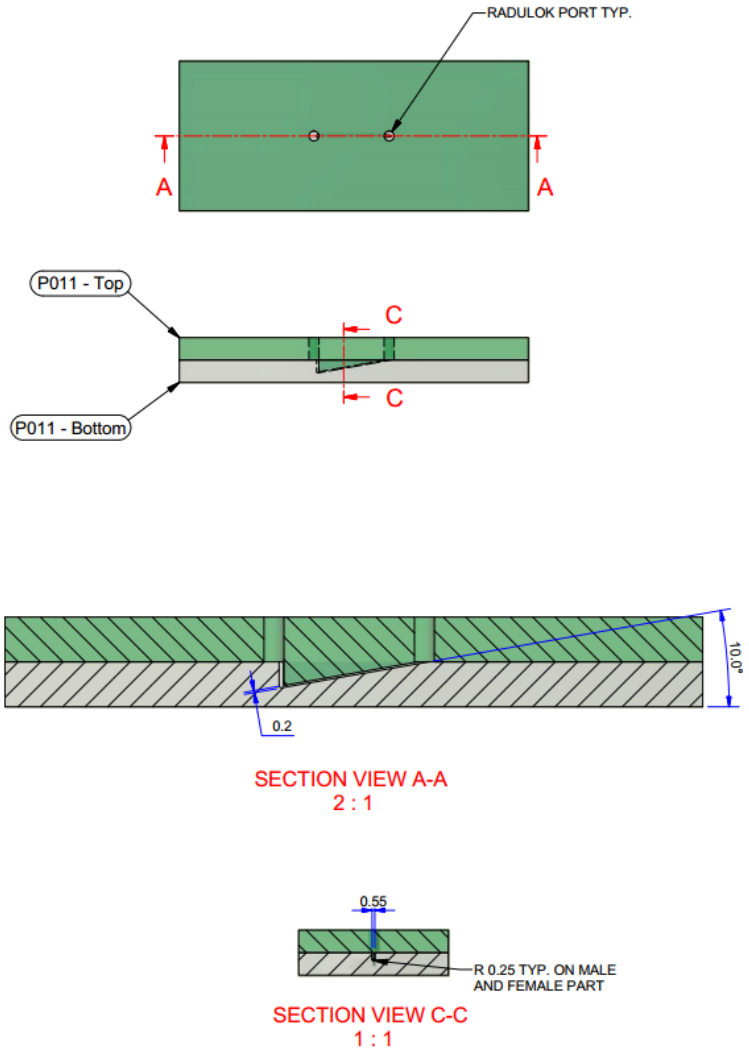

Figure 4-14, Tilted channel CAD design (CAD drawings produced by Mark Cherill).

4.2.4 PDMS

PDMS is a silicone organic polymer. It has uses ranging from contact lenses to lubricants, and is one of the most widely used organic polymers. PDMS is non-toxic and inflammable. PDMS has been used extensively for microchannel fabrication [60], because it is simple to fabricate channels. Depending on how it is treated, PDMS can exhibit hydrophobic or hydrophilic surface properties. The refractive index of PDMS is 1.4, This allows for matches with fluids more suitable to this application than PMMA; RI matching fluids like aqueous solutions of glycerol are less damaging to nematode eggs than saturated salt solution, and easier to handle.

PDMS can be purchased as a two-pot mix. When combined, the two fluids will set into a flexible solid. During the curing process the PDMS can be molded to form a

microchannel. Removeable cores can be inserted into the curing PDMS. After curing the core is removed, leaving behind a channel [61]. Curing times and solid properties are temperature dependant. In the case of this project, Sylgard 184 (see appendix I) was the selected PDMS. For channel production it was cured for a period of one hour at a temperature of 100˚C.

Requiring little in the way of specialised equipment or skills, PDMS is a simple material for fabricating microchannels. It can be at as little as $1 per gram, and has a suitably low refractive index for this application.

Several iterations of PDMS channels were constructed as the specifications and process were refined. The first two versions were produced with the aid of Callaghan Innovation, who provided the soft lithography, molding equipment, and PDMS.

4.2.4.1 Callaghan Innovation channels

Callaghan Innovation is a government funded research provider. Their role is to assist New Zealand businesses in research and development. The PDMS microchannel design and fabrication was completed with substantial assistance from their microfabrication team.

4.2.4.1.1 First iteration

Callaghan Innovation produced a number of devices which were instrumental in the development of a functional system. These devices were constructed using PDMS with a technique known as Soft Lithography [62].

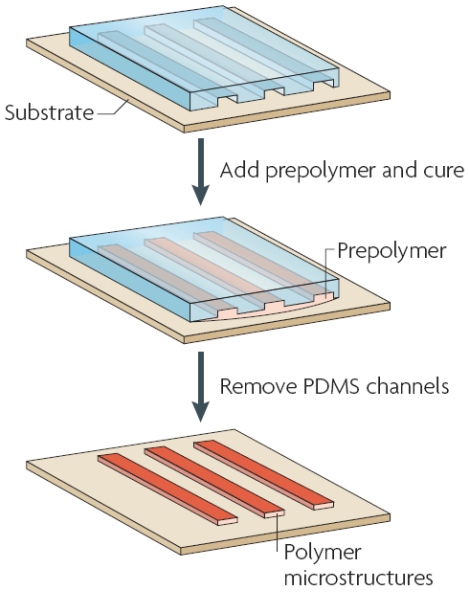

Figure 4-15, PDMS soft lithography [62].

This technique uses stamped channel profiles to form the channel. PDMS is mixed and then allowed to cure over the stamps to emboss the channel geometry in the finished device. The stamps are created by using a laser and photoresist to build up the channel material on a substrate. PDMS is poured over the stamps, degassed, and allowed to cure. After removal from the substrate, the microchannel is imprinted into the PDMS. This imprinted face can then be covered to enclose the channel. For the first devices a thin Mylar sheet was placed over the channel to seal it. This Mylar layer was of a similar thickness to a microscope cover slip, allowing for low working distance objective lenses to be used. These first devices can be seen in figure Figure 4-16.

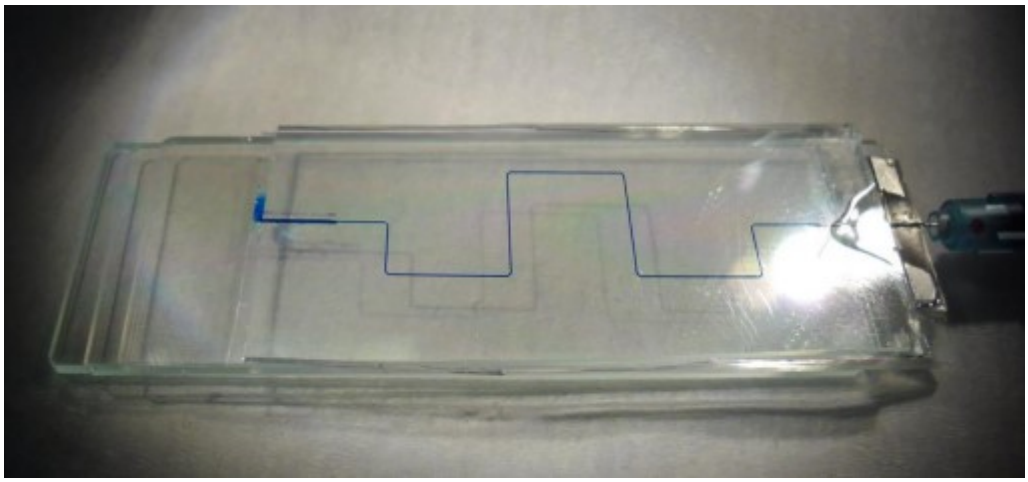

Figure 4-16, First generation channels (photograph by Dr Mike Arnold).

Devices produced from the photoresist method were dimensionally accurate, and could be produced in complicated 2D geometries. The devices were also produced in a clean room to ensure that no unwanted particles entered the channel or substrate. These devices had Luerlok fittings at each end, and were mounted to a microscope slide for rigidity. The fittings were implemented so syringes could be used to introduce fluids to the channel.

The syringe connectors and Mylar top layer were found to be unsuitable to this application. The syringe connectors did not bond into the PDMS well and thus did not seal. This resulted in fluid leaking through the gap around them. The connectors were also very delicate and were prone to falling out. The luerlok fittings did not interface with the required syringes, and often had large air pockets in them. due to the large differences in cross sectional area, a small depression of a mililiter scale syringe result in a very large displacement in the microchannel. Because air is compressible, the presence of the air bubbles in the channel resulted in unpredictable flow behaviour.

The first prototype devices were intended to be high capacity, and hold a large fluid volume inside the microchannel. To do this, the chip design was a large zig zag across the chip with many 90 degree corners. It was decided that this feature was not necessary. This greatly reduced the complexity of the design and allowed for simpler molding methods to be used.

4.2.4.1.2 Second iteration

Following the changes in design, Callaghan Innovation helped to produce some devices which were better tailored to the application. These devices had a single, straight, channel with input and output ports at either end replacing the Luerlok fittings. These ports would be made from 1.5mm OD 0.5mm ID flexible tubing. Tubing of these dimensions was selected as 22 Gauge syringe needles could easily be inserted into it, allowing for smaller volume syringes to be interfaced.

The first designs for this device involved bonding several PDMS sheets together to produce the channel. The PDMS sheets were bonded together by either surface treatment (high frequency plasma) or by placing them together midway through the curing process. These methods had mixed results, and the process where multiple pieces of partially cured PDMS pieces needed to be cut and rearranged was very complicated. In initial testing it was found that devices made this way did not form an effective seal.

High frequency plasma surface treatment was also applied to both the connection tubing and PDMS in an attempt to better bond the tubing into the channel. This was unsuccessful as the tubing would still detach from the channel. Some attempts were made to bond multiple pieces of PDMS together. However, limited success and low repeatability lead to this not being further perused.

4.2.4.1.3 Third iteration

As the previous methods were not successful, another method was devised which uses a removeable core threaded between two pieces of tubing. PDMS is poured around the core and cured. Once the curing is complete the blank piece is removed. The first attempts of this design improvised a 0.5mm IV needle as the removeable core (as seen in Figure 4-17).

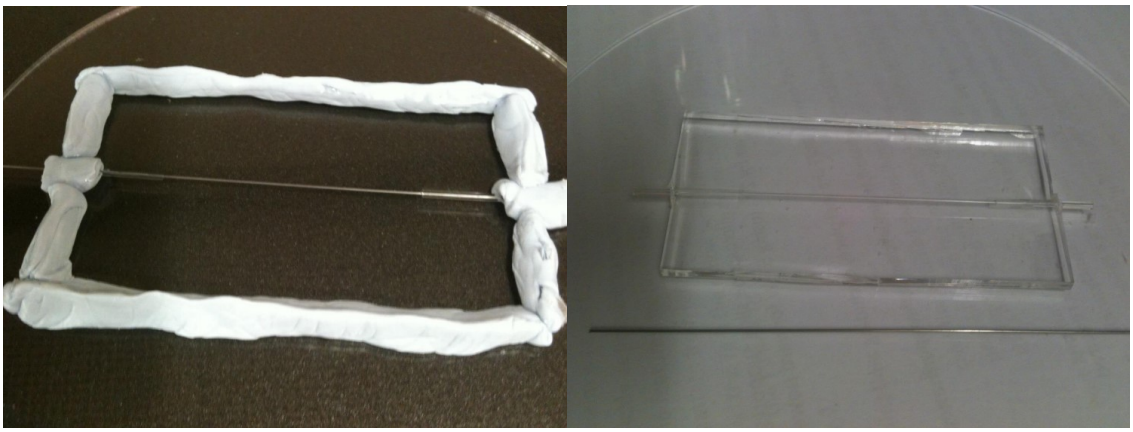

Figure 4-17, Mold set up for third channel design (photographs by Dr Andrea Bubendorfer)

This was the first functional channel produced for the project. It had a 500µm diameter channel cross section and was 60mm long. This device had several limitations, for example as with devices produced in earlier iterations, the tubing was poorly bonded into the channel, resulting in leakage. If the channel blocked, or was exposed to high pressure, the seals around the tubing would break, causing the tubing to detach.

The biggest advantage of this design was its simplicity. If a removable core with the dimensions of the channel can be sourced, a channel can be produced in this way. Very little equipment is needed beyond basic ovens and vacuum lines.

To minimise damage to the internal surfaces care must be taken when the core is removed. Although the PDMS will not form a strong bond to core, some small tears may occur,

damaging sections of the surface. This damage could possibly be avoided by selecting a core material which PDMS would not bond to, by coating the core in a lubricant, or by using a soluble core.

One disadvantage of this method, is that the top external surface is exposed to air and not constrained. While curing the PDMS is a viscous liquid, this means that it will run. If the mold is not level, the top surface will not be parallel to the bottom surface. This slight variance in the angle of the top surface can introduce additional optical aberrations to the system, and potentially reduce image quality.

This method of channel manufacture does fail to meet one of the channel specifications. There is no tilt angle between the external surfaces and channel. This precludes the system from operating as a tilted channel microscope without external tilt introduced to the system. The circular cross-section of the channel has the result that the objects in the channel are being imaged through a tilted cylindrical lens inside a tilted plate. As discussed in Chapter 3, a tilted cylindrical lens introduces additional optical aberrations. A tilted cylindrical lens is also harder to correct for with refractive index matching.

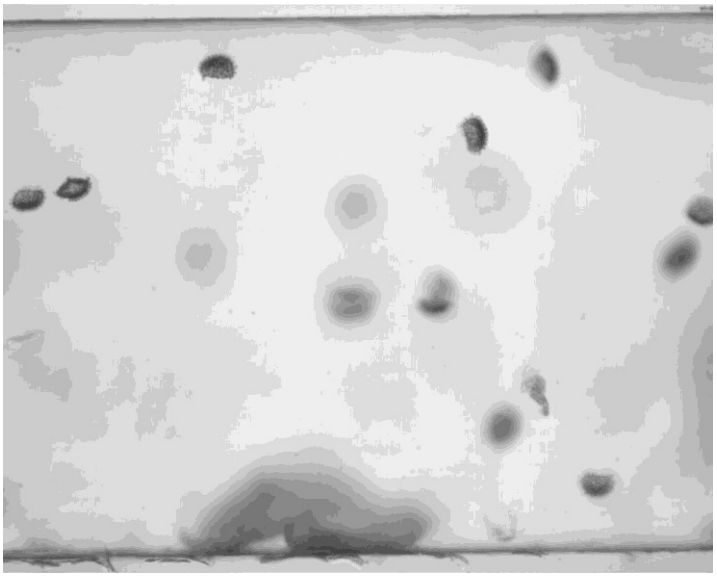

Figure 4-18, Lycopodium pollen inside 2nd generation PDMS channel

The first and second iterations of PDMS devices showed promise (images from a second generation device in Figure 4-18), however they had some bonding and sealing limitations. These devices also had some deficiencies in their optical design, which at this stage had not been fully considered by the author. The appeal of PDMS devices is due to the properties of the material and the simplicity of fabricating microchannels with it. A

low capital investment method for producing channels had been developed, however further development was needed to fully tailor the channel designs to the project.

4.2.4.2 Massey University channels

With help from Callaghan Innovation, a method had been devised for producing channels suitable for this application. Callaghan provided some PDMS for use to continue developing the process. These newer designs focused on adding features including tilt to the design and eliminating the limitations of the older manufacturing processes including the poor bonding of tubing to the PDMS.

The first change to the manufacturing process, was to introduce a method for tilting the channel through the PDMS substrate, removing the need to mount the device on an angle relative to the imaging system, and allowing simpler and cheaper optical corrections through refractive index matching. This ensures that as many optical interfaces as possible are perpendicular to the optical axis. Adding tilt to the design required changes to the mold design. Previously, the walls of the mold were constructed from Blu-Tack. This is a practical way of constraining PDMS during curing, however the tilt angle is introduced by holding the inlet and outlet ports at a controlled height and distance from each other and threading a flexible core between them. This change introduces the requirement that the mold walls needed to be machined so that the inlet and outlet ports can be accurately located.

The added accuracy required for the channel placement lead to the development of a reusable mold tool. This tool was comprised of a series of machined pieces, which fit together, and created a rectangular cavity to be filled with PDMS. The first mold was designed so that the channel would be angled at 20 degrees through the substrate. The plates of the mold tool were produced from both glass and PMMA. The glass surfaces were used to take advantage of surface molding accuracy of PDMS and produce a good surface finish on the top and bottom of the channel.

The channel was angled on the plane perpendicular to the base of the mold. This design feature was introduced to prevent bubbles from forming between the optical surfaces and the channel (in the path of the imaging system). Bubbles should move to the top of the mold during the curing process, which then becomes the side of the substrate when the device is in use (shown in Figure 4-19 and Figure 4-20).

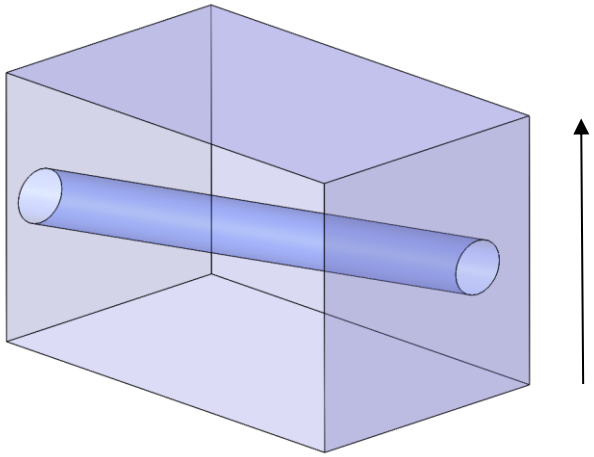

Figure 4-19, Orientation of channel during molding. Bubbles move to top, out of optical path when rotated.

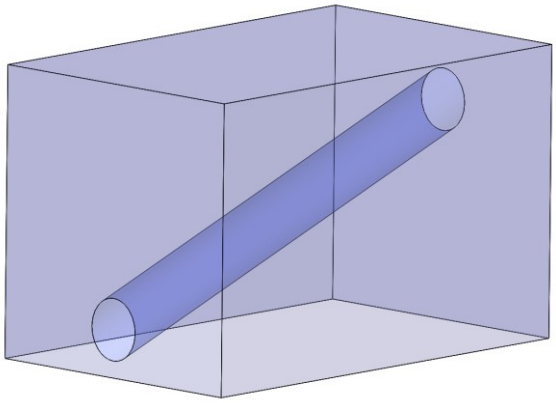

Figure 4-20, Channel orientation in operation.

With a more accurate mold tool, as used for producing these devices, the top surface is parallel to the bottom surface, and as such the only angled interfaces are the tilted channel surfaces. This tooling allows for the top thickness, that is the distance between top of substrate and channel to be controlled. The disadvantages of this approach are that the top thickness increases along the length of the channel due to the geometry of the situation (shown in Figure 4-21), and that the top thickness has to allow for 1.5mm OD tubing. Assuming the channel comes from the centre of the tubing, the minimum top thickness is >0.5mm above the channel top. This thickness limits the objective lenses which can be used to image the channel, as the working distance of the objective needs to be higher than the top thickness. This can be overcome with higher working distance objective lenses, however increasing the cost of the optics, to simplify the design of the channel may not be the most cost effective option.

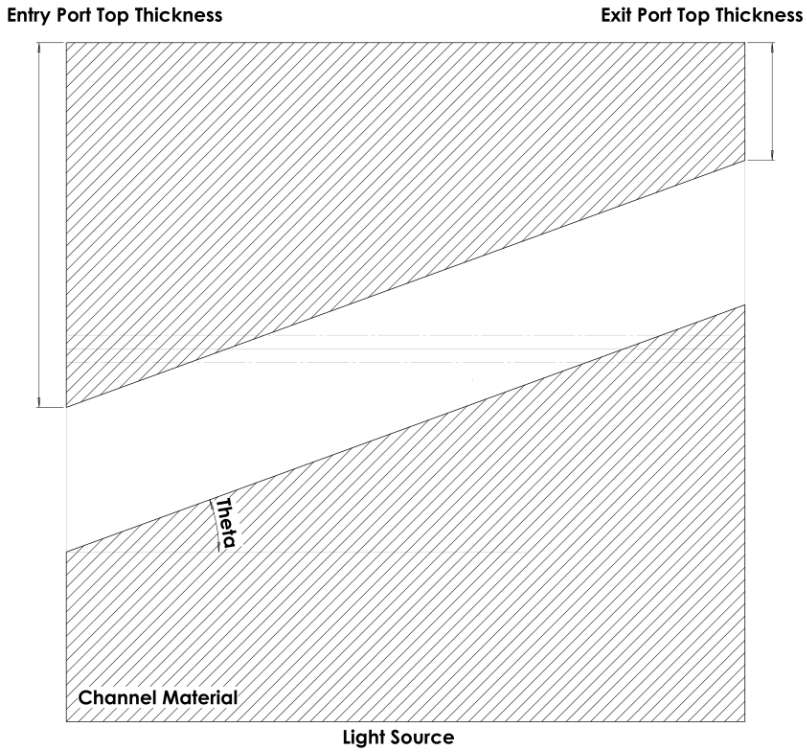

Figure 4-21, Increasing top thickness

The largest disadvantage of this channel design is the added complexity of the mold. This manufacturing method requires a multi-plate mold tool which has been designed to provide a specific channel length and angle, as well as a fixed minimum top thickness. Producing the tooling for this mold requires a competent machinist, and access to milling equipment. There is the potential to create this mold tooling in a variety of ways, however the method used in this case was considerably more complicated than the method developed with Callaghan. Provided the user knows the specifications and has access to machining equipment, the tooling is a small capital cost due to its reusability.

The weak bonds of the inlet and outlet tubing remain a problem with this design. This has the result that cleaning devices made with this method is more difficult and potentially damaging to the device: Pressure cannot be used to remove unwanted objects from the channel, as there is the potential to destroy the device.

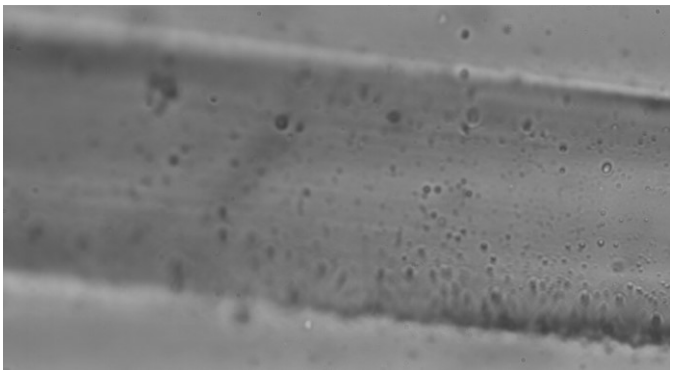

Figure 4-22, Surface finish of PDMS angled channel.

The devices produced through this method were the first ones which met all the requirements of an initial testing system. As detailed above they did have a number of limitations, however the addition of a tilt to the channel through the substrate was useful in reducing the optical aberrations in the system. Controlling the top thickness also helps reduce the potential complexity of the imaging system.

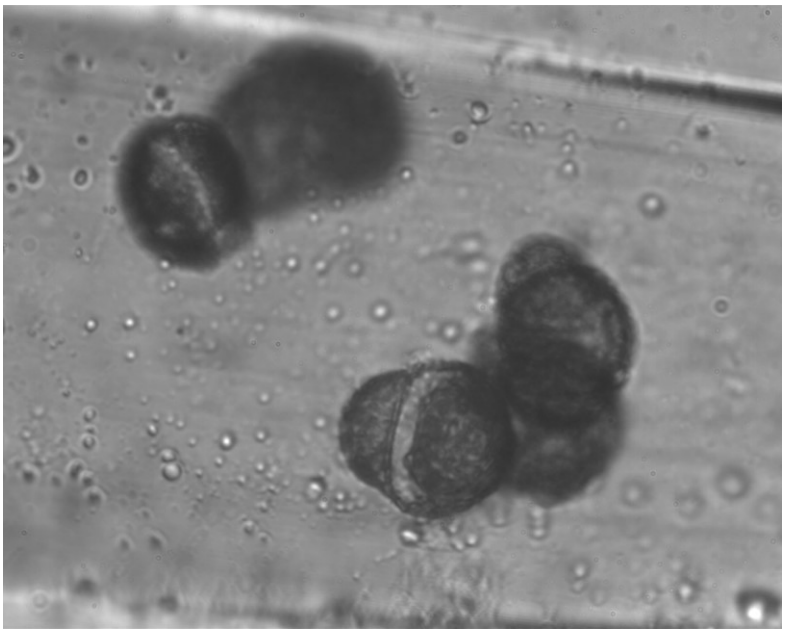

Figure 4-23, Pine pollen inside PDMS device.

Images produced from these devices (shown in Figure 4-23) were improved from previous iterations of the design. However, they still have a number of aberrations present. The round cross-section of the channel still acted as a tilted cylindrical lens introducing aberrations to the image. The quality of images also decreased towards the edges of the channel. The author suggests that this is because the angle of the curved surface was greater towards the outer edges (Figure 4-24).

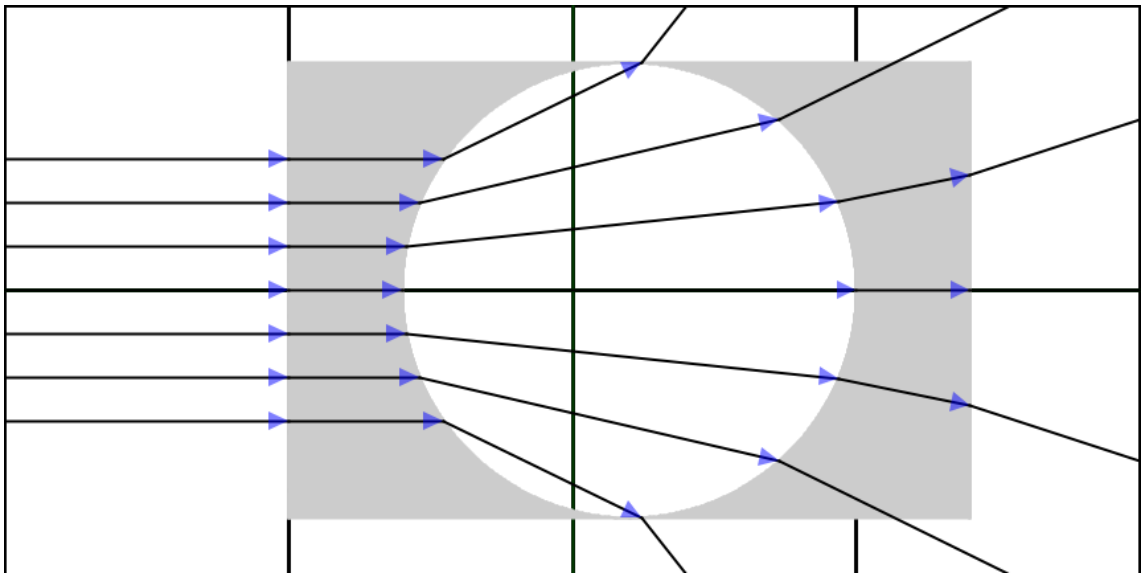

Figure 4-24, Planar wavefronts entering circular channel (Images produce with OpticalRayTracer 9.3)

4.2.5 PDMS bonded to PMMA

Continuing from the design work done with Callaghan, the author attempted to produce devices which were corrected for as many optical aberrations as possible, while meeting the functional specifications for a tilted channel in this application. The intention was to improve the current manufacturing method, rather than exploring additional materials. The aim was to use the low-cost benefits of the PDMS manufacturing method, while improving the optics and making the devices more robust to pressure and external forces.

The approach taken was to encapsulate PDMS in a PMMA shell. This could be likened to making the mold tool a part of the final product. PDMS was allowed to cure into a cavity in a single piece of PMMA. This approach was selected, as it combined the strength of a PMMA device with the acceptable surface finish, and optical properties of PDMS. Further optical improvements were made, by using flattened (rectangular removeable cores), produced from rolled copper wire. To do this, circular sections of soft copper wire were repeatedly dragged through a set of hard steel rollers set at an offset corresponding to the required channel dimensions.

4.2.5.1.1 Design

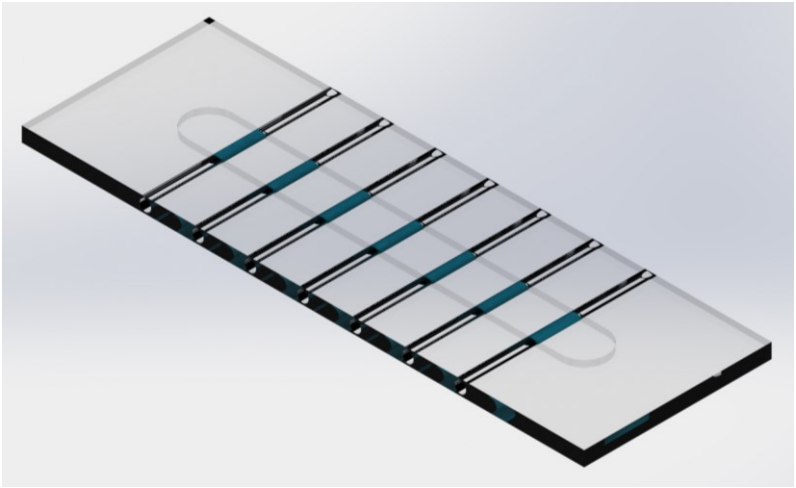

Figure 4-25, Multi-channel concept.

The device was designed to be the same length and width as a microscope slide, allowing a typical microscope slide holder to locate the device. Because the required channel length is very short (less than 1mm long, depending on the field of view), the channel can be orientated such that it runs the width of the device rather than length (shown Figure 4-25). To improve the cost performance of the devices, each device holds several channels running parallel to each other. This method improved the efficiency of making channels, as only a single PMMA piece needed to be machined for many channels. One rectangular core is still required per channel.

To accommodate multiple channels on a single device, the angled section could not be perpendicular to the to the top face. This has the result that bubbles formed during the curing process can obscure or damage the channels. To compensate for this, one cavity is left empty at the end of the device, and the device is cured on a shallow angle so that this empty cavity is elevated. This allows for air to escape away from the channel locations. Some bubbles do form as air can be trapped under the overlapping section of the design. Another degassing step once the PDMS has been syringed into the mold helps ensure that the additional bubbles will not form during curing.

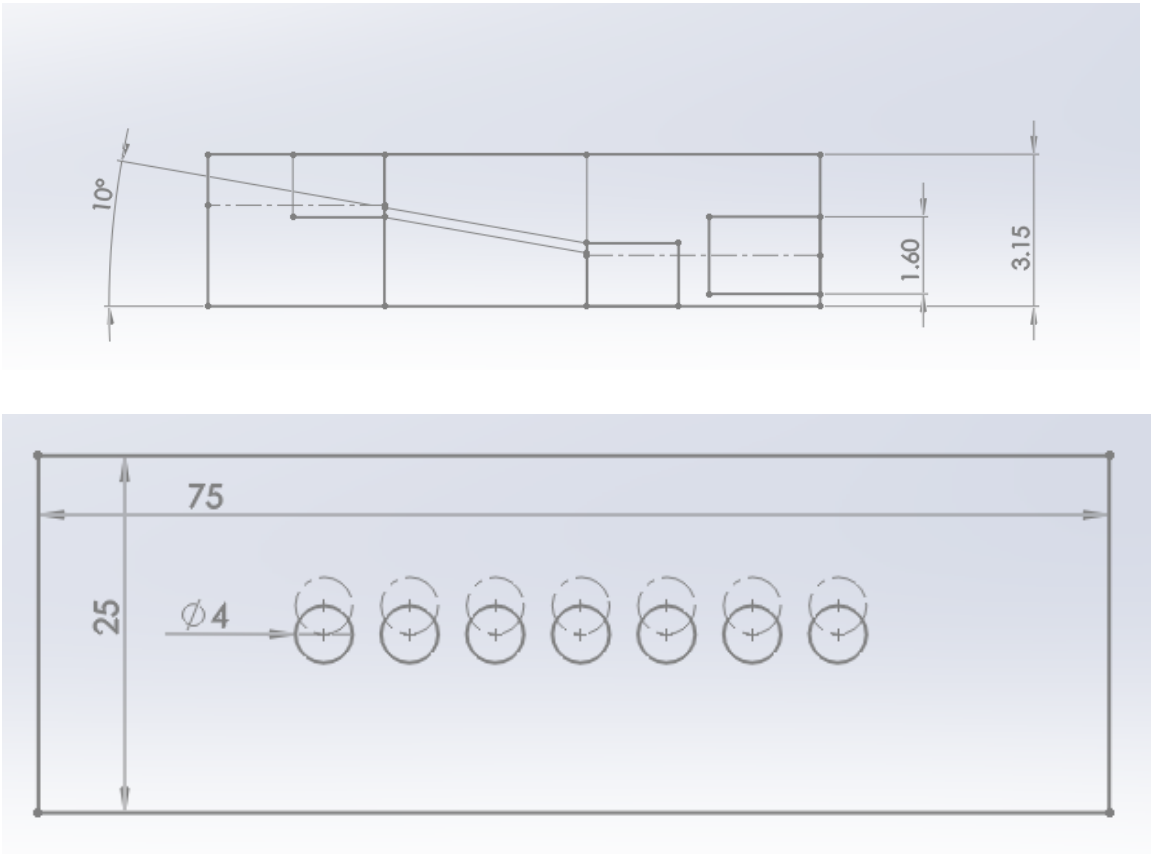

Figure 4-26, Hybrid PMMA & PDMS device geometry.

A downside to the hybrid PMMA and PDMS design, is that the PMMA part is no longer reusable and cannot be treated as a one-off tooling expense. Instead each time a device is made, a new PMMA outer shell must also be produced. This second set of operations adds to the cost per unit. The additional cost is offset by the multichannel design, however there should still be a focus of making the PMMA part as simple as possible. To this end the machining operations for the PMMA component were broken down into two sections, Milling and Laser Cutting. A commercial laser cutter can be used to reduce amount of manual machining required to produce the devices. This reduces the technician workload and by extension, the cost per PMMA component. While there is the potential to automate the drilling and step milling operations, the thickness variation of cast PMMA sheet can cause issues with drilling tolerances. A technician should manually assess each piece of PMMA prior to machining, to ensure the correct geometry can be achieved.

4.2.5.1.2 Fabrication process

A single piece PMMA outer shell (shown in Figure 4-27) is constructed. This is laser cut to the size of a microscope slide (25mm x 75mm), then slot milled to form a cavity for the PDMS. A series of 1.5mm holes are drilled into each side of the device. The height

offset between them allows for the rectangular cores to be threaded between them and form the angled channel.

The same 1.5mm OD tubing is then glued into each of the holes in the side profile, using the same Loctite adhesive as the previous PMMA channels. The tubing acts as an interface for syringe needles, allowing fluids to be introduced to the microchannel.

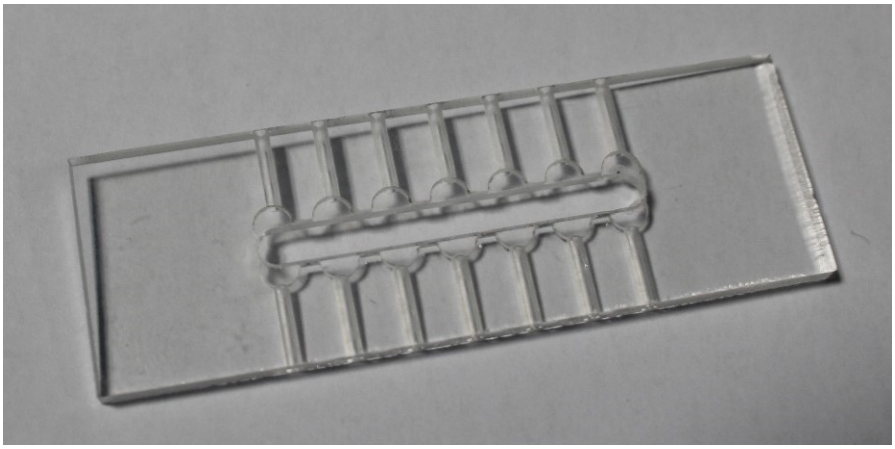

Figure 4-27, PMMA shell

A jig (shown in Figure 4-28) consisting of two bearings fixed 200µm apart, was used to roll 27 AWG (American Wire Gauge) copper wire to a 500x200µm cross section. Due to the possible imprecision of this rolling operation, a range of 250-500µm for the channel width and 180-220µm for the channel depth was accepted. Provided the channel angle is constant (the channel does not curve), the majority of objects would move through the focal plane, allowing the system to function as presented in Chapter 2.

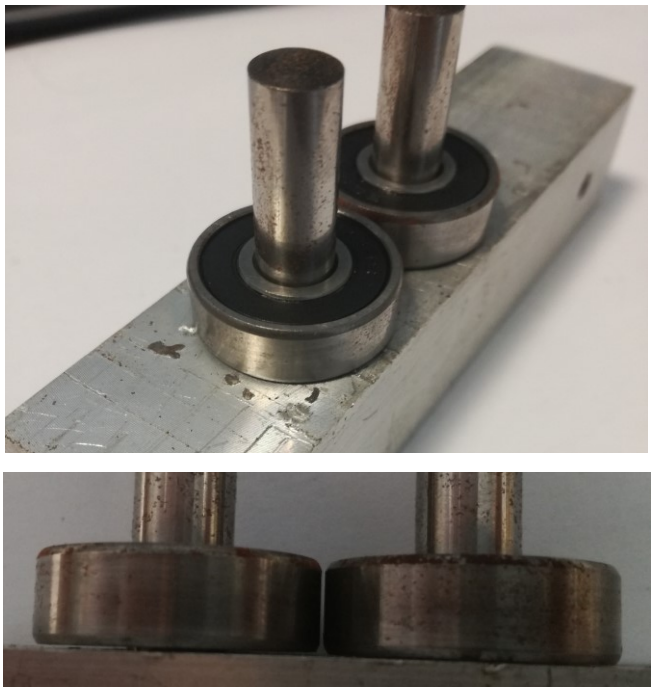

Figure 4-28, Wire rolling jig, rollers are 200µm apart.

The channel dimensions could be smaller than expected, to reduce the risk of blockages the filtering method for samples was altered to only accept objects smaller than 100µm in minor axis length.

The rolled wire cores do not have perfectly rectangular cross sections (shown in Figure 4-29), as only the two faces in contact with the rollers will be flattened. The other surfaces of the wire are likely to retain some curvature. For this reason, the optics of the channel will not be ideal at the edges. Only a small proportion of the objects will flow in the regions which are rounded (due to boundary layers and edge effects), as such this will not have a significant negative effect on performance. If truly rectangular cores could be produced or sourced by another method, this limitation could be eliminated.

Figure 4-29, Rolled wire profile (dimensions in µm).

4.2.5.1.3 Assessment

The surfaces in the channel are not perfect. Imperfections from the molding process are visible and can impact image quality as objects move through damaged regions of the channel. The damage is seen as regions of dark texture on the internal surfaces of the channel (shown Figure 4-30). These regions can be considered part of a background, and easily removed from images as fixed pattern noise, where objects are obscured by these regions there is still the possibility that some information may be lost. It should be noted that the UOSA machined PMMA channels have a superior surface finish in this regard.

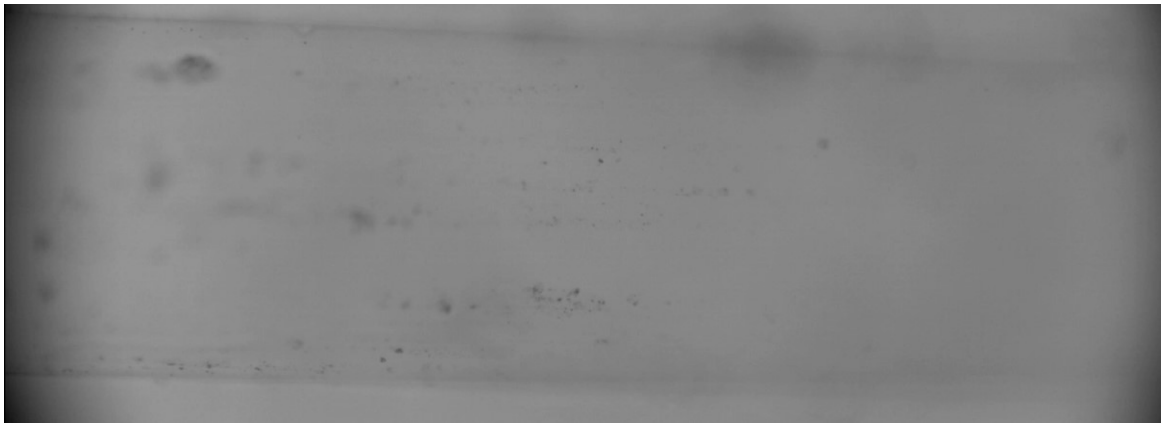

Figure 4-30, Internal surface damage visible as dark regions.

Because the faces of the rectangular section are the only angled interfaces in the system, the only additional step required to reduce the optical aberrations of this system, is to match the refractive index of the channel material to the carrier fluid passing though. This can be achieved due to the low refractive index of PDMS. In the test system, the magnitude of the optical aberrations is reduced to the level where that images can be captured close to the diffraction limit of the imaging system. This is the outcome that was desired when attempting to produce a physically robust device with better optical qualities.

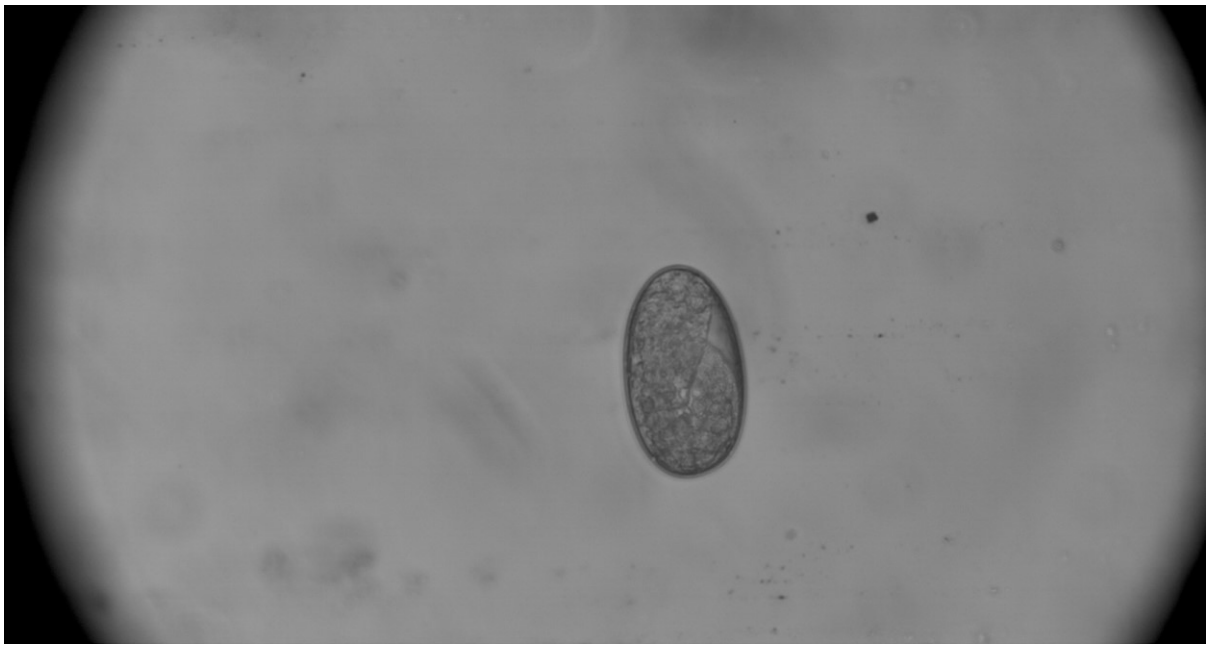

Figure 4-31, Image of nematode egg inside channel (20X objective)

Devices produced using this method remain low in cost, while being more resistant to external stresses and producing less distorted images than the previous iterations (seen in Figure 4-31). The PMMA sections of the device add machining steps to the fabrication process, and increase the cost per unit. The increased cost is offset by the multi-channel design which enables devices to be used multiple times, and reduces the cost of channel blockages. These hybrid devices appear to handle pressure better than the previous iterations, however due to time constraints the destructive testing required to validate this tentative conclusion was not carried out.

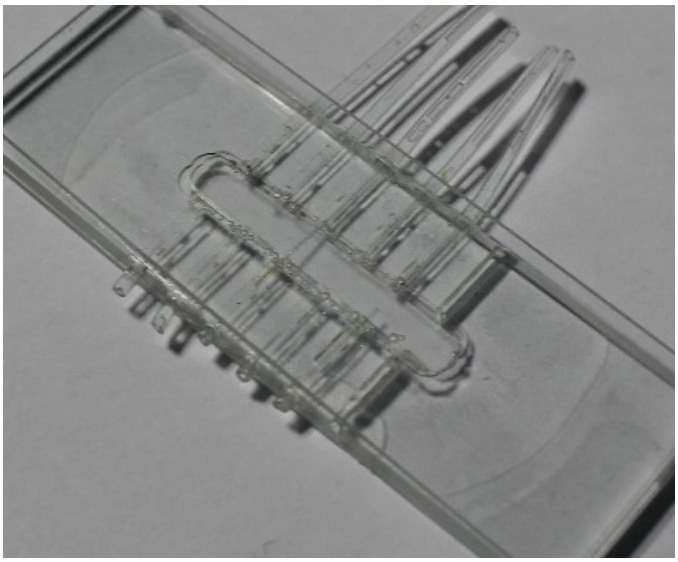

Figure 4-32, Final microfluidic device

4.3 Material suitability and conclusions

Material	Microchannel Fabrication Methods and Costs					
	Fabrication Method	***Cost per device***	***Capital Investment***	***Design Flexibility***	***Surface Thickness***	***Refractive Index***
Glass	Chemical Milling	$500	High	2D design	0.15mm	1.45 – 1.96
PMMA	Milling	$350	>$100,000	Restricted by tooling	1mm	1.47-1.49
PDMS	Molding	$10	<$100 + tooling	Restricted by tooling	0.15mm	1.406
COC	3D Printing		High	Not Restricted	<0.1mm	1.53

Table 4-1, Comparison of materials for microchannel fabrication. [63-66]

This chapter discussed several of the methods available for producing microchannels. These methods and materials represent a subset of the available solutions given the budget and time constraints of the project. While many methods can be adapted to the process of producing the required device, some are better suited than others. A breakdown of the relevant information can be seen in tables 4-1 and 4-2.

Material	Refractive Index Matches		
	First Match	***Second Match***	***Third Match***
Glass	Silicon oil	Zinc iodide	Sodium iodide
PMMA	Para-cymene	Zinc iodide	Sodium iodide
PDMS	Glycerol Solution		

Table 4-2, Materials and refractive index matches [44, 67]

PDMS devices have the lowest cost to manufacture out of all devices considered in this chapter. They also have the most convenient refractive index match with aqueous glycerol solutions. PDMS devices manufactured using the wire core removal method have an acceptable surface finish, however this surface contains more irregularities than machined PMMA, or PDMS channels produced from laser etched soft lithography.

PMMA devices have the potential to be adapted to the application, however the cost per unit is considerably higher than PDMS. These devices are more robust than PDMS and can withstand higher pressures.

The Hybrid PDMS-PMMA design is a compromise between cost and performance. These devices are more robust than the pure PDMS design, however, they have the increased

cost of machining the PMMA component. Because of the adequate optical performance, reliability, and cost, these devices were adopted for the remainder of the project. It is estimated, that using the equipment available in the university, the cost to produce one of these devices is as low as $10. This cost could be reduced if channels were made in large quantities or batches.

Chapter 5. Software

5.1 Software Description

5.1.1 Introduction

A software package was developed to control the system. The aim was to provide a package which automates several of the tasks for the user. This software will control hardware systems including the lighting, and camera. Image acquisition, memory management, processing, and data display will be automated by the software. Required user input includes: background selection, starting and finishing samples.

5.1.2 Constraints

The software described in this chapter was developed for the nematology application, as both an egg counter and classifier. Further details on the constraints from this application are listed in the 'Nematology' section (1.41).

When counting objects of interest, the system must collect images of each object which passes through the FoV. If objects of interest are missed the reliability of the results is reduced.

In the nematology application, the camera will provide data at a rate of 300MB/s for a period of six minutes, producing a total data volume over 100GB. This data must be managed either through compression or real time analysis, as storage of multiple data sets would be inconvenient.

The operator of the machine will likely be a laboratory technician or researcher. It is assumed that the user may have a minimal level of computer literacy, so will require the software to be simple to operate and understand. Minimal training should be needed to learn the operation of the machine.

5.1.3 General Approach

There are two distinct sections to the software developed for this project, real time, and offline. The two sections were developed as separate code bases. The real-time section of the software is the image acquisition system that interfaces with the camera. This consists of processing frames as they are received from the camera, and the associated memory management.

The offline software handles the post capture processing including: image processing, feature extraction, classification, and counting. As the offline software is not operating on frames as they are received, the timing constraints are less stringent.

This chapter will discuss how these sections of software were implemented, and the degree of success of the implementation. To avoid confusion, a physical object moving through the sample stream will be called an 'object of interest'. All other use of the word object, will relate to object orientated programming. Figure 5-1 outlines the software process described in this chapter.

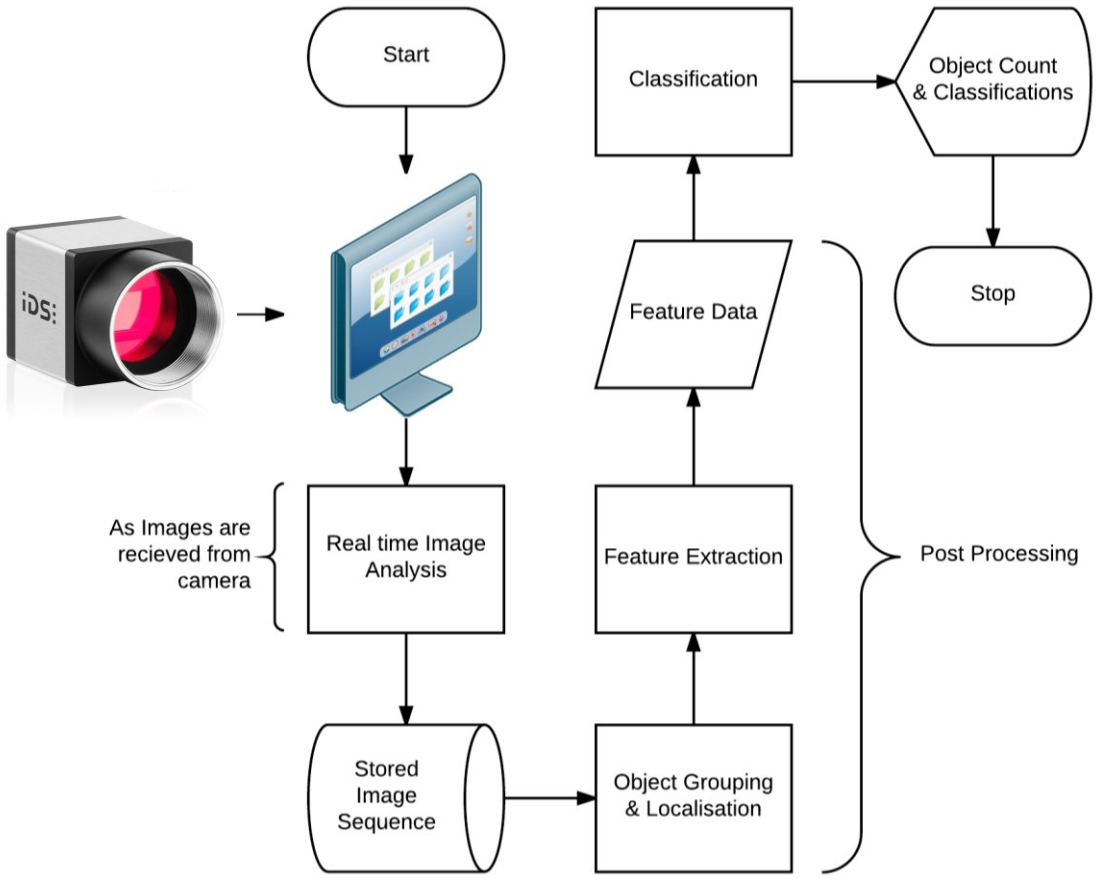

Figure 5-1: Software process Flow.

5.2 Real Time Software

5.2.1 Image Acquisition

When operating the camera at its maximum frame rate of 150fps, all operations on a frame will need to be completed before the next frame arrives (6.7ms). As stated above the data rate from the camera is 300MB/s, with a total data volume in a six-minute period of 117GB. Modern computers can support systems with more than 128GB of memory [68],

however consumer equipment with this much memory is still expensive. The development system, an HP Z220 workstation, had 16GB of on board memory, this amount is more typical of a consumer level work station.

Because the volume of data exceeded the system memory, an algorithm needed to be developed which would enable the collection of complete data sets. The following options were considered:

1. Write every frame from the camera directly to disk as a 117GB file.
2. Compress the video substantially through some means.
3. Save only few frames from the sequence.
4. Save only regions of interest from the camera.

Option one required a hard disk with 300MB/s sequential write speed, this is standard with a modern SSD [69], however storing data from multiple trials will quickly fill the drive.

Option two requires the compression to occur as the images are received from the camera. There is also the potential to lose information and introduce artifacts in the compression.

Option three assumes that only a fraction of frames contain objects of interest. Excluding these frames from the stored sequence reduces its size. This method requires the detection of objects of interest in real time, adding complexity to the image acquisition.

Option four only stores partial frames where objects have been detected, this is an expansion of option three, however also requires localisation of the objects of interest.

All four options are feasible methods for handling the volume of data generated in a sample. The concentration of objects of interest in the sample fluid is low, therefore most of the frames captured will contain no objects. Therefore, option three provides an adequate reduction in total stored data. A sequence of only frames containing objects of interest can be stored in memory and then written to disk for further analysis. For development, the author wished to keep as much of the raw data as possible, allowing for flexibility when selecting an approach for subsequent analysis.

5.2.2 Approach

To keep only frames occupied by objects of interest, each frame is processed in real time. This process consists of:

- Down sampling
- Background subtraction
- Binarization
- Morphological filtering
- Assessment against a fixed threshold

Down sampling expedites the subsequent steps in the process by significantly reducing the volume of data that requires processing. Fixed pattern background subtraction produces a foreground image. The foreground is binarized and morphologically opened to remove small objects and noise. The count of the pixels remaining in the image is compared to a threshold; images which exceed the threshold are stored.

This software was developed in C++ because it is a compiled language with a high level of support. OPENCV (Open Computer Vision) [70] libraries are available in C++, which reduces the development time by providing image processing functions and tools. OPENCV has seamless integration of OPENCL (Open Computing Language), a parallel processing framework, which leverages GPUs (Graphics Processing Units). OPENCL supports a range of devices from numerous manufactures including both AMD and Nvidia (the two leading desktop GPU manufacturers) [71].

Processing with a GPU can accelerate the execution of algorithms which, lend themselves to parallel implementations (most image processing operations) [72]. OPENCV supports these parallel implementations through the UMat class.

The software was developed in Visual Studio Community 2015 (VS). VS has a number of timing and performance tools which were used to assess algorithm run time, and CPU and GPU loading.

User input and data display is executed in a separate thread to the processing and frame collection. This ensures that the user interface does not impede performance. Thread management was handled through spin locks, and atomic variables.

5.2.3 Process

The real time process is shown in Figure 5-5.

1. The camera is initialised with a fixed frame rate and exposure time.
    a. The exposure time is calculated from the maximum linear velocity of the objects in the sample stream to reduce motion blur. Objects should travel less than one pixel during the exposure period.
    b. A circular buffer is set up in the system memory to store frames as they are read from the camera.

2. A vector is set up to store images in. Kept frames will be appended to this to form a 3D array of 2D images.
3. The process receives and displays frames from the camera continuously to the user.
4. The user selects an image from the camera feed to use as a background.
    a. (continuous) background estimation and update is more robust to changes in the background (such as objects being deposited in the channel), however this was not implemented due to the longer computation time required.

5. Sample processing begins
6. Every image is copied and down sampled by a factor of four (in each direction).
    a. This down sampling is acceptable as the objects of interest are large enough that they will not be removed in the process.
    b. To save computation time a decimation filter is not used in the down sampling. The down sampled image is every 4^{th} pixel of every 4^{th} row of the original image.

7. A down sampled version the background image is subtracted from the current frame, producing a foreground image, shown in Figure 5-2.

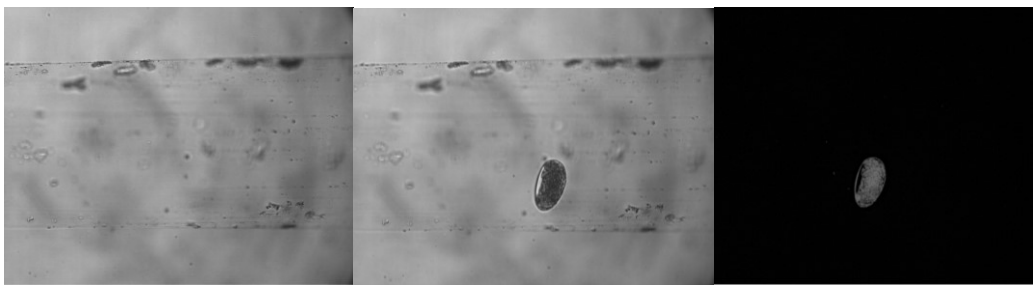

Figure 5-2, Background Subtraction.

8. The foreground image is then binarized with a fixed threshold.

Figure 5-3, Binarized image of nematode eggs (Left: without background subtraction, Right: after background subtraction).

9. The binary image is then morphologically opened (eroded then dilated) with a 5x5 square kernel.
    a. This removes any small blobs in the foreground image.

Figure 5-4, Morphologically opened binary egg image.

10. The pixel values of the filtered image are then summed and compared to a fixed threshold (based on expected object size).
11. If the sum is higher than the threshold, the image may contain an object of interest and is appended to the image vector
12. When then sample fluid has passed through the imaging system, the user stops the process.
13. The user can review all saved frames to validate that there are no discontinuities in the data set.
14. The image vector is written as a video file with a user selected FourCC codec.

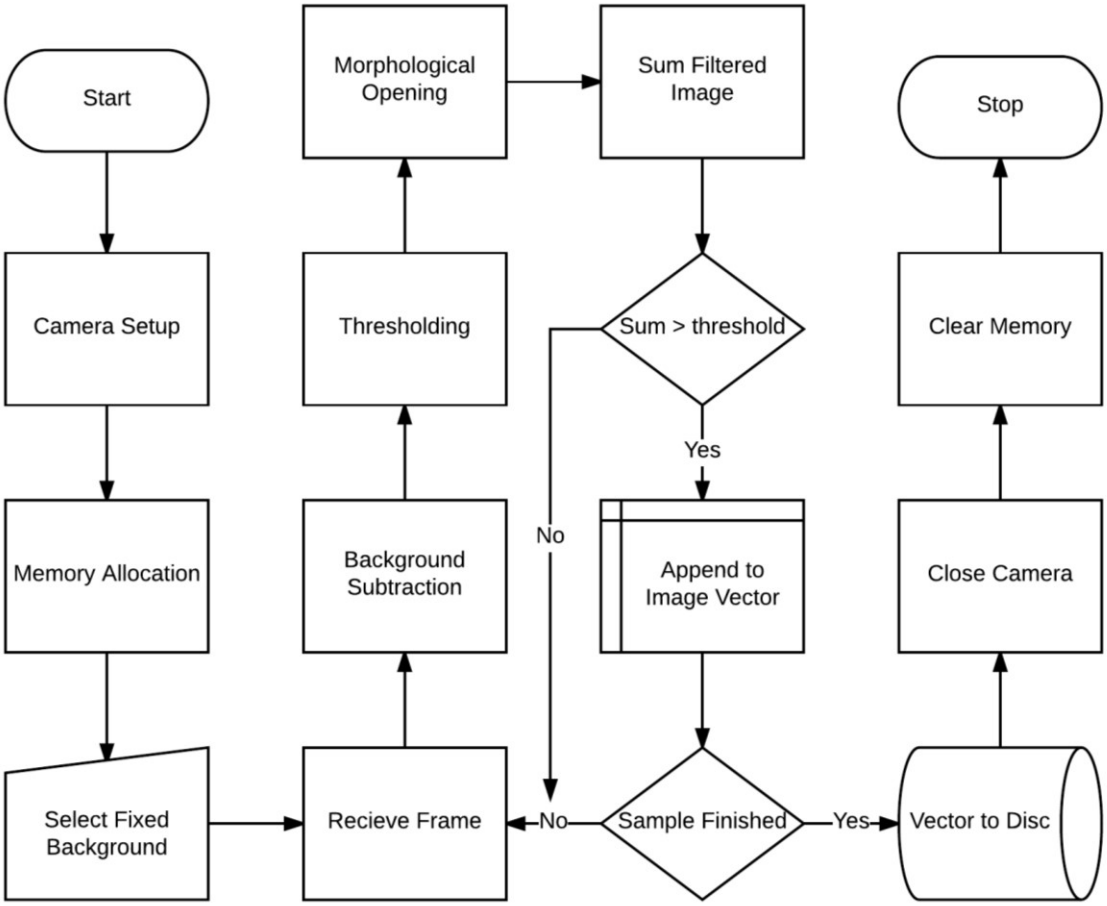

Figure 5-5, Image acquisition flow diagram.

5.2.4 Results

Using the same dilution factor as the McMaster method (with a volume of 300uL and a multiplication factor of 50), counts of infections up to 18,000 eggs per gram can be completed with less than 16GB of data. Data reduction for a six-minute run (period used for development purposes) from 117GB to under 16GB is achievable if the concentration of objects in the sample fluid is no higher than 1.2 particles per microliter (at 20 frames per object). This is calculated below.

$$Data\ per\ frame, D = \ 2.044 \times 1.088 = 2.224 MB \tag{18}$$

$$Data\ per\ egg = D * number\ of\ images = 2.224 \times 20 = 44.55 MB \tag{19}$$

$$number\ of\ objects, n \ = \frac{16{,}000}{44.5} = \ 360 \tag{20}$$

$$Concentration = \frac{n}{V} = \frac{360}{300} = 1.2 \quad (21)$$

These equations over-estimate the total data, as not all objects of interest in the sample stream will be traveling at the same linear velocity.

Increasing the dilution and multiplication factors can increase this upper limit. Further data reduction through the addition of options two and four (as described in 5.2.1) could also extend the limit.

OPENCV does not support video storage for files larger than 4GB (.AVI wrapper limit). This is overcome by writing the file in sequential sections, or as a set of images.

Changes in the orientation of objects of interest during imaging can cause the detection algorithm to fail. If the object rotates to a position where it falls below the detected size it will not be stored, this behaviour is illustrated in Figure 5-6.

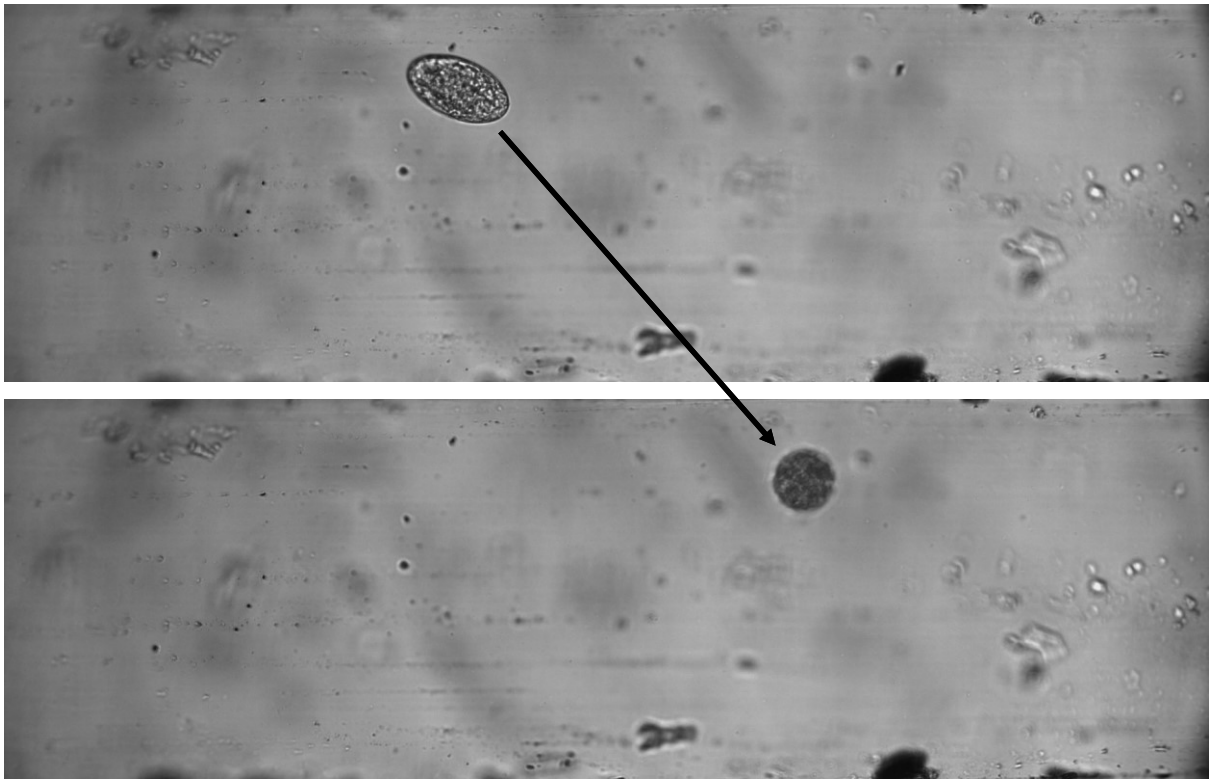

Figure 5-6, Shows an object of interest rotating as it is imaged. Rotation perpendicular to specimen plane, causes different projections of the object to be imaged, these projections will differ in area.

Some frames are torn or missed because of the limitations of the USB3 interface and CPU sleep states (this could be rectified by use of a real-time operating system (RTOS)). If the CPU is busy or in a low power state when the USB3 needs servicing, frame data can be

missed or corrupted. Torn (as shown in Figure 5-7) and missed frames negatively bias the data and invalidate counts. Disabling the C1-3 sleep states and running the USB3 below maximum bandwidth can remove this problem. Reducing USB3 bandwidth reduces the maximum frame rate and increases sample time.

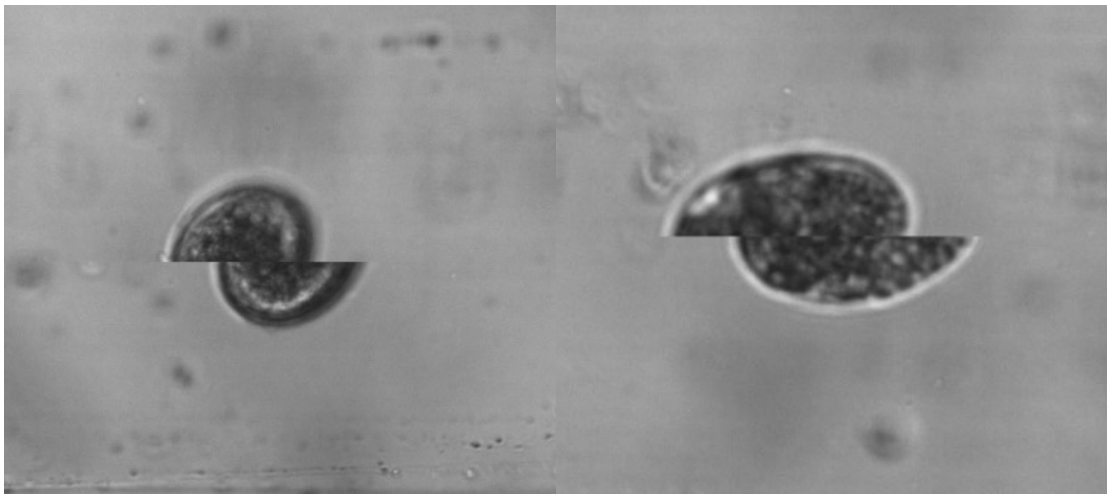

Figure 5-7, Examples of frame tearing during image acquisition.

Three representative data sets were randomly selected to compare the number of captured frames in the sequence to the number of corrupted images (duplicate or torn frames). Table 5-8 shows the number of frames from a captured sequence which were corrupted. Errors in the frame collection process typically occur in less than 1% of acquired frames. Assuming all objects are imaged as they move through the system, the probability all frames associated with a given object will be corrupted is very low.

Data Set	Discontinuities per thousand	Number frames	Proportion corrupt	Proportion acceptable
1	8	860	0.01	0.99
2	10	747	0.01	0.98
3	5	1145	0.004	0.99
Mean:	7.67	917	0.009	0.99

Figure 5-8, proportion of frames corrupted during data capture.

Two 4GB data sets were captured while objects passed through the channel. These sets were not compressed and consisted of 4100 frames each. The number of frames containing objects of interest was manually counted. The data sets were then processed by the real-time blob detection algorithm to verify its effectiveness. The results of this are shown in Table 5-9.

Sequence	Number Frames	Number frames with info	frames kept by algorithm	Difference
test 100	4099	424	498	74
test 100 2	4099	467	472	5

Figure 5-9, Frames collected compared to frames of interest

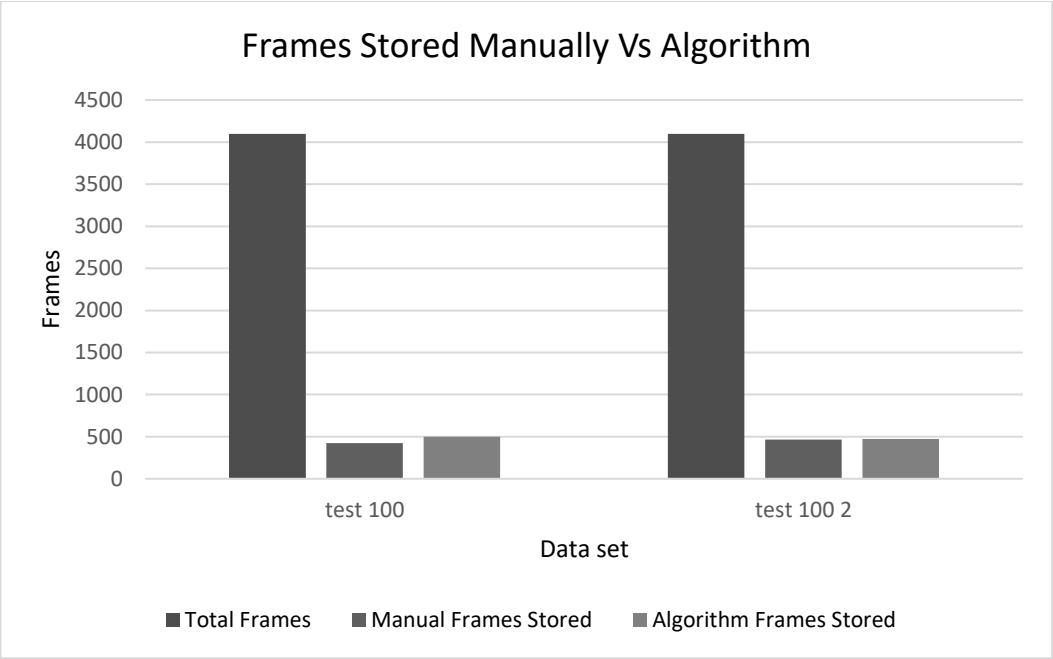

Figure 5-10, Comparison of frames stored in manual analysis against algorithm.

The number of frames kept compares well to the number of frames manually selected. The difference between the frames kept by the algorithm and those manually selected may be due to the algorithm detecting smaller objects than the viewer. For example, an object on the edge of the field of view will typically increase or decrease in size over several frames as it moves in or out of view. Based on a fixed threshold, the software will determine consistently when to store frames, while a manual assessment of this will be less consistent and subjective.

Also, a single 4GB raw data set was captured as carrier fluid without objects flowed through the channel. No frames were stored, this demonstrates that when objects are not present in the stream, the process will not store images inadvertently.

5.3 Offline Software

The stored image set is processed to classify the objects of interest, and generate an egg count. Two stages of analysis are performed. Possible egg images are grouped, then features are extracted for use in classification.

5.3.1 Image Processing and Feature Extraction.

A number of images will be captured for each object of interest, these images must be grouped and localized for feature extraction and subsequent classification

As the objects move along the channel, each image of an object of interest will represent it in a different orientation and focus. The difference between the images must be sufficiently small for them to be correctly associated with the corresponding object of interest.

5.3.2 Approach

This section of the software was developed in MATLAB because it has available a wide range of tools for classification, and image processing. MATLAB uses just-in-time compilation to execute faster than interpreted languages. MATLAB supports object orientated programming, so a number of classes were developed to handle the data during processing.

Background subtraction, binarization, and morphological filtering operations are applied to the data. 3D centroid coordinates are generated for each blob detected in the filtered images. These coordinates are used to associate blobs with corresponding objects of interest. A set of features is extracted from each image to use in classification. A tailored feature set, which will be discussed further in section 5.3.5.1, was selected to be representative of features used in the literature of this application. Principal component analysis (PCA) can be used to help identify which features account for the significant variation within the data [73].

5.3.3 Steps

1. The video sequence is read into Matlab as a 3D array of 2D frames.
2. The first frame in the sequence (frame(:,:,1)), is designated as the background image.
3. The background frame is subtracted from each of the other images to give an array of foreground images.
4. The foreground images are binarized.
5. Each binary frame has a blob detection process performed on it.
6. Each blob above a size threshold has the following features extracted. (additional features are extracted from fused images).
    - Major axis length
    - Minor axis width
    - Major axis angle
    - Area
    - Eccentricity
    - Centroid
    - External contour
    - GLCM properties
    - Contour Features
7. A 256*256 window is extracted from the foreground frames centered on the centroid of each blob detected. A stationary wavelet transform (bior4.4, level 5) is taken and stored. This window is taken from the centroid of the blob in the binary image.
8. Blobs are grouped into particles (a particle is a collection of the blobs associated with an object of interest)
9. The wavelet transforms of each image in a particle are combined to form a compound image.

5.3.4 Data Structures

For any given sample there can be between zero and hundreds of objects of interest. As the sampling rate is changed, the number of images for each object of interest can range from one to tens. Therefore, the classes and methods used for image processing need to be flexible and avoid unnecessary memory overhead.

The classes need to provide a logical data flow from the raw data to a set of grouped features. Tools were developed (as methods) to show the user how the processed information is extracted. A full description of the classes used for image processing and feature extraction can be found in Appendix III. Code samples can be found in Appendix IV.

5.3.4.1 Simple Class descriptions

The following classes were developed for handling the data generated when a sample is processed.

Sequence Class

The sequence object is a container which holds the video sequence, the background image, and the enhanced versions of the video sequence.

objectImage Class

The objectImage class is a container which holds all the properties, references, and data associated with each blob detected in the data set.

imageSetArray Class

The imageSetArray is a container for all the objectImages. This class finds each object images and constructs an array to contain them. A number of tools and techniques for examining the object images are also implemented in this class.

particle Class

Each physical object of interest viewed by the system will be imaged a number of times, each physical object will have a number of objectImages(blobs) associated with it. A 'particle' is a representation of a physical object of interest, as a number of images and their associated features. This object is a container for grouping all the objectImages of the same physical object of interest.

particleArray Class

A container for all the particles in the sequence.

5.3.5 Software Techniques

5.3.5.1 Calibration

To accurately measure the size of eggs imaged by the system some calibration is required. A number of spherical objects of known size were imaged and measured to produce a "millimetres per pixel" calibration value.

5.3.5.1.1 Test Objects

The most accessible spherical objects of an appropriate size were 22.6µm nominal diameter Palynospheres. Palynospheres are markers which can be placed in palynology slides to assist in pollen counting. These spheres come in several grades based on size

and tolerance. ‘Orange’ grade spheres were used for calibration. The spheres have a size variation of ±2µm. To account for this, approximately 83 spheres were imaged, with the mean size taken for calibration.

5.3.5.1.2 Procedure

The procedure for performing a calibration was broken into two steps. First a solution of spheres was made up, then imaged and measured. The solution was prepared from:

- 0.008g of Palynospheres.
- Tween 20 Polysorbate.
- 143g Sodium bromide.

A small quantity of Tween 20 at a 0.05 V/V concentration was used to wet out the Palynospheres. The spheres were then placed in a sodium bromide solution with a density of 1.28g/cc. A few ml of the sodium bromide solution was pipetted onto a slide to be imaged.

83 spheres were measured. The radius of each sphere was measured by thresholding the images, determining the area of each circle and the diameter from it.

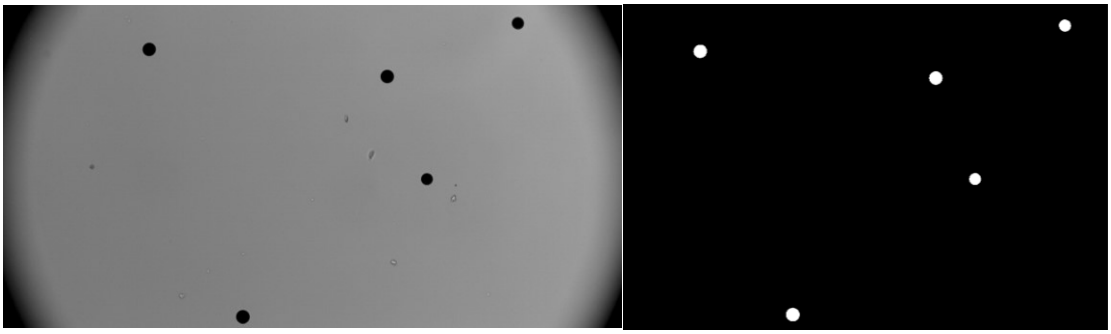

Figure 5-11, Raw image of Palynospheres and binarized version (left: raw image, right: binarized image).

The mean measured diameter was then divided by the expected 22.6µm to produce a figure of 0.5080µm per pixel.

5.3.5.2 Features

Many features can be extracted from the stack of images collected from each egg. Some of these features will better describe the object, or be easier to measure depending on which images in the set they are extracted from. For example, the size of an egg as defined by major axis and minor axis length, is best observed in images with the highest aspect

ratio (shown in Figure 5-14). While texture information is best presented in focused images of the contents of the egg.

Pre-existing MATLAB functions, and some simple tools were used to extract features detailed below from the images.

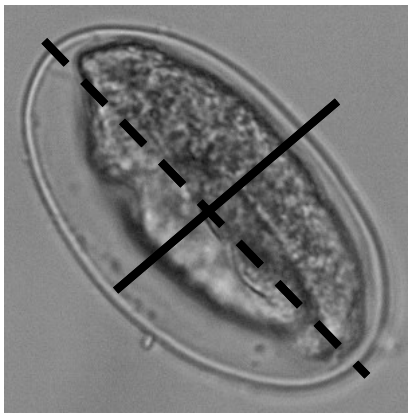

Figure 5-12, Major and minor Axes of nematode egg (Major axis shown as dashed line, Minor axis shown as solid line).

To best describe the eggs, and help mitigate the artefacts introduced in the fusion process, three different feature sets were extracted from different parts of the image stack.

- Fused image
  - Texture
- Maximum Focus
  - Contour
- Maximum Aspect ratio
  - Area

5.3.5.2.1 Texture

Literature has shown that texture information can be used to classify nematode eggs with a high degree of success. In this application texture information is extracted as features from the GLCM. As explained in section 1.4.2.1.2, the GLCM is a measure of the frequency of occurrence of specific pairs of pixel values.

5.3.5.2.2 Contour

As shown in [16], the edge profile of an egg can be extracted as a function of the radius relative to angle. For an ellipse this profile will resemble a sinusoid, the Fourier transform of this can be taken, and its energy distribution used as a feature. As an elliptical object will not have any sharp changes in curvature, the highest gradient of the contour can potentially be used as a feature. This feature may break down in situations where objects

are not properly segmented from the background, or when a complete contour can not be obtained.

5.3.5.2.3 Area

The width, length, and area can be of interest when determining the species of egg. The distribution of sizes in a sample can indicate the presence of different species. Aspect ratio, eccentricity, and solidity are useful shape features for elliptical objects. The aspect ratio is relatively constant for nematode eggs and is expected to be useful in assessing if a potential object is an egg.

Solidity, measured as the area of the egg over the convex area indicates how well the object fits inside the convex hull. A high Solidity indicates that the convex hull and the shape itself are very similar. In situations where there is damage to the eggs outer shell (Figure 5-15), this will translate to an increased difference between area and convex area.

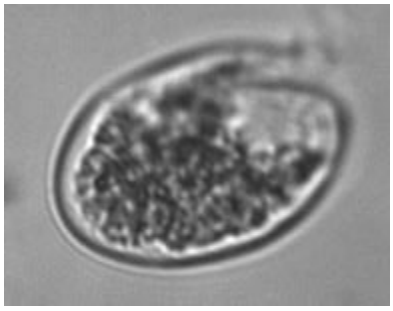

Figure 5-13, Egg with damaged shell.

5.3.5.3 Wavelet based image fusion

Each *objectImage* object has as a property a 256x256 stationary wavelet decomposition. Each *particle* has a fusion image synthesised from the decompositions. The fusion image is produced by comparing all the decompositions at each point with a maximum absolute operation. A full description of the wavelet based image fusion method can be found in [74]. An example from a palynology application (nematode eggs were substituted for Lycopodium) is shown in Figure 5-16. Objects of interest rotating during image capture cause this method of image fusion to break down, as shown in Figure 5-17.

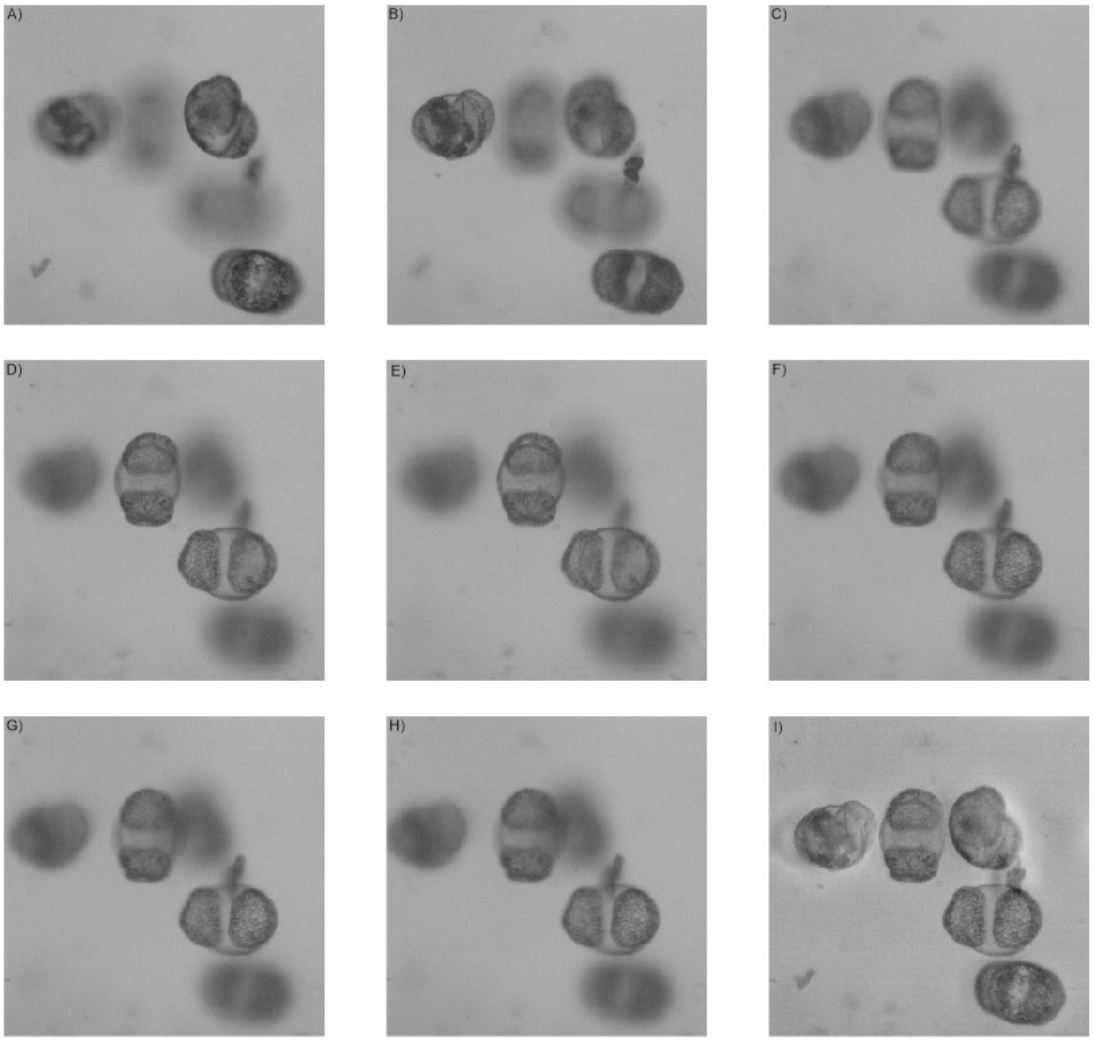

Figure 5-14, Wavelet based pollen fusion (A-H focal stack, I fusion)

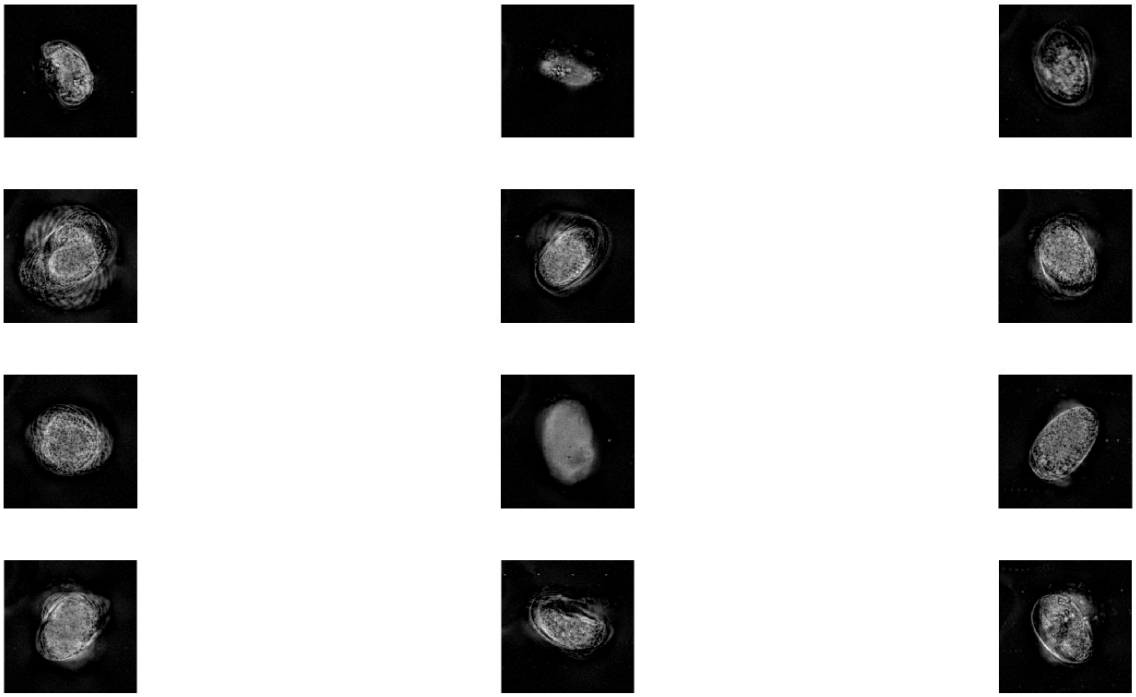

Figure 5-15, Image fusion results on rotating nematode eggs.

5.3.5.4 Alternative to wavelet fusion for rotating objects

The rotation of the objects as they were being imaged often resulted in distorted image fusions from which very little shape information could be extracted. In an attempt to mitigate this problem two approaches were taken: The images were realigned to improve the performance of the fusion algorithm, the best image from the set of each egg was selected to represent the object.

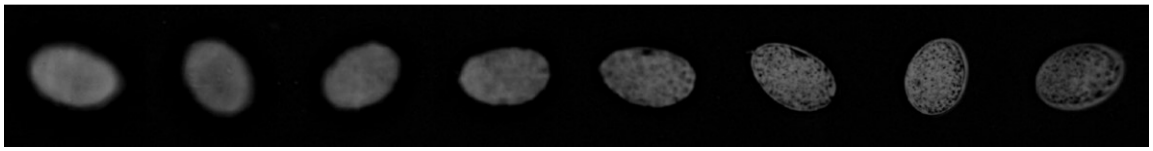

Figure 5-16, Nematode egg rotating on focal plane.

5.3.5.4.1 Rotation correction

As discussed in Chapter 3, objects moving through the channel will rotate. This will be evident in the rotation of the object both through and on the focal plane (shown in Figures 5-19 and 5-20).

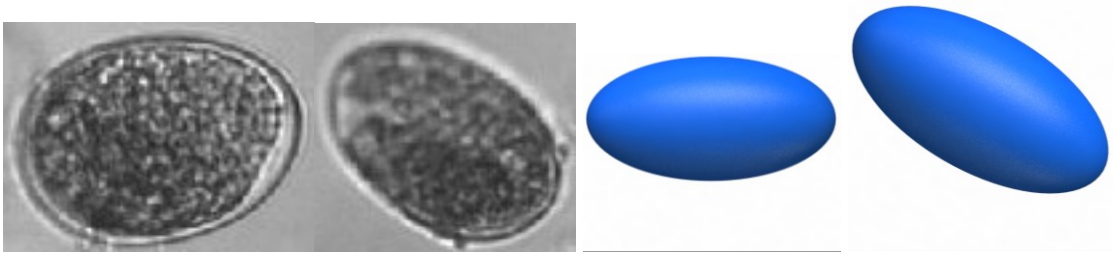

Figure 5-17, Egg rotating on focal plane (Left: egg images. Right: Render of observed rotation).

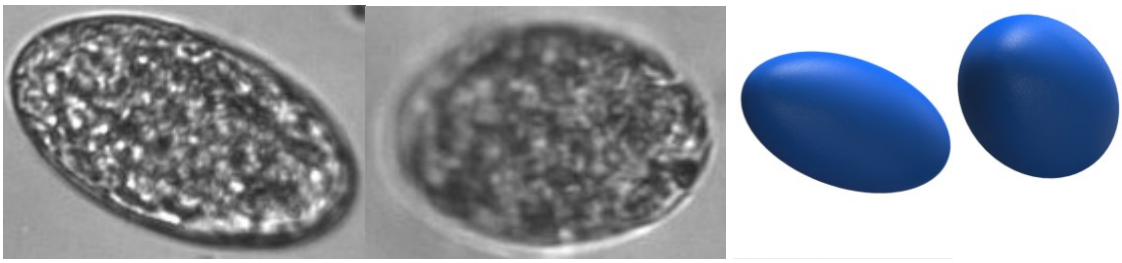

Figure 5-18, Egg rotating through the focal plane (Left: egg images. Right: Render of observed rotation).

[74] explains that fusion quality is very dependent on image alignment. To better align the images for rotation, the orientation of the egg is tracked in each frame. The orientation was defined as the angle of the major axis of the egg, relative to the X axis of the image. Each image in the stack is then rotated so that the major axes are aligned.

It should be noted that this does not correct for rotation through the focal plane. The author believes that some the rotation of an ellipse through the focal plane could be measured and possibly corrected for by examining the aspect ratio of the egg. Typically nematode eggs have a 2:1 aspect ratio. Deviation from a 2:1 ratio should indicate some rotation through the focal plane. This idea was not fully explored.

5.3.5.4.2 Finding the 'best' image

An alternative approach, similar to wavelet based fusion, is to assess an images focus based on the distribution of energy in the focal stack. The image produced from wavelet fusion can contain pixels from each image in the focal stack. The more energy in an image, the greater its representation in the fused image will be. The focused images from the stack will have a greater number of pixels in the fused image.

With this algorithm it is possible to rank images in a focal stack by the contribution they would provide to a fused image. This is analogous to an estimate of the relative focus between the images in the stack.

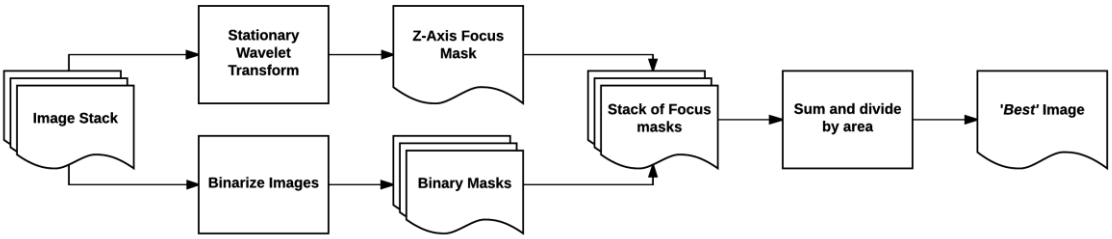

Figure 5-19, Focus assessment algorithm.

Alternatively, some shape and texture features could best be extracted from the most focused image in the stack. Rather than performing a simple image fusion where the maximum absolute pixel value at each X, Y coordinate in the focal stack was placed in the fused image, instead the Z index of the selected value was placed there. This shows from which layer in the Z stack pixels at each point originated. From this information, the number of pixels from each frame which are present in the fused image can be calculated. Figure 5-21 outlines the described process.

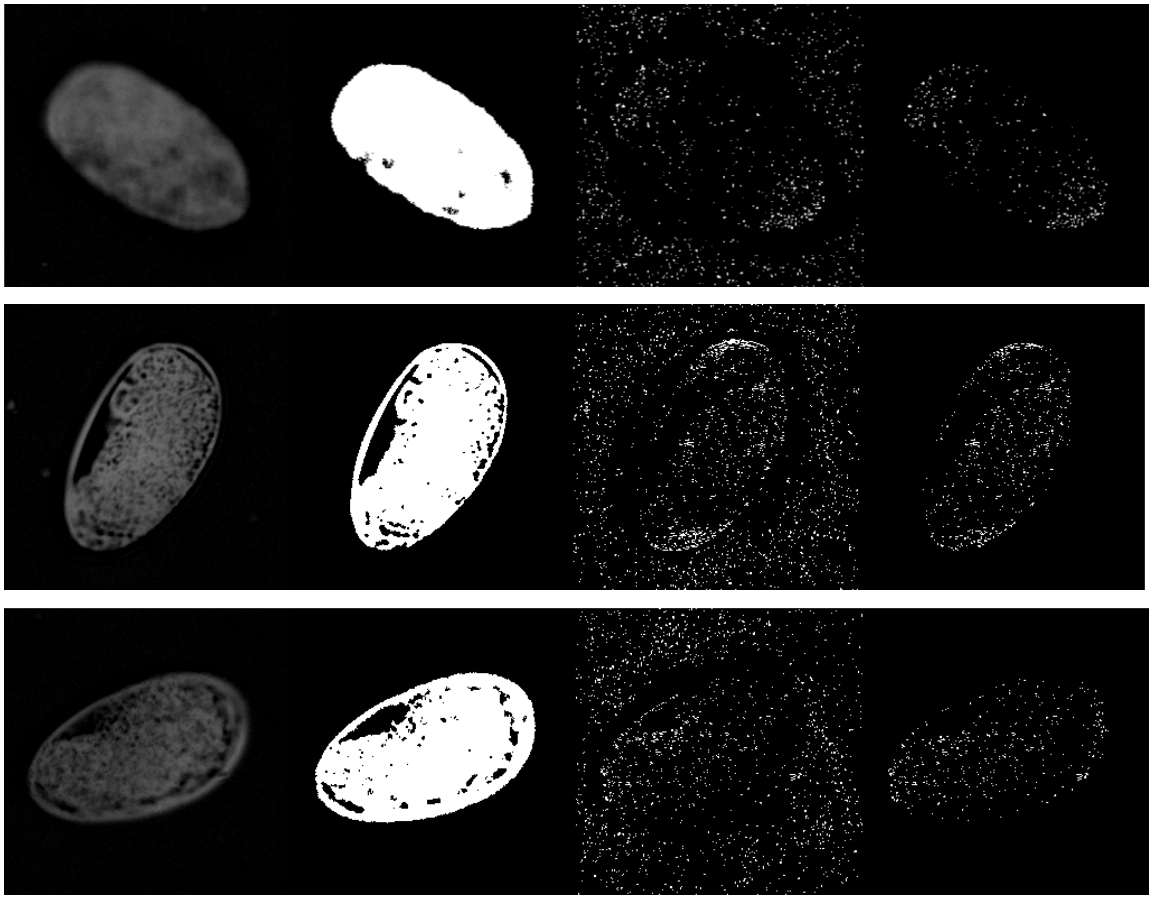

Figure 5-20, Fusion, and binary masks of eggs from focal stack(Order left to right: Image without background, Binary mask, Mask from image fusion, Binary mask multiplied by fusion mask).

It can be observed in Figure 5-22 that the background pixels will also be processed in the image fusion algorithm, and subsequently part of the mask produced from this. These pixels have no bearing on the focus of the image, and reduce the accuracy of the algorithm. A simple solution to this is to mask again with a binary image of the object. The product of the two masks can be seen in right most column of Figure 5-22. The number of pixels in the right most mask is used as an indicator for how focused the image is relative to the other images in the stack.

The number of pixels in the combined binary and wavelet masks is related to the area of the object. As an object rotates through the focal plane, its area will appear to change in the image set. Images with a higher area may contain more points in the fused image even if they are not as focused. To correct for this, a binary mask of the image is used again. The number of points present in the fused image is then divided by the area of the image (shown in Figure 5-23).

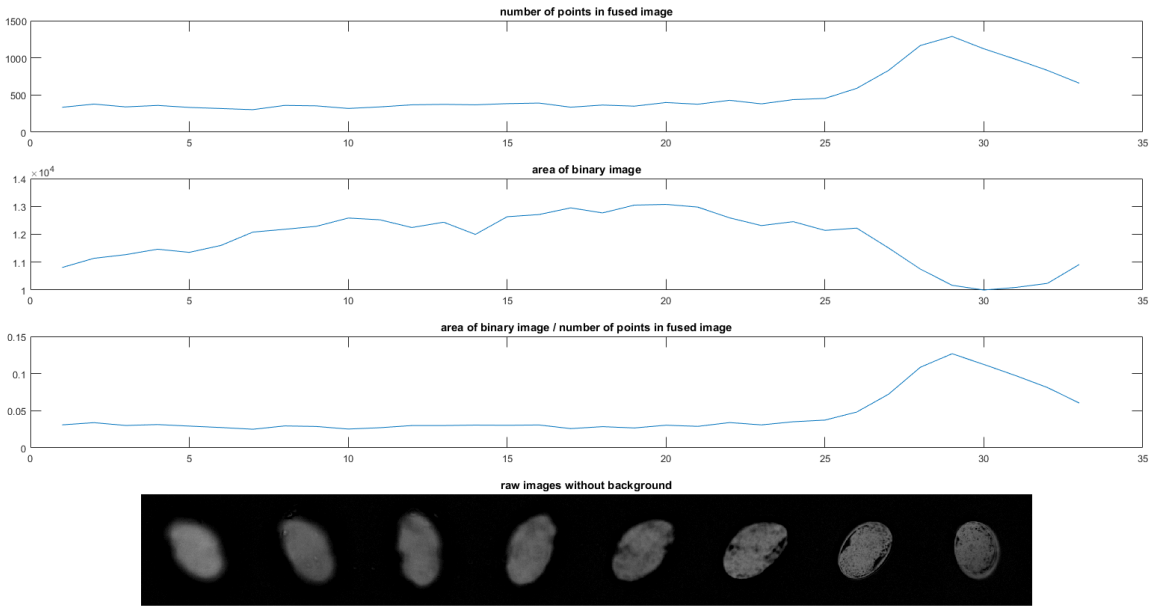

Figure 5-21, Measured Focus in Z-stack.

From dozens of test images, this simple algorithm has been demonstrated as effective in selecting the most focused image of the set. The algorithm requires little additional computation, as the wavelet transforms are already computed for image fusion.

In situations when significant rotation through the focal plane makes simple fusion perform poorly, a combination of correcting for rotation on the focal plane, and this focus estimation method is expected to produce a suitable image for contour extraction. Due to

time constraints, alternative methods to this were not considered, and extensive testing was not completed. This approach is deserving of further investigation.

5.3.5.4.3 Extreme Images

Some images with extreme values may provide more accurate measurements of the egg. For example, the image with the highest aspect ratio from the stack may provide the most accurate measurement of area. The accuracy of extreme measurements would be dependent on how defocused the image is. The author believes that combining features extracted from different images in the focal stack would present the best description of the eggs. Texture could be extracted from a fusion image, while shape and contour parameters could be extracted from the most focused, highest aspect-ratio and other extreme images. An in depth exploration of this could highlight the benefits of the extended DoF data, even when image fusion does not function as intended.

Features from extreme images could also be used to check the output of the fusion process. If shape features extracted from the fused image are not within a set margin of the features extracted from images with the highest values. Due to time constraints this idea was not developed further.

5.3.5.5 Data set cleaning

A particle cleaning method was introduced to remove particles with fewer than six objectImages. Particles less than six objectImages are typically artifacts caused by the adaptive threshold. Placing a lower bound on the adaptive threshold or replacing it with a fixed threshold could also remove them. These fixed values would need to be adjusted to the exposure time and lighting intensity.

5.4 Discussion

A mixture of real time and post processing algorithms were developed for use analysing samples of comparable size to a modified McMaster test. Data is received from the camera at 300MB/s, this is punctuated with torn, skipped, and duplicate frames. These occurrences can be reduced by reducing the data rate from the camera, and disabling CPU sleep states. The software developed runs fast enough for the given application, however if a higher data rate camera was selected, alternative methods for selecting frames to store should be investigated.

The real-time software detects objects of interest in the sample stream, and selectively stores the frames containing them. Although this system functions, it does have several limitations. For instance, when running at full speed approximately, 1% of the frames are corrupted. Also, ellipsoid objects rotating in the channel may enter an orientation with a projected area that falls below the given threshold. This results in the frame not being stored and a gap in the data set. This failing is due to the reliance on fixed thresholds, and potentially excessive down-sampling. A possible solution to this would be expanding the algorithm to consider both the previous and subsequent frame.

The post processing software makes use of image fusion to produce images suitable for feature extraction. The rotation of objects on the specimen plane can distort the fused images as the object changes orientation repeatedly between frames.

Chapter 6. Final Implementation, Results, and Discussion

The research aims presented in Chapter 1 were to develop an automated system for the presentation and imaging of nematode eggs, which was not significantly more expensive than current manual methods. The images produced must be suitable for distinguishing nematode eggs from detritus, and determination of taxa. These aims were achieved, and a system demonstrated as documented in this thesis.

6.1 Design Results

The design equations presented in Appendix II were applied to this application. These were used to determine the feasibility of the system and select hardware.

Physical constraints

- object size (typical) : 80*40um
- object size range : 80-200um
- object aspect ratio : 2:1
- sample volume : 100uL
- time frame : 10 minutes

system constraints

- channel dimensions : 200*200um
- max camera frame rate : 150 FPS
- camera dimensions : 11*4mm
- camera resolution : 2048 * 1088
- numerical aperture : 0.25
- magnification : 10x
- illumination wavelength : 528±5 nm

Fluid calculations

- volumetric flow rate : 0.167 μL/s
- average velocity : 4.167 mm/s
- reynolds number : 0.187
- pressure drop : 39.15 Pa
- max velocity : 8.33 mm/s
- shear rate : 147.49 1/s

camera calculations

- FoV : H = 1100um, V = 550um

- Tilt angle : 11˚
- Volume per frame : 0.00187 uL
- estimated frame rate : 89 FPS
- exposure time : 200 µS

6.2 Selected Hardware

Channel

- Materials : PMMA/PDMS *(see Chapter 4)*
- Connector Tubing : Tygon 0.5mm ID, 1.6mm OD

Flow control

- Pump : Elveflow AF1 millibar pressure generator
- Connection : 22 gauge needle
- Reservoir : 5ml sample tube

Optics

- Objective lens : Olympus 10x pln
- Light source : Cree X-bulb green (528nm)(Appendix V)
- Camera : UI-3360CP-M-GL Rev.2

Interface

- Desktop computer : HP Z220

6.3 Sample Preparation and Filtering

Blockages in the microchannel can cause machine failures and permanent damage to the microchannel. Numerous small objects can also cause the object detection to fail, leading to increased file sizes. To avoid these issues, a filtering method was implemented to pre-screen large and undesirable objects from the sample.

Filtering method:

1. 10g faeces weighed out.
2. Faeces mixed with 50ml of zinc sulphate solution (33% w/w concentration).
3. Strained in 0.3mm pore size sieve. (remove large solids).
4. Centrifuged at 1200RPM in 50mL falcon tube, five minutes.
5. Filtered through 205µm pore filter (run off kept).
6. Filtered through 20um pore filter (run off discarded).

Normally implementing the described filtering prevented blockages from occurring, and removed most fine particles from the solution. This was not the case with barn animals fed on pellets. The additional fibre in the faeces would clump after filtration.

6.4 Feature selection

Literature has shown both shape and texture features can be used to identify and classify nematode eggs. [4, 6] achieved high classification accuracy using shape features including deviation from an ellipse, area, and image moments. [5] then expanded to texture features, such as Grey level co-occurrence (GLCM) [19] improving the rate of correct classification. Other papers also cite the use of GLCM for nematode egg classification [7].

The following feature set was selected for detection and determination of egg taxa:

Texture:

- GLCM
  - Contrast
  - Correlation
  - Energy
  - Homogeneity

Shape:

- Aspect ratio
- Eccentricity
- Area
- Convex Area
- Perimeter
- Major axis length
- Minor axis length
- Solidity

Contour:

- Fourier transform energy distribution
- Standard deviation
- Highest radius over lowest
- Mean radius

6.5 Results

6.5.1 System Performance

This section will report on the performance of each of the subsystems.

6.5.1.1 Microchannel

The microchannels developed for this project and the fabrication techniques were very successful. Finally, these devices can be produced using commonly available equipment at an affordable cost (estimated $10 per unit).

The final design is simple to fabricate, and introduces minimal optical aberrations while achieving the necessary tilt to collect focal stacks. The materials chosen for the design match optically with an inexpensive aqueous glycerol solution, which acts as a carrier fluid for the eggs. This solution has the added advantage of not damaging eggs. Prolonged exposure to the salt solutions used in most flotation methods damages eggs. The glycerol used in the carrier fluid does not add significant costs to the process, and has a density suitable for egg flotation.

Any inconsistencies in the channel finish are attributed to either the wire surface finish, or damage which occurred when the mold wire was removed. The effects of the surface damage can be mitigated easily in software through simple background subtraction.

After prolonged use the devices degraded. The seals would eventually fail, causing fluid to flow between and outside the channels. It should be noted that this occurred after several months of use per device.

6.5.1.2 Sample preparation

The sample preparation method, uses a combination of steps from both the McMaster and FLOTAC methods. The addition of a centrifuge step was necessary to prevent damage to the initial channels. Experimentation with different filtration techniques was not continued once samples which did not damage the channels could be produced. The purpose of this filtration method was to separate the eggs from particles which could block or damage the channels. Further refinement of the process could offer reductions in filtration, and sample preparation time.

6.5.1.3 Imaging

A representative subset of the features used in literature for the classification of nematode eggs were extracted from the images collected by the system. The same features were extracted from a set of egg images collected on a microscope slide with the same imaging system. A comparison of the histograms of the extracted features (shown in Appendix VI) shows that there are only a few significant differences in range and scale between the data sets. This supports the conclusion that the introduction of the tilted microchannel does not significantly impact image quality. The optical aberrations introduced from the tilt have been significantly corrected for by the refractive index match between the carrier fluid and PDMS channel.

For some features, there are significant differences between the features extracted from the microchannel. An example of this is the energy distribution of the Fourier transform of the external contour.

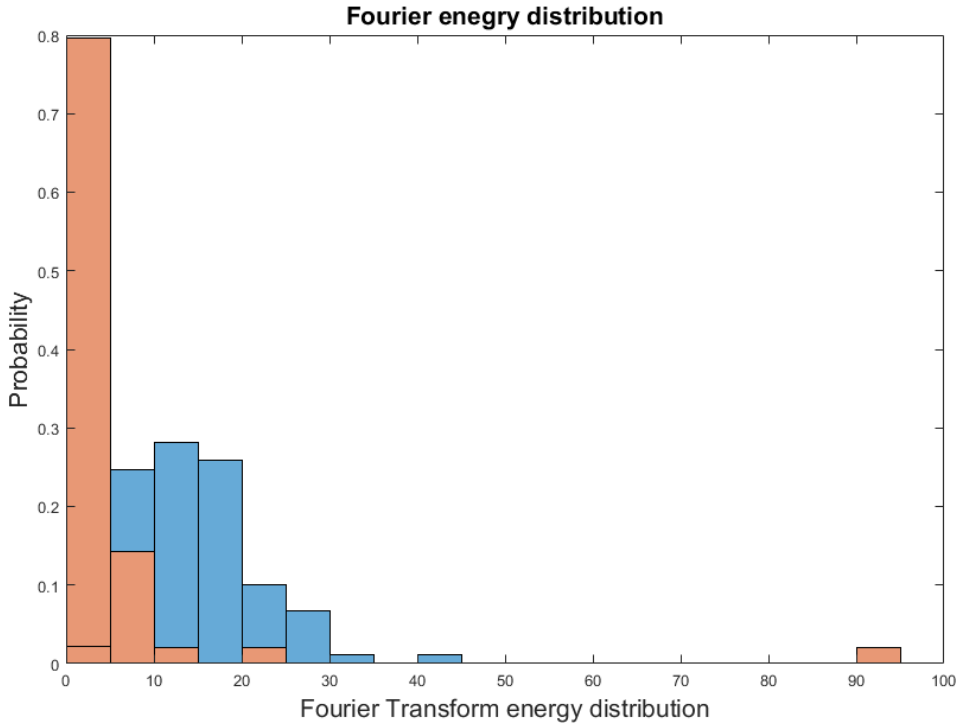

Figure 6-1, Fourier transform of external contour histogram, (Orange microscope slide, Blue: flow cell).

The majority of measured features from the microscope slides fell into a far smaller range than those from the flow cell (evident in Figure 6-1). The author expects that this is due to a difference in how the background is subtracted, and a subsequently more consistent external contour.

A sample of the images collected from the system can be found in Appendix VI. These show the level of detail obtained through this means of imaging.

6.5.1.4 Microchannel

The materials for fabricating a microchannel suitable for this application are accessible and low cost. Both PDMS and PMMA can be obtained and worked with, without any specialised equipment. Because of this, the microchannels can be built at a cost for which where they are effectively disposable. A single device can be fabricated with multiple channels for almost no additional cost, this furthers the case for a disposability.

The microchannel can be thought of as an alternative counting chamber, introduced for the purpose of simplifying automated object presentation. To this end, it was designed to be used with conventional microscopes in the same manner as a traditional counting chamber. Any microscope with a digital camera attachment could be used with this system. Interfacing with existing systems will reduce costs further, as less additional components are needed.

6.5.1.5 Imaging system components

The imaging system was comprised of a 10X magnification objective, a digital camera, and a monochromatic LED light source. The largest cost in the imaging system is the digital camera. This cost is unavoidable as the systems speed and performance is dependent on the characteristics of the camera (sensor size, and frame rate).

6.5.1.6 Integration with existing equipment

Laboratories capable of producing manual FECs will have microscopes and are likely to have computers. The capital cost of this system, could be substantially reduced by interfacing a microchannel and digital camera with the equipment already present in the laboratory. No additional optical components or computers would need to be purchased.

If flow was driven by a gravity feed instead of a pressure generator pump, costs could be further reduced.

6.5.2 Limitations

6.5.2.1 Impact of rotating objects on image fusion

The rotation of the eggs as they move through the channel had a negative effect on the performance of the image fusion algorithm. To compensate for this, an attempt was made to align the images in a stack based on the angle of their major axes. This helped correct for rotation on the specimen plane, however rotation through the specimen still caused alignment issues. Another work around was to subtly alter the fusion algorithm to assess the relative focus between the images in focal stacks. This worked effectively and consistently selected appropriate images for feature extraction.

In a future system a combination of both methods and additional estimation of object orientation could be used to more effectively fuse the data from the focal stack.

6.5.2.2 Channel blockages from high fibre content in samples from barn fed animals

Despite numerous attempts, some faecal samples caused blockage during and after filtration. This is due to the high fibre content of the faeces (typical of barn fed animals). Fibre could not be easily separated from the eggs using centrifuging, or sieving. Large fibre particles would form after filtration as smaller particles clumped together. Not only did this lead to blockages in the channel, it also made the real-time image analysis perform poorly.

6.5.2.3 Microchannel degradation and failures

After prolonged use over a period of months, the seals in the microchannels failed. This resulted in leakage between the channels, with less direct fluid flow through the channel. Bubbles would enter the flow stream and cause objects to move inconsistently. In some circumstance, once a single channel failed, it often resulted in the failure of the entire device.

In some cases, material became lodged in the channel. An appropriate method for removal could not be devised rendering the device useless. This highlights a significant downside to this approach. For a traditional FEC method the size of the detritus in the sample will not significantly impact the test. However, for the digital imaging system presented here, the counting chamber (microchannel) can be damaged by large objects.

6.6 Conclusion

This thesis presents the initial concept development and proof of concept work for a low-cost microfluidics-based method for the automated, detection, counting, and classification of nematode eggs. The presented system demonstrates a case for the use of a tilted microchannel as a simple object presentation system for the purpose of collecting extended depth-of-field images of nematode eggs. Much of the initial development of the machine was completed using pine pollen as a substitute for nematode eggs. This work indicated that the system may also have applications in automated palynological classification.

A simple, low cost method for producing microchannels of the required geometry, and quality was developed. Several different materials and fabrication techniques were trialled and eliminated in this development.

A suite of software was developed for image acquisition and analysis. This software is separated into two sections, real-time object detection and, post processing. The real-time software accurately detected frames of interest and stored them while ignoring frames unlikely to contain egg objects. This aided significantly by reducing the volume of data stored from each sample. Although not entirely sufficient as an egg counter as no assessment of egg viability is made, this part of the software does provide the foundation for a simple automated nematode counter. The system was shown to consistently capture images of eggs in the flow steam with a low and acceptable number of missed eggs. Few frames not containing eggs were captured. However, such frames did not invalidate counts.

The post processing software grouped and localised the sets of images captured for each egg. Then performed the following operations:

- Specimen plane rotation correction
- Image fusion
- Best image assessment
- Feature extraction

With further development, this system could lead to a useful tool for automatic detection, counting, and classification of nematode eggs. Areas for further development include:

- Refinement and automation of the sample preparation process (filtration), to further reduce operator involvement and streamline the system.
- Replacing the pressure generator pump with a gravity feed, further reducing cost and complexity.
- The development of a tailored feature set for the classification of eggs, based on the species of nematodes common in New Zealands ovine and bovine herds.

References

References are as generated by Google Scholar, some inconsistencies may be found.

[1] R. V. Brunsdon, "The Economic Importance of Parasites of Livestock in New Zealand," *New Zealand Society for Parasitology,* vol. 15, 1988.

[2] Waghorn T.S., Leathwick D.M., Rhodes A.P., Jackson R., Pomroy W.E., West D.M.*, et al.*, "Prevalence of anthelmintic resistance on 62 beef cattle farms in the North Island of New Zealand.," *New Zealand Veterinary Journal,* vol. 54, pp. 278-282, 2006.

[3] Waghorn T.S., Leathwick D.M., Rhodes A.P., Lawrence K.E., Jackson R., Pomroy W.E.*, et al.*, "Prevalence of anthelmintic resistance on sheep farms in New Zealand.," *New Zealand Veterinary Journal,* vol. 54, pp. 271-277, 2006.

[4] C. Sommer, "Digital image analysis and identification of eggs from bovine parasitic nematodes," *Journal of helminthology,* vol. 70, pp. 143-151, 1996.

[5] C. Sommer, "Quantitative characterization of texture used for identification of eggs of bovine parasitic nematodes," *Journal of helminthology,* vol. 72, pp. 179-182, 1998.

[6] E. Dogantekin, M. Yilmaz, A. Dogantekin, E. Avci, and A. Sengur, "A robust technique based on invariant moments–ANFIS for recognition of human parasite eggs in microscopic images," *Expert Systems with Applications,* vol. 35, pp. 728-738, 2008.

[7] G. Sengül, "Classification of parasite egg cells using gray level cooccurence matrix and kNN," *Biomedical Research,* vol. 27, 2016.

[8] W. E. Pomroy, "227.303 Veterinary Parasitic Diseases," in *Self-teaching Manual for Nematoda*, I. Scott, Ed., ed, 2014, p. 198.

[9] vetslides, "McMaster counting slides, green grid," mcmaster-counting-slides-green-grid.jpg, Ed., ed. http://vetslides.com/wp-content/uploads/2013/02/mcmaster-counting-slides-green-grid.jpg, 2013.

[10] A. Bosco, L. Rinaldi, M. P. Maurelli, V. Musella, G. C. Coles, and G. Cringoli, "The comparison of FLOTAC, FECPAK and McMaster techniques for nematode egg counts in cattle," *Acta Parasitologica,* vol. 59, pp. 625-628, 2014.

[11] parassitologia, "FLOTAC banner," flotac-banner.jpg, Ed., ed. http://www.parassitologia.unina.it/wp-content/uploads/2015/07/flotac-banner.jpg, 2015.

[12] DOLF, "FLOTAC Steps," FLOTAC-steps.jpg, Ed., ed. http://www.dolf.wustl.edu/wp-content/uploads/FLOTAC-Steps.jpg.

[13] techiongroup, "FECPAK Complete Unit," fecpak-complete-unit_500x380.jpg, Ed., ed.

[14] B. Speich, S. Knopp, K. A. Mohammed, I. S. Khamis, L. Rinaldi, G. Cringoli*, et al.*, "Comparative cost assessment of the Kato-Katz and FLOTAC techniques for soil-transmitted helminth diagnosis in epidemiological surveys," *Parasites & vectors,* vol. 3, p. 71, 2010.

[15] A. Kongs, G. Marks, P. Verle, and P. Van Der Stuyft, "The unreliability of the Kato-Katz technique limits its usefulness for evaluating S. mansoni infections," *Tropical Medicine & International Health,* vol. 6, pp. 163-169, 2001.

[16] Y. S. Yang, D. K. Park, H. C. Kim, M.-H. Choi, and J.-Y. Chai, "Automatic identification of human helminth eggs on microscopic fecal specimens using digital image processing and an artificial neural network," *IEEE Transactions on Biomedical Engineering,* vol. 48, pp. 718-730, 2001.

[17] J. M. Bruun, J. M. Carstensen, N. Vejzagić, S. Christensen, A. Roepstorff, and C. M. Kapel, "OvaSpec–A vision-based instrument for assessing concentration and developmental stage of Trichuris suis parasite egg suspensions," *Computers in biology and medicine,* vol. 53, pp. 94-104, 2014.

[18] P. Slusarewicz, S. Pagano, C. Mills, G. Popa, K. M. Chow, M. Mendenhall*, et al.*, "Automated parasite faecal egg counting using fluorescence labelling, smartphone image capture and computational image analysis," *International journal for parasitology,* vol. 46, pp. 485-493, 2016.

[19] D. A. Clausi, "An analysis of co-occurrence texture statistics as a function of grey level quantization," *Canadian Journal of remote sensing,* vol. 28, pp. 45-62, 2002.

[20] L. E. Ostergaard, "Automatic Detection and Characterization of Parasite Eggs by Image Processing," Virginia Tech, 2013.

[21] R. Hadi, K. Ghazali, I. Z. Khalidin, and M. Zeehaida, "Human parasitic worm detection using image processing technique," in *Computer Applications and Industrial Electronics (ISCAIE), 2012 IEEE Symposium on*, 2012, pp. 196-201.

[22] D. Avci and A. Varol, "An expert diagnosis system for classification of human parasite eggs based on multi-class SVM," *Expert Systems with Applications,* vol. 36, pp. 43-48, 2009.

[23] E. R. Dowski Jr and G. E. Johnson, "Wavefront coding: a modern method of achieving high-performance and/or low-cost imaging systems," in *SPIE's International Symposium on Optical Science, Engineering, and Instrumentation*, 1999, pp. 137-145.

[24] M. Matrecano, M. Paturzo, A. Finizio, and P. Ferraro, "Enhancing depth of focus in tilted microfluidics channels by digital holography," *Optics letters,* vol. 38, pp. 896-898, 2013.

[25] V. R V, K. Kim, A. S. Somkuwar, Y. Park, and R. K. Singh, "Single-shot optical imaging through scattering medium using digital in-line holography," *arXiv preprint arXiv:1603.07430,* 2016.

[26] K. Holt, G. Allen, R. Hodgson, S. Marsland, and J. Flenley, "Progress towards an automated trainable pollen location and classifier system for use in the palynology laboratory," *Review of Palaeobotany and Palynology,* vol. 167, pp. 175-183, 2011.

[27] Y. Fan and A. P. Bradley, "A two-stage method to correct aberrations induced by slide slant in bright-field microscopy," *Micron,* vol. 87, pp. 18-32, 2016.

[28] J. Braat, "Analytical expressions for the wave-front aberration coefficients of a tilted plane-parallel plate," *Applied optics,* vol. 36, pp. 8459-8467, 1997.

[29] J. Wang and R. Koning, "Influence of slant of objective on image formation in optical microscopes," *Chinese Optics Letters,* vol. 6, pp. 603-606, 2008.

[30] N. C. Pégard and J. W. Fleischer, "Three-dimensional deconvolution microfluidic microscopy using a tilted channel," *Journal of biomedical optics,* vol. 18, pp. 040503-040503, 2013.

[31] W. E. Ortyn, D. J. Perry, V. Venkatachalam, L. Liang, B. E. Hall, K. Frost*, et al.*, "Extended depth of field imaging for high speed cell analysis," *Cytometry Part A,* vol. 71, pp. 215-231, 2007.

[32] V. K. Jagannadh, M. D. Mackenzie, P. Pal, A. K. Kar, and S. S. Gorthi, "Slanted channel microfluidic chip for 3D fluorescence imaging of cells in flow," *Optics Express,* vol. 24, pp. 22144-22158, 2016.
[33] J. W. Fleischer, "Fluid channels for computational imaging in optofluidic microscopes," ed: Google Patents, 2014.
[34] S. Liu and H. Hua, "Extended depth-of-field microscopic imaging with a variable focus microscope objective," *Optics express,* vol. 19, pp. 353-362, 2011.
[35] S. Kuiper and B. Hendriks, "Variable-focus liquid lens for miniature cameras," *Applied physics letters,* vol. 85, pp. 1128-1130, 2004.
[36] G. Tylka, T. Niblack, T. Walk, K. Harkins, L. Barnett, and N. Baker, "Flow cytometric analysis and sorting of Heterodera glycines eggs," *Journal of nematology,* vol. 25, p. 596, 1993.
[37] S. Umair, L. McMurtry, J. Knight, and H. Simpson, "Use of fluorescent lectin binding to distinguish eggs of gastrointestinal nematode parasites of sheep," *Veterinary parasitology,* vol. 217, pp. 76-80, 2016.
[38] V. K. Jagannadh, R. S. Murthy, R. Srinivasan, and S. S. Gorthi, "Field-Portable Microfluidics-Based Imaging Flow Cytometer," *Journal of Lightwave Technology,* vol. 33, pp. 3469-3474, 2015.
[39] daigger, "Axygen PCR Tubes 0.2 mL," 16557-Group_1-B.jpg, Ed., ed. http://www.daigger.com, 2017.
[40] I. new Era Pump Systems, "NE-1010 Programmable Single Syringe Pump," ed, 2017.
[41] Elveflow, "Af1 microfluidic pressure pump," Af1-microfluidic-pressure-pump-.png, Ed., ed. www.elveflow.com: elveflow, 2016.
[42] I. I. D. Systems, "UI-3060CP Rev. 2," ids-usb3-ueye-cp-rev2-industrial-machine-vision-camera-1.jpg, Ed., ed. https://en.ids-imaging.com, 2016.
[43] K. H. Ghazali, R. S. Hadi, and Z. Mohamed, "Automated system for diagnosis intestinal parasites by computerized image analysis," *Modern Applied Science,* vol. 7, p. 98, 2013.
[44] G. P. Association, *Physical properties of glycerine and its solutions*: Glycerine Producers' Association, 1963.
[45] *ViscosityShearFlow*. Available: http://www.flowillustrator.com/wp-content/uploads/2015/02/ViscosityShearFlow.png
[46] *Poiseuille Flow*. Available: https://www.intechopen.com/source/html/43434/media/image1.jpeg
[47] G. B. Jeffery, "The motion of ellipsoidal particles immersed in a viscous fluid," in *Proceedings of the Royal Society of London A: Mathematical, Physical and Engineering Sciences*, 1922, pp. 161-179.
[48] I. Zia, R. Cox, and S. Mason, "Ordered aggregates of particles in shear flow," in *Proceedings of the Royal Society of London A: Mathematical, Physical and Engineering Sciences*, 1967, pp. 421-441.
[49] M. Ingber and L. Mondy, "A numerical study of three-dimensional Jeffery orbits in shear flow," *Journal of Rheology,* vol. 38, pp. 1829-1843, 1994.
[50] Z. Wu, Z. Xu, O. Kim, and M. Alber, "Three-dimensional multi-scale model of deformable platelets adhesion to vessel wall in blood flow," *Philosophical Transactions of the Royal Society of London A: Mathematical, Physical and Engineering Sciences,* vol. 372, p. 20130380, 2014.
[51] M. W. Davidson, "Microscopy basics, numerical aperture," 2016.
[52] T. U. o. Utah. (2011). *Super-Resolution Microscopy Tutorial*. Available: http://advanced-microscopy.utah.edu/education/super-res/

[53] (2016). *Optical Aberration*. Available: https://en.wikipedia.org/wiki/Optical_aberration
[54] E. Optics, "Comparison of Optical Aberrations," 2016.
[55] "Camera Lens Corrections - Chromatic Aberrations," in *1001 Best Photography Tips*, ed, 2013.
[56] Thorlabs. (2016). *Beam Displacement Optics*. Available: https://www.thorlabs.com/newgrouppage9.cfm?objectgroup_id=5952
[57] J. A. Shimizu and P. J. Janssen, "Compensation plate for tilted plate optical aberrations," ed: Google Patents, 1996.
[58] P. Scholz, I. Reuter, and D. Heitmann, "PIV measurements of the flow through an intake port using refractive index matching," in *16th International Symposium on Applications of Laser Techniques to Fluid Mechanics*, 2012.
[59] T.-F. Hong, W.-J. Ju, M.-C. Wu, C.-H. Tai, C.-H. Tsai, and L.-M. Fu, "Rapid prototyping of PMMA microfluidic chips utilizing a CO 2 laser," *Microfluidics and nanofluidics,* vol. 9, pp. 1125-1133, 2010.
[60] J. R. Anderson, D. T. Chiu, H. Wu, O. Schueller, and G. M. Whitesides, "Fabrication of microfluidic systems in poly (dimethylsiloxane)," *Electrophoresis,* vol. 21, pp. 27-40, 2000.
[61] Y. Jia, J. Jiang, X. Ma, Y. Li, H. Huang, K. Cai*, et al.*, "PDMS microchannel fabrication technique based on microwire-molding," *Chinese Science Bulletin,* vol. 53, pp. 3928-3936, 2008.
[62] Elveflow, "INTRODUCTION ABOUT PDMS SOFT-LITHOGRAPHY AND POLYMER MOLDING FOR MICROFLUIDICS," http://www.elveflow.com/wp-content/uploads/2013/05/Micromolding-in-capillaries.png, Ed., ed. www.elveflow.com: elveflow, 2016.
[63] F. Hendriks and A. Aviram, "Use of zinc iodide solutions in flow research," *Review of Scientific Instruments,* vol. 53, pp. 75-78, 1982.
[64] R. Budwig, "Refractive index matching methods for liquid flow investigations," *Experiments in fluids,* vol. 17, pp. 350-355, 1994.
[65] M. Jermy, "Making it clear: flexible, transparent laboratory flow models for soft and hard problems," in *8th World Conference on Experimental Heat Transfer, Fluid Mechanics, and Thermodynamics*, 2013.
[66] D. V. Vezenov, B. T. Mayers, D. B. Wolfe, and G. M. Whitesides, "Integrated fluorescent light source for optofluidic applications," *Applied Physics Letters,* vol. 86, p. 041104, 2005.
[67] P. M. Bardet, C. D. Fu, C. E. Sickel, and N. A. Weichselbaum, "Refractive index and solubility control of para-cymene solutions," in *2014 International Symposium on Applications of Laser Techniques to Fluid Mechanics, Instituto Superior Tecnico, Lisbon, Portugal*, 2014.
[68] D. Wang. (2013). *Why migrate to DDR4?*
[69] Samsung. (2016). *Samsung SSD 850 EVO Data Sheet, Rev.3.1 (May, 2016)*.
[70] G. Bradski, "The opencv library," *Doctor Dobbs Journal,* vol. 25, pp. 120-126, 2000.
[71] T. Report, "GPU sales strong as AMD gains market share," ed, https://techreport.com/news/15778/gpu-sales-strong-as-amd-gains-market-share 2008.
[72] J. Franco, G. Bernabé, J. Fernández, and M. Ujaldón, "The 2D wavelet transform on emerging architectures: GPUs and multicores," *Journal of Real-Time Image Processing,* vol. 7, pp. 145-152, 2012.

[73] Y. Lu, I. Cohen, X. S. Zhou, and Q. Tian, "Feature selection using principal feature analysis," in *Proceedings of the 15th ACM international conference on Multimedia*, 2007, pp. 301-304.

[74] G. Pajares and J. M. De La Cruz, "A wavelet-based image fusion tutorial," *Pattern recognition,* vol. 37, pp. 1855-1872, 2004.

Appendices

Appendix I Data Sheets

UI-3360CP-M-GL Rev.2



Specification

Sensor

Sensor type	CMOS Mono
Shutter	Global Shutter
Sensor characteristic	Linear with knee points
Readout mode	Progressive scan
Pixel Class	2 MP
Resolution	2.23 Mpix
Resolution (h x v)	2048 x 1088 Pixel
Aspect ratio	17:9
ADC	12 bit
Color depth (camera)	12 bit
Optical sensor class	2/3"
Optical Size	11.264 mm x 5.984 mm
Optical sensor diagonal	12.75 mm (1/1.25")
Pixel size	5.5 µm
Manufacturer	CMOSIS
Sensor Model	CMV2000-3E5M
Gain (master/RGB)	4x/-
AOI horizontal	same frame rate
AOI vertical	increased frame rate
AOI image witdh / step width	16 / 4
AOI image height / step width	2 / 2
AOI position grid (horizontal/vertical)	2 / 2
Binning horizontal	-
Binning vertical	-
Binning method	-
Binning factor	-
Subsampling horizontal	same frame rate
Subsampling vertical	same frame rate
Subsampling method	M/C automatic
Subsampling factor	2, 4, 6, 8

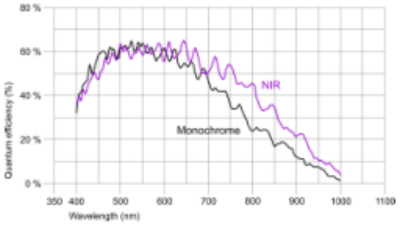

Subject to technical modifications (2017-06-27)

IDS Imaging Development Systems GmbH
Dimbacher Str. 6 - 8 · 74182 Obersulm · Germany · Phone +49 7134 96196-0 · Fax +49 7134 96196-99 · E-mail info@ids-imaging.com

UI-3360CP-M-GL Rev.2

Model

Pixel clock range	38 MHz - 344 MHz
Frame rate freerun mode	152.0 fps
Frame rate trigger (maximum)	152.0 fps
Exposure time (minimum - maximum)	0.025 ms - 500 ms
Power consumption	1.4 W - 2.9 W
Image memory	128 MB
Special features	Overlap trigger, Dual exposure, Sensor source gain, Multi-AOI

Ambient conditions

The temperature values given below refer to the outer device temperature of the camera housing.

Device temperature during operation	0 °C - 55 °C / 32 °F - 131 °F
Device temperature during storage	-20 °C - 60 °C / -4 °F - 140 °F
Humidity (relative, non-condensing)	20 % - 80 %

Connectors

Interface connector	USB 3.0 micro-B, screwable
I/O connector	8-pin Hirose connector (HR25-7TR-8PA(73))
Power supply	USB cable

Pin assignment I/O connector

1	Ground (GND)
2	Flash output with optocoupler (-)
3	General Purpose I/O (GPIO) 1
4	Trigger input with optocoupler (-)
5	Flash output with optocoupler (+)
6	General Purpose I/O (GPIO) 2
7	Trigger input with optocoupler (+)
8	Output supply voltage, 5 V (100 mA)

Design

Lens Mount	C-Mount
IP code	IP30
Dimensions H/W/L	29.0 mm x 29.0 mm x 29.0 mm
Mass	52 g

IDS Imaging Development Systems GmbH
Dimbacher Str. 6 - 8 · 74182 Obersulm · Germany · Phone +49 7134 96196-0 · Fax +49 7134 96196-99 · E-mail info@ids-imaging.com

ELVEFLOW
PLUG & PLAY MICROFLUIDICS

AF1
Pressure Generator

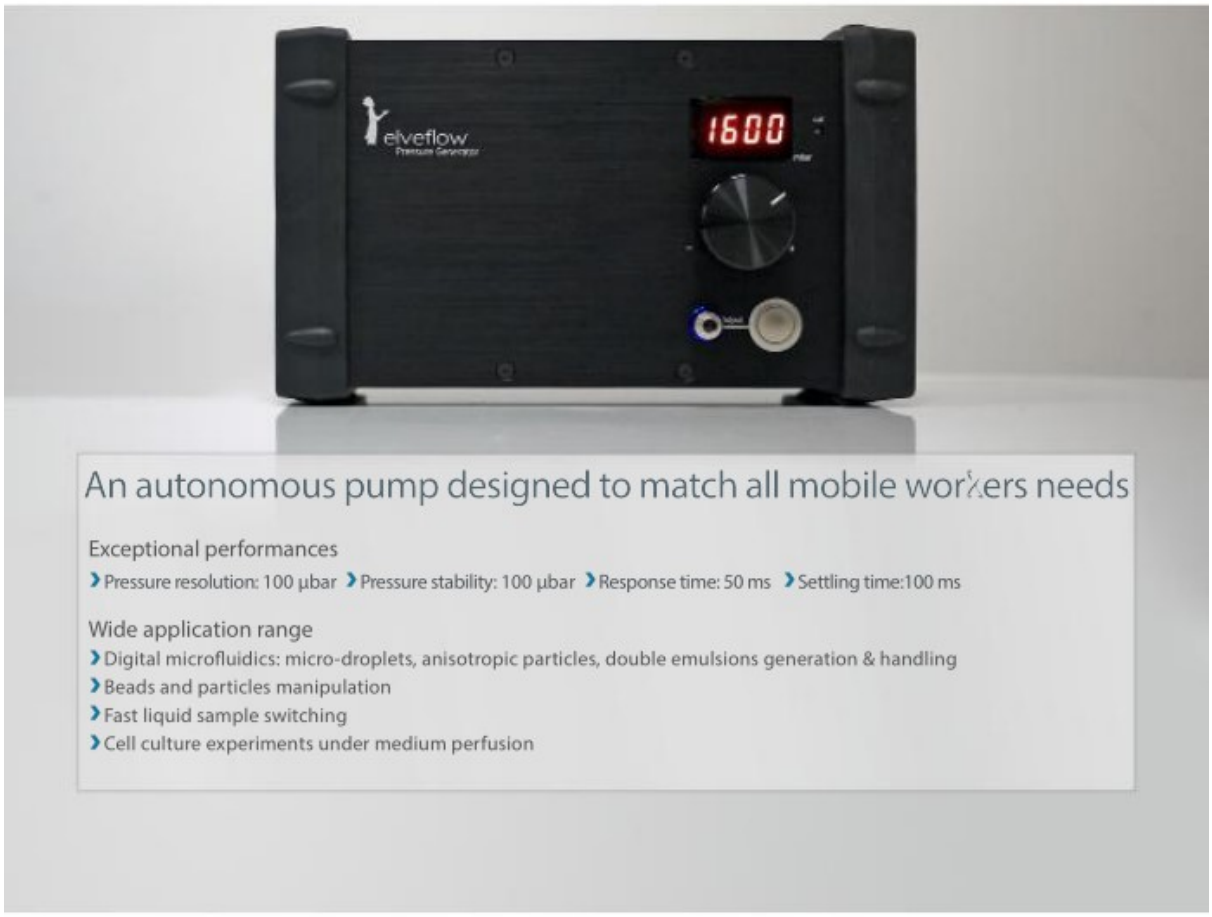

AF1
TECHNICAL SPECIFICATIONS

AF1 Unit Pressure range Premium	0 to 200 mbar (0 to 2.9 psi)	0 to 1600mbar (0 to 23 psi)	Dual Pressure & Vacuum Controller -700 to 1000 mbar (-10 to 14 psi)
Type of pressure	Positive	Positive	Negative & Positive
Pressure Sensor Resolution	0.006 % FS 12.2 µbar - 0.00017 psi	0.006 % FS 122 µbar - 0.0017 psi	0.006 % FS 122 µbar - 0.0017 psi
Pressure stability	100 µbar (0.0014 psi) i.e. 0.05 % Full Scale	1 mbar (0.014 psi) i.e. 0.05 % Full Scale	-700 to 500 mBar : 1 mBar 500 to 1000 mBar: 5 mBar
Response time	50 ms		
Settling time	down to 40 ms [1]		
Supply pressure (min - max)	Integrated pump No pressure source needed		Pressuresupplyneeded (1.5barmin,2.5barmax)
Liquid compatibility	Any aqueous or organic solvent, oil, or biological sample solution can be propelled		
Power consumption	15 W (100 V to 240 V - 50 Hz to 60 Hz)		
Weight	1.7 kg		
Case dimensions L x l x h (mm)	220 x 130 x 130		
Output connectors	Stainless steel female luer lock		

(1) Volume dependent – Measurement done on 12 mL reservoir for a set point from 0 to 200 mbar

AF1
PRODUCTS & SERVICES

Elements provided by Elveflow	Included	Optional
Software & libraries Control all Elveflow® instruments with the same smart interface.	•	
AF1 Connection kit A complete set of accessories fitted for the AF1 pressure generator.		•
Kits Connect any pressure source/syringe pump to your device.		•
Reservoirs Gas tight reservoirs with ergonomic fluidic connection.		•
Flow Sensors A line of sensors to monitor very low liquid flow rates.		•
Compressor A safe & secure pressure source for the OB1 pressure controller.		•

Related Products & Services

›Eppendorf® Microfluidic Tank

100% gas tight connection caps.
1.5 - 2 mL Eppendorf® tubes
15 mL BD Falcon® tubes
100 mL - 2 L Upchurch® bottle caps.

›Connection Kits

Bored of microplumbing issues? Our kits enable to easily connect your microfluidic device to any pressure or flow control equipment.

› Broad Product Line

Elveflow instruments are designed to work together on your microfluidic setup. Switch valve system, flow rate monitoring, temperature control...

›Service

Benefit from our microfluidics PhD team's expertise. Take advantage of our support for specific developments on your setup.

›Grants & Partnerships

Elveflow invests in co-development and cooperative projects with academic, SME and industrial partners to take an active part in the development of microfluidics.

It is no coincidence that the most prestigious names trust in us

Product Information
Electronics

DOW CORNING

Sylgard® 184 Silicone Elastomer

FEATURES & BENEFITS

- Flowable
- Room temperature and heat cure
- Good dielectric properties
- Rapid, versatile cure processing controlled by temperature
- High transparency allows easy inspection of components

COMPOSITION

- Two-part
- 10 to 1 mix ratio
- Polydimethylsiloxane elastomer

Transparent encapsulant with good flame resistance

APPLICATIONS

Sylgard® 184 Silicone Elastomer is suitable for:

- LED Lighting encapsulation
- Power supplies
- Connectors
- Sensors
- Industrial controls
- Transformers
- Amplifiers
- High voltage resistor packs
- Relays
- Adhesive/encapsulant for solar cells
- Adhesive handling beam lead integrated circuits during processing

TYPICAL PROPERTIES

Specification Writers: These values are not intended for use in preparing specifications. Please contact your local Dow Corning sales office or your Global Dow Corning Connection before writing specifications on this product.

Property	Unit	Result
One or Two Part		Two
Color		Colorless
Viscosity (Base)	cP	5100
	Pa-sec	5.1
Viscosity (Mixed)	cP	3500
	Pa-sec	3.5
Thermal Conductivity	btu/hr ft °F	0.15
	W/m °K	0.27
Specific Gravity (Cured)		1.03
Working Time at 25°C (Pot Life - hours)	hours	1.5
Cure Time at 25°C	hours	48
Heat Cure Time at 100°C	minutes	35
Heat Cure Time at 125°C	minutes	20
Heat Cure Time at 150°C	minutes	10
Durometer Shore		43
Dielectric Strength	volts/mil	500
	kV/mm	19

TYPICAL PROPERTIES (Continued)

Property	Unit	Result
Volume Resistivity	ohm*cm	2.9E+14
Dissipation Factor at 100 Hz		0.00257
Dissipation Factor at 100kHz		0.00133
Dielectric Constant at 100 Hz		2.72
Dielectric Constant at 100 kHz		2.68
Linear CTE (by DMA)	ppm/°C	340
Tensile Strength	PSI	980
	MPa	6.7
	Kg/cm^2	69
Refractive Index	@ 589 nm	1.4118
Refractive Index	@ 632.8 nm	1.4225
Refractive Index	@1321 nm	1.4028
Refractive Index	@ 1554 nm	1.3997
UL RTI Rating	°C	150

DESCRIPTION

Dow Corning® brand silicone 10 to 1 encapsulants are supplied as two-part liquid component kits. When liquid components are thoroughly mixed, the mixture cures to a flexible elastomer, which is well suited for the protection of electrical/electronic applications. *Dow Corning* silicone encapsulants cure without exotherm at a constant rate regardless of sectional thickness or degree of confinement.

Dow Corning® silicone elastomers require no post cure and can be placed in service immediately following the completion of the cure schedule. Standard silicone encapsulants require a surface treatment with a primer in addition to good cleaning for adhesion while primerless silicone encapsulants require only good cleaning.

APPLICATION METHODS

- Automated metered mixing and dispensing
- Manual mixing

MIXING AND DE-AIRING

The 10 to 1 mix ratio these products are supplied in gives one latitude to tune the modulus and hardness for specific application needs and production lines. In most cases de-airing is not required.

PREPARING SURFACES

In applications requiring adhesion, priming will be required for many of the silicone encapsulants. For best results, the primer should be applied in a very thin, uniform coating and then wiped off after application. After application, it should be thoroughly cured prior to application of the silicone elastomer. Additional instructions for primer usage can be found in the information sheets specific to the individual primers.

PROCESSING/CURING

Thoroughly mixed *Dow Corning* silicone encapsulant may be poured/dispensed directly into the container in which it is to be cured. Care should be taken to minimize air entrapment. When practical, pouring/dispensing should be done under vacuum, particularly if the component being potted or encapsulated has many small voids. If this technique cannot be used, the unit should be evacuated after the silicone encapsulant has been poured/dispensed. *Dow Corning* silicone encapsulants may be either room temperature (25°C/77°F) or heat cured. Room temperature cure encapsulants may also be heat accelerated for faster cure. Ideal cure conditions for each product are given in the product selection table.

POT LIFE AND CURE RATE

Cure reaction begins with the mixing process. Initially, cure is evidenced by a gradual increase in viscosity, followed by gelation and conversion to a solid elastomer. Pot life is defined as the time required for viscosity to double after base and curing agent are mixed and is highly temperature and application dependent. Please refer to the data table.

USEFUL TEMPERATURE RANGES

For most uses, silicone elastomers should be operational over a temperature range of -45 to 200°C (-49 to 392°F) for long periods of time. However, at both the low and high temperature ends of the spectrum, behavior of the materials and performance in particular

2014, April 2
Form No. 11-3184B-01

Appendix II Design Equations

Physical constraints:

- object size
- object size range
- object aspect ratio
- sample volume
- time frame

System constraints:

- channel dimensions
- max camera frame rate
- camera dimensions
- numerical aperture
- magnification
- illumination frequency

The design equations can be broken down into fluid mechanics related equations, and system specific equations.

Fluid calculations (equations from chapter 3):

- volumetric flow rate

$$Q = \frac{V}{T} \qquad A(1)$$

- average velocity

$$u = \frac{Q}{Y\,Z} \qquad A(2)$$

- Reynolds number

$$R_e = \frac{\rho u D_H}{\mu} \qquad A(3)$$

- pressure drop

$$\Delta P = \frac{32\mu L v}{d^2} \qquad A(4)$$

- max velocity

$$u_{max} = \frac{\Delta P R^2}{4\mu L} \qquad A(5)$$

- shear rate

$$\gamma = \frac{\Delta Pr}{2\mu L} \qquad A(6)$$

For further details on the equations expressed here, please refer to Chapter 3.

camera calculations:

- Field of View

$$H_{fov} = {}^{S_h}/_{O_m} \qquad A(7)$$

$$V_{fov} = {}^{S_w}/_{O_m} \qquad A(8)$$

From the specified objective magnification, and sensor. The field of view from the sensor can be calculated using equations A7 & A8. These can be used to assess the width of the channel, and the aspect ratio of a candidate sensor.

- Channel dimension requirements [32]

$$C_h = 2\, O_{h\,max} \qquad A(9)$$

- Tilt angle required

$$\theta = \sin\left(\frac{C_h}{H_{fov}}\right) \qquad A(10)$$

[32] suggests that to avoid blockages, the minimum channel dimension should be twice the height of the object. He also provides a useful equation for determining the required tilt angled, which has been rephrased in equations 9 & 10.

- Depth of field

$$D_{of} = \frac{\lambda n}{NA^2} + \frac{n}{M\ NA} e \qquad A(11)$$

- Volume per frame

$$V_f = D_{of}\ H_{fov}\ V_{fov} \qquad A(12)$$

The volume in focus each frame can be compared to the volumetric flow rate, to provide an estimate on the frame rate required to image the objects in the system. Other factors, such as the peak linear velocity and rate of rotation, are not taken into account by this. Equation A13 was used as a sanity check rather than a fixed criteria, as each object will have a different velocity based on its position in the channel. In practice the system used a sensor with a higher frame rate than estimated by this equation.

- Estimated frame rate

$$f_{ps} = Q\ V_f \qquad A(13)$$

- exposure time

$$t = \frac{\frac{H_{fov}}{H_{res}}}{v_{max}} \qquad A(14)$$

An appropriate exposure time can be calculated as the time taken for an object to travel a distance corresponding to one pixel on the sensor. If the fastest moving objects in the system travel less than a pixel during the image exposure, the motion blur will be acceptable.

Appendix III Class Descriptions

Classes

Sequence Class

The sequence object is a container which holds the video sequence, the background image and the enhanced versions of the video sequence.

Properties

- *frameArray* – is the raw uncompressed image set from the input video sequence stored as a single channel greyscale image array (0-255).
- *width* – width of each image in pixels.
- *height* – height of each image in pixels.
- *length* – number of frames in the image sequence.
- *info* – all meta data associated with the AVI wrapper.
- *background* – frameArray(:,:,1), the first image in the sequence to be used as a background image.
- *binaryArray* – a binary version of frameArray.
- *subtractionArray* – array of foreground images derived from the frameArray.

Methods

- *constructor* – reads in the video sequence and populates the properties of the sequence object.
- *getSubtractionArray* – subtracts the background from each frame in the frameArray and stores in the subtractionArray. This method is called in the constructor.
- *getBinaryArray* – generates binary versions of the foreground images stored in the subtractionArray, using an adaptive threshold. This method is called in the constructor.

objectImage Class

The objectImage class is a container which holds all the properties, references and data associated with each blob detected in the data set.

Properties

- *picture* – A 256x256 window around the centroid location of the blob.
- *location* – The X, Y, Z coordinate of the blob in the image sequence.
- *wavelet* – level 5 stationary wavelet decomposition (biorthogonal 4.4) of the picture.
- *features* – Is a vector containing all the features associated with the blob.

- *particleNumber* – The particle number, that the blob belongs to.

Methods

There are no methods associated with the objectImage Class. All values are passed to the object when it is generated.

imageSetArray Class

The imageSetArray is a container for all the objectImages. This class finds each object images and constructs an array to contain them. A number of tools and techniques for examining the object images are also implemented in this class.

Properties

- *imageObjects* – An array of all objectImages found in the video sequence.
- *numberImages* – the number of objectImages which are present.
- *posWidthVector* – a vector of the X locations of each objectImage.
- *posHeightVector* – a vector of the Y locations of each objectImage.
- *posLengthVector* - a vector of the Z locations of each objectImage.
- *particleNumberVector* – a vector containing the associated particle number of each objectImage.

Methods

- *constructor* – Populates the imageObjects array with objectImages and their associated properties.
- *posVectors* – Populates the width, length, and height position vectors.
- *getParticleNumberVector* – Populates the particle number vector.
- *findPosLength* – Returns the length of the position vector for a given objectImage.
- *findParticleNumber* – Returns the particle number associated with a given objectImage.
- *graphPositions* – Plots the positions of the objectImages in the array in both 2D and 3D.
- *showparticleNumber* – Shows the particle number on the specified objectimage.

particle Class

Each physical object of interest viewed by the system will be imaged a number of times, each physical object will have a number of objectImages(blobs) associated with it. A ‘particle’ is a representation of a physical object of interest, as a number of images and their associated features. This object is a container for grouping all the objectImages of the same physical object of interest.

Properties

- *imageObjects* – An array of objectImages associated with the particle.
- *numberImages* – The number of objectImages in the particle.
- *zLocations* – A vector of the Z coordinates of the objectImages in the particle.
- *zLocationRange* – The range of Z coordinates of the objectImage in the particle.
- *fusion* – The wavelet recomposition of the maximum absolute values of the wavelet decompositions of each objectImage in the particle.

Methods

All properties of this class are passed to it upon creation by another object, similar to the objectImage class.

- *showParticle* – Displays the all the frames containing objectImages in the particle.

particleArray Class

A container for all of the particles in the sequence.

Properties

- *particleObjects* – An array of all the particles in the sequence.
- *numberParticles* – The number of particles in the sequence.

Methods

- *constuctor* – Populates the particleObjects array by generating particle objects from the objectImages in the sequence.
- *getParticles* – Called as part of the constructor.
- *cleanParticles* – Removes unwanted particles based on the number of objectImages in them.

Appendix IV Software

Real Time (Key sections only, full code to be included on disk)

Downsample and store frame

```
while (imDisp.test_and_set(std::memory_order_acquire))  // acquire
lock
    ;
dispFrame = acqFrame.clone();
imDisp.clear(std::memory_order_release);                // release
lock
newFrame2 = true;
prevAcqFrame = acqFrame.clone();
prevAcqFrameFlag = 1;

lrecFrame = passFrame.clone();

newFrame = false;

UMat copy = lrecFrame.clone();
Mat inbetween = copy.getMat(ACCESS_READ);
lstore = inbetween.clone();
inbetween.release();

//downsample current frame
resize(lrecFrame, lrecFrame, Size(), 0.25, 0.25, INTER_LINEAR);

//background subtraction, thresholding and morphological filtering
absdiff(lrecFrame, lbg, lsub);
threshold(lsub, lsub, 40, 255, 0);
morphologyEx(lsub, lsub, 2, lstrel);

//get intensity sum of remaining binary image
framesum = sum(lrecFrame).val[0];
int lforesum = sum(lsub).val[0];
cout << "ForeGround intensity : " << lforesum << endl;
cout << "thresh               : " << thresh << endl;

//save image if useful.
if (lforesum >= thresh)
{
    images.push_back(lstore);
    cout << "frame saved" << endl;
}
```

Display while running

```
//show image in parallel with main thread, see if channel blocked,
empty ect...
int parShowImage()
{
    int a;
    while (1)
    {
        if (newFrame2 == 1)
        {
            newFrame2 = false;
            while (imDisp.test_and_set(std::memory_order_acquire))  //
acquire lock
                ;
            showFrame = dispFrame.clone();
            imDisp.clear(std::memory_order_release);                //
release lock

            imshow("showFrame", showFrame);

        }
        a = cvWaitKey(30);
        if (a == 27)
        {
            exitAcq = true;
            break;
        }
        if (a == 61)
        {
            thresh = thresh + 5000; // up
        }
        if (a == 45)
        {
            thresh = thresh - 5000; //down
        }
    }
    return 0;
}
```

Store saved sequence

```
int writeVideo(void)
{
    VideoWriter outputVideo;
    const string NAME = "binary data test 3 .avi";
    Size S = Size(static_cast<int>(store.cols),
static_cast<int>(store.rows));
    //outputVideo.open(NAME, CV_FOURCC('F', 'L', 'V', '1'), 70, S,
false);
    outputVideo.open(NAME, -1, 70, S, false);
    //outputVideo.open(NAME, 0, 29, Size(400,400));


    cout << images.size() << endl;

    //write first chunk of video to disk
    int a;
    int b = 0;
    while (1)
    {
        imshow("image being written", images[b]);//
.getMat(ACCESS_READ));
        a = cvWaitKey(0);
        if (a == 27)
        {
            exitAcq = true;
            break;
        }
        if (a == 61)
        {
            b++;
            if (b > images.size()-1)
                b = images.size()-1;// up
        }
        if (a == 45)
        {
            b--;
            if (b < 0)
                b = 0;//down
        }
    }

    //if exceeding video size, write as images
    for (int a = 0; a < images.size(); a++)
    {
        if (a < 1200)
        {
            imshow("thingy", images[a]);//.getMat(ACCESS_READ));
            outputVideo.write(images[a]);// .getMat(ACCESS_READ));

            //sprintf_s(test, "image%d.bmp", a);
            //imwrite(test, images[a]);// .getMat(ACCESS_READ));
            cout << a << endl;
        }
        if (a > 1200)
```

```
        {
            char test[80];
            sprintf_s(test, "image%d.bmp", a);
            imwrite(test, images[a]);// .getMat(ACCESS_READ));
            cout << a << endl;
        }

        waitKey(20);
    }
    return 0;
}
```

Post Processing

Classes

Sequence

```
%%first attempt and object bassed approach to object detection and
%%identification

classdef sequence < handle
    properties (SetAccess = public)
        frameArray
        width
        height
        length
        info
        backGround
        binaryArray
        subtractionArray
        slit
        test
    end
    methods

        function obj = sequence
            fn = ''
            v = VideoReader(fn);
            info = aviinfo(fn)
            obj.info = info;
            obj.width = info.Width; %1280;
            obj.height = info.Height; % 1024;
            obj.length = info.NumFrames; %400;
            obj.frameArray = uint8(zeros(obj.height, obj.width,
obj.length)) ;
            i = 0;
            while (hasFrame(v) && i < obj.length)
                    i = i + 1;
                    obj.frameArray(:,:,i) = readFrame(v);
                    %obj.frameArray(:,:,i) = rgb2gray(readFrame(v));
                    %^ color vids
            end
            obj.backGround = (obj.frameArray(:,:,1));
```

```
            obj.getSubtractionArray
            obj.getBinaryArray
        end

        function getSubtractionArray(obj)
            obj.slit = (zeros(obj.height,obj.length));
            obj.subtractionArray = uint8(zeros(obj.height, obj.width,
obj.length));
            for i = 1:obj.length
                obj.subtractionArray(:,:,i) =
imcomplement(obj.frameArray(:,:,i)) - imcomplement(obj.backGround);
                obj.slit(:,i) = obj.subtractionArray(:,300,i);
            end
        end

        function getBinaryArray(obj)
            obj.binaryArray = logical(zeros(obj.height, obj.width,
obj.length));
            for i = 1:obj.length
                bw = imbinarize(obj.subtractionArray(:,:,i));
                obj.binaryArray(:,:,i) = bwareaopen(bw, 3000);
            end
            clear bw;
        end
    end
end
```

Image Set Array

```
classdef imageSetArray < handle
    properties
        imageObjects = objectImage
        numberImages
        posWidthVector
        posHeightVector
        posLengthVector
        particleNumberVector
    end

    methods
        function obj = imageSetArray(sequence)
            count = 0;
            for i = 1:sequence.length
                s = regionprops('table',
sequence.binaryArray(:,:,i),'centroid', 'orientation', 'eccentricity',
'Area', 'Convexarea', 'solidity', 'majoraxislength',
'minoraxislength');
                if length(s.Centroid) > 1
                    blobNumber = size(s.Centroid);
                    for j = 1:blobNumber(1)
                        count = count + 1;
                        obj.imageObjects(count) = objectImage;
                        obj.imageObjects(count).location =
[s.Centroid(j,1), s.Centroid(j,2), i];
```

```
                        if (s.Centroid(j,1) > 130) && (s.Centroid(j,1)
< (sequence.width -130)) && (s.Centroid(j,2) > 130) &&
(s.Centroid(j,2) < (sequence.height -130))
                            obj.imageObjects(count).picture =
sequence.subtractionArray(s.Centroid(j,2)-
127:s.Centroid(j,2)+128,s.Centroid(j,1)-127:s.Centroid(j,1)+128, i);
                            obj.imageObjects(count).bw =
sequence.binaryArray(s.Centroid(j,2)-
127:s.Centroid(j,2)+128,s.Centroid(j,1)-127:s.Centroid(j,1)+128, i);
                            obj.imageObjects(count).features = s;
%                             obj.imageObjects(count).picture;
obj.imageObjects(count).features.Orientation;
                            obj.imageObjects(count).pictureRotated =
imrotate(obj.imageObjects(count).picture,
obj.imageObjects(count).features.Orientation(1), 'crop');
                            obj.imageObjects(count).hasPicture = 1;
                        else
                            obj.imageObjects(count).picture =
zeros(256,256);
                            obj.imageObjects(count).pictureRotated =
obj.imageObjects(count).picture;
                            obj.imageObjects(count).hasPicture = 0;
                        end
                    end
                end
            end
            obj.numberImages = count;
            posVectors(obj)
            getParticleNumberVector(obj)
        end
        function posVectors(obj)
            for i = 1:obj.numberImages
                obj.posWidthVector(i) =
obj.imageObjects(i).location(1);
                obj.posHeightVector(i) =
obj.imageObjects(i).location(2);
                obj.posLengthVector(i) =
obj.imageObjects(i).location(3);
            end
        end
        function getParticleNumberVector(obj)
            for i = 1:obj.numberImages
                obj.particleNumberVector(i) =
obj.imageObjects(i).particleNumber;
            end
        end
        function ret = findPosLength(obj, n)
            ret = find(obj.posLengthVector == n);
        end
        function ret = findParticleNumber(obj, n)
            getParticleNumberVector(obj)
            ret = find(obj.particleNumberVector == n);
        end
        function ret = findNotParticleNumber(obj, n)
            getParticleNumberVector(obj)
            ret = find(obj.particleNumberVector ~= n);
        end
        function graphPositions(obj)
```

```
            figure;
            %subplot(2,1,1);
            %scatter3(obj.posWidthVector, obj.posHeightVector,
obj.posLengthVector);
            %title('3d scatter');
            %subplot(2,1,2);
            scatter(obj.posLengthVector, obj.posHeightVector);
            axis([0,450,100,800]);
            title('2d scatter');
        end
        function showParticleNumber(obj, sequence, i)
            textIn =
insertText(sequence.subtractionArray(:,:,obj.posLengthVector(i)),
[obj.posWidthVector(i),obj.posHeightVector(i)],
obj.imageObjects(i).particleNumber, 'TextColor', 'black', 'FontSize',
22);
            imshow(textIn);
        end
    end

end
```

```
classdef objectImage < handle
    properties
        picture
        pictureRotated
        bw
        hasPicture = 0;
        location
        wavelet
        waveletReshape
        waveletSum
        waveletMask                 %a binary mask of the components
from this image included in final
        features
        particleNumber = 0;
        level = 6;
    end

    methods
        function getWavelet(obj)
            obj.wavelet = swt2(double(obj.picture), obj.level,
'bior4.4');
            obj.waveletReshape = reshape(obj.wavelet, 1, []);
            obj.waveletSum = sumabs(obj.waveletReshape);
        end
    end


end
```

Particle

```
classdef particle < handle
    properties
        imageObjects = objectImage
        numberImages
        zLocations
        zLocationRange
        waveletSize
        waveletReshapeSize
        fusion
        iwtFusion
        waveletMax
        focusedImageIndex
        histA
        histB
    end

    methods
        function showParticle(obj, sequence)
            addition = 0;
            for i = 1:obj.numberImages
                addition = addition +
sequence.subtractionArray(:,:,obj.imageObjects(i).location(3));
            end
            figure,
            subplot(2,2,1), imshow(obj.fusion);
            subplot(2,2,2),
imshow(obj.imageObjects(obj.focusedImageIndex).picture);
            subplot(2,2,[3 4]), imshow(addition);
            %figure, imshow(addition);
        end
        function getFusion(obj)
             for i = 1:obj.numberImages
                 obj.imageObjects(i).getWavelet;
                 waveletStack(i,:) =
obj.imageObjects(i).waveletReshape;
             end

             [trash, I] = max(abs(waveletStack), [], 1);

             [obj.histA, obj.histB] = hist(I, unique(I))

             fusionHolder = waveletStack(sub2ind(size(waveletStack),
I, (1:256*256*(obj.imageObjects(1).level*3+1))));

             obj.iwtFusion =reshape(I, 256, 256,
obj.imageObjects(1).level*3+1);

             waveletfusion = reshape(fusionHolder, 256, 256,
obj.imageObjects(1).level*3+1);
             obj.fusion = iswt2(waveletfusion, 'bior4.4')/255;

             [obj.waveletMax obj.focusedImageIndex] =
max([obj.imageObjects.waveletSum]);
```

```
            for i = 1:obj.numberImages
                obj.imageObjects(i).waveletMask =
fusionMask(obj.iwtFusion, i);
            end
        end
    end
end
```

Particle Array

```
classdef particleArray < handle
    properties
        particleObjects = particle
        numberParticles

    end

    methods
        function obj = particleArray(imageArray, sequence)
            localParticleNumber = 0;
            for i = 1:imageArray.numberImages
                if (imageArray.imageObjects(i).particleNumber == 0)
                    localParticleNumber = localParticleNumber + 1;
                    imageArray.imageObjects(i).particleNumber =
localParticleNumber;
                    localDepth =
imageArray.imageObjects(i).location(3);
                    lookingDepth = localDepth + 1;
                    frameFound = 1;
                    compReference = i;
                    while(frameFound == 1)
                        frameFound = 0;
                        optionImageReferences =
imageArray.findPosLength(lookingDepth);
                        optionImageReferencesCopy =
optionImageReferences;
                        while(length(optionImageReferencesCopy) > 0)
                            for j = 1:length(optionImageReferences)
                                if
(imageArray.imageObjects(optionImageReferences(j)).particleNumber ==
0)
                                    heightDif =
imageArray.posHeightVector(compReference) -
imageArray.posHeightVector(optionImageReferences(j));
                                    widthDif =
imageArray.posWidthVector(compReference) -
imageArray.posWidthVector(optionImageReferences(j));
                                    if(heightDif < 70) && (heightDif >
-70) && (widthDif < 0) && (widthDif > -400)% swapped 0 and 300 for
testing

imageArray.imageObjects(optionImageReferences(j)).particleNumber =
localParticleNumber;
                                        frameFound = 1;
                                        optionImageReferencesCopy =
optionImageReferencesCopy(optionImageReferencesCopy~=optionImageRefere
nces(j));
                                        compReference =
optionImageReferences(j);
                                    else
                                        optionImageReferencesCopy =
optionImageReferencesCopy(optionImageReferencesCopy~=optionImageRefere
nces(j));
                                    end
```

```
                                    else
                                        optionImageReferencesCopy =
optionImageReferencesCopy(optionImageReferencesCopy~=optionImageRefere
nces(j));
                                    end
                                end
                            end
                            lookingDepth = lookingDepth + 1;
                        end
                    end
                end
                getParticles(obj, imageArray)
                cleanParticles(obj)
                obj.numberParticles = length(obj.particleObjects);
                getWavelets(obj, sequence)
            end
            function getParticles(obj, imageArray)
                imageArray.getParticleNumberVector
                for i = 1:max(imageArray.particleNumberVector)
                    obj.particleObjects(i) = particle;
                    count = 0;
                    for j = 1:imageArray.numberImages
                        if (imageArray.imageObjects(j).particleNumber ==
i)
                            count = count + 1;
                            obj.particleObjects(i).imageObjects(count) =
imageArray.imageObjects(j);
                        end
                    end
                    obj.particleObjects(i).numberImages = count;
                end
            end
            function cleanParticles(obj)
                i = 1;
                deleted = 0;
                while (i <= length(obj.particleObjects))
                   if (obj.particleObjects(i).numberImages <= 5)
                       obj.particleObjects(i) = [];
                       deleted = deleted + 1;
                   else
                   i = i+1;
                   end
                end
                deleted
            end
            function getWavelets(obj, sequence)
               for i = 1:obj.numberParticles
                   obj.particleObjects(i).getFusion
%                    figure, imshow(obj.particleObjects(i).fusion);
%                    obj.particleObjects(i).showParticle(sequence);
               end
        end
    end
end
```

Fusion mask

```
function [ arrayOut ] = fusionMask(waveletFusion, objectImageNumber)
%Takes a 2d fusion in, returns a binary mask of the coefficients


a = waveletFusion;
s = size(a);
b = [];
for i = 1:s(1)
    for j = 1:s(2)
        if a(i,j) == objectImageNumber
            b(i,j) = 1;%(a(i,j));
        else
            b(i,j) = 0;
        end
    end
end
arrayOut = b;

end
```

Find Focus

```
function [i1 i2 sumsum areas] = findFocus(pn, particles)
%this function returns the index of the most focused image in the
stack by two metrics
%it also returns arrays for focus and area
index = [];
sumsum = [];
imdisp = [];
areas = [];
se = strel('square', 5);
for i = 1:particles.particleObjects(pn).numberImages
    if particles.particleObjects(pn).imageObjects(i).hasPicture == 1
        bwmask =
imdilate(particles.particleObjects(pn).imageObjects(i).bw, se);
        test =
particles.particleObjects(pn).imageObjects(i).waveletMask.*bwmask;
        index = [index i];
        sumsum = [sumsum sum(sum(test))];
        areas = [areas
particles.particleObjects(pn).imageObjects(i).features.Area(1)];
        %figure, imshow()
%         imdisp = cat(2, imdisp,
particles.particleObjects(pn).imageObjects(i).picture);
    end
end

for i = 2:4:particles.particleObjects(pn).numberImages-1
    if particles.particleObjects(pn).imageObjects(i).hasPicture == 1
        imdisp = cat(2, imdisp,
particles.particleObjects(pn).imageObjects(i).picture);
    end
end
[m i] = max(sumsum);
i1 = index(i);                          %This is the image with the most
elements in the fused image
[m2 i2] = max(sumsum./areas);
i2 = index(i2);                         %image with most elements over
most area
%
imshow(particles.particleObjects(pn).imageObjects(index(i)).picture);
figure
subplot(4,1,1)
plot(sumsum)
title('number of points in fused image')
subplot(4,1,2)
plot(areas)
title('area of binary image')
subplot(4,1,3)
plot(sumsum./areas)
title('area of binary image / number of points in fused image')
subplot(4,1,4)
imshow(imdisp)
title('raw images without background')

end
```

Appendix V PCBS

Annular Light

Schematic

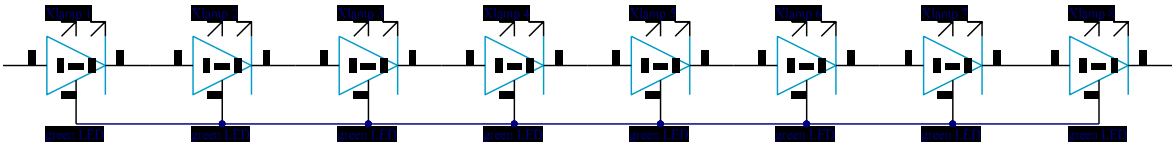

Layout

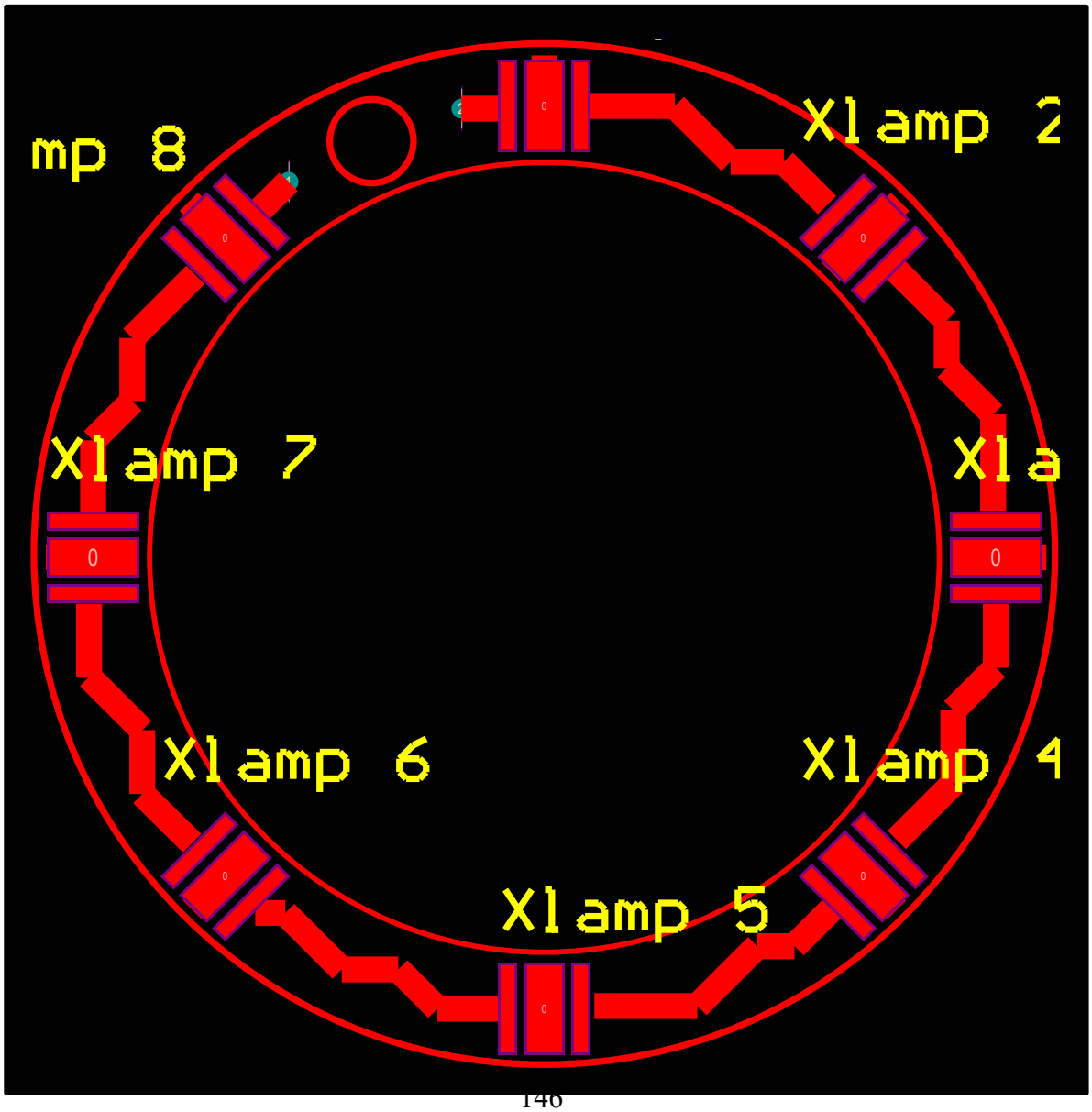

Direct Lighting

Schematic

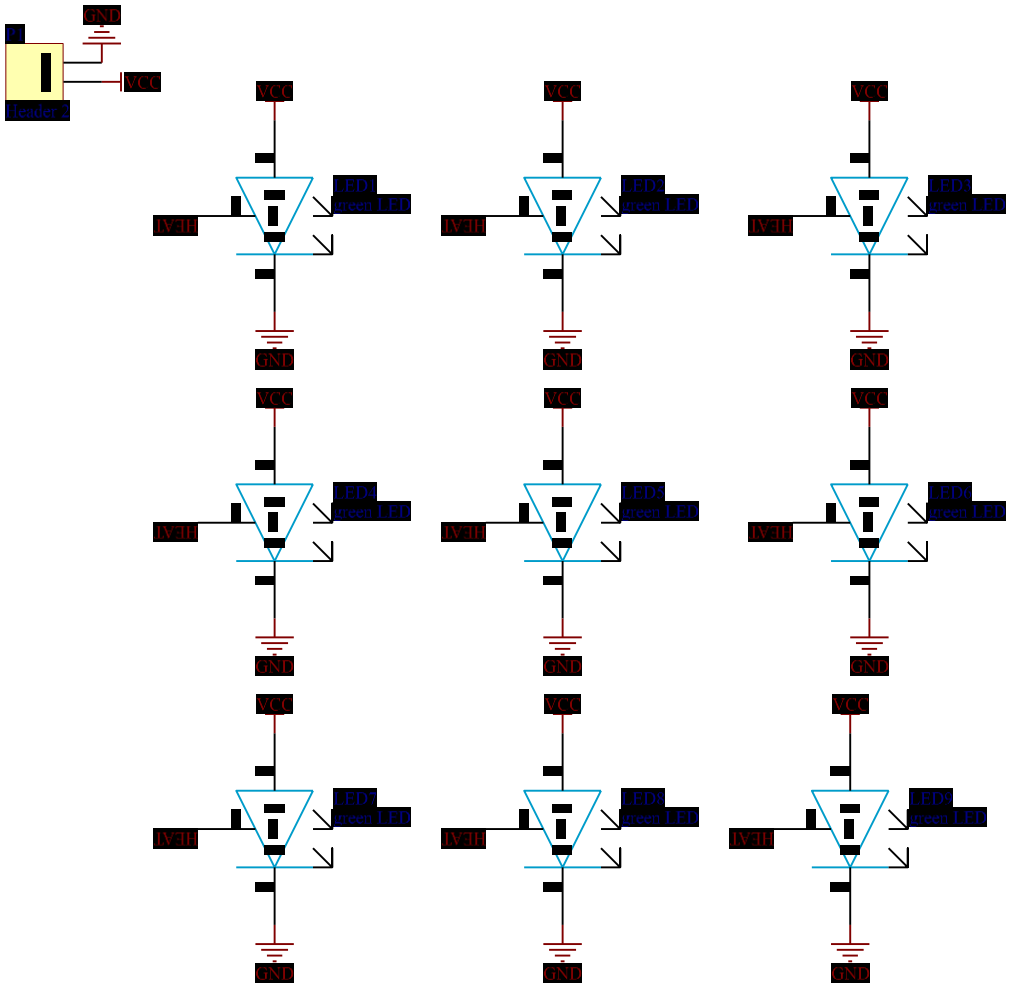

Layout

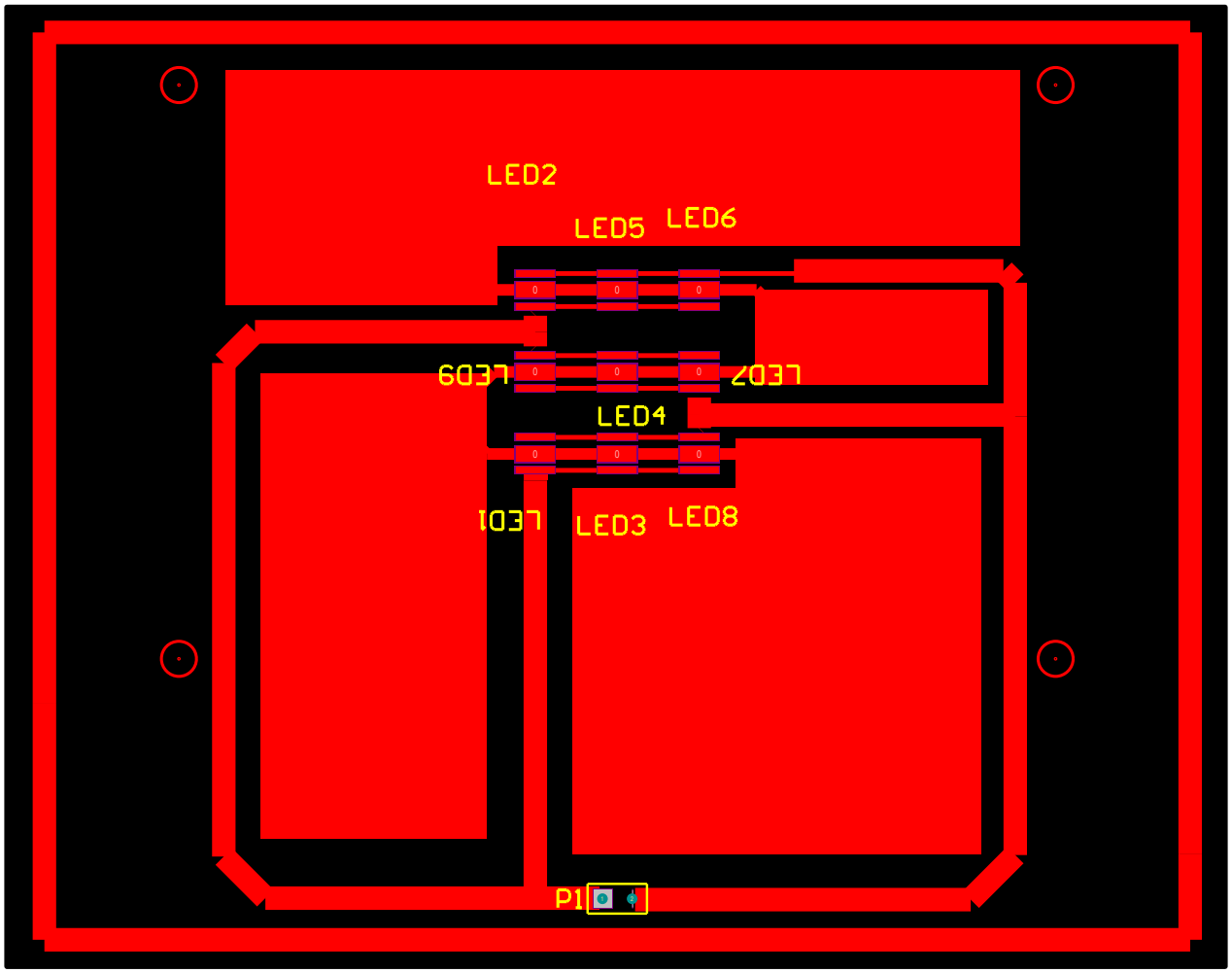

Schematic

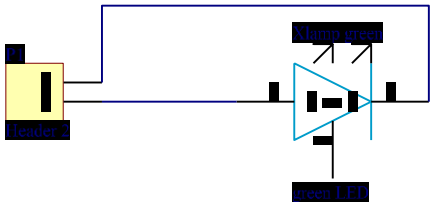

Layout

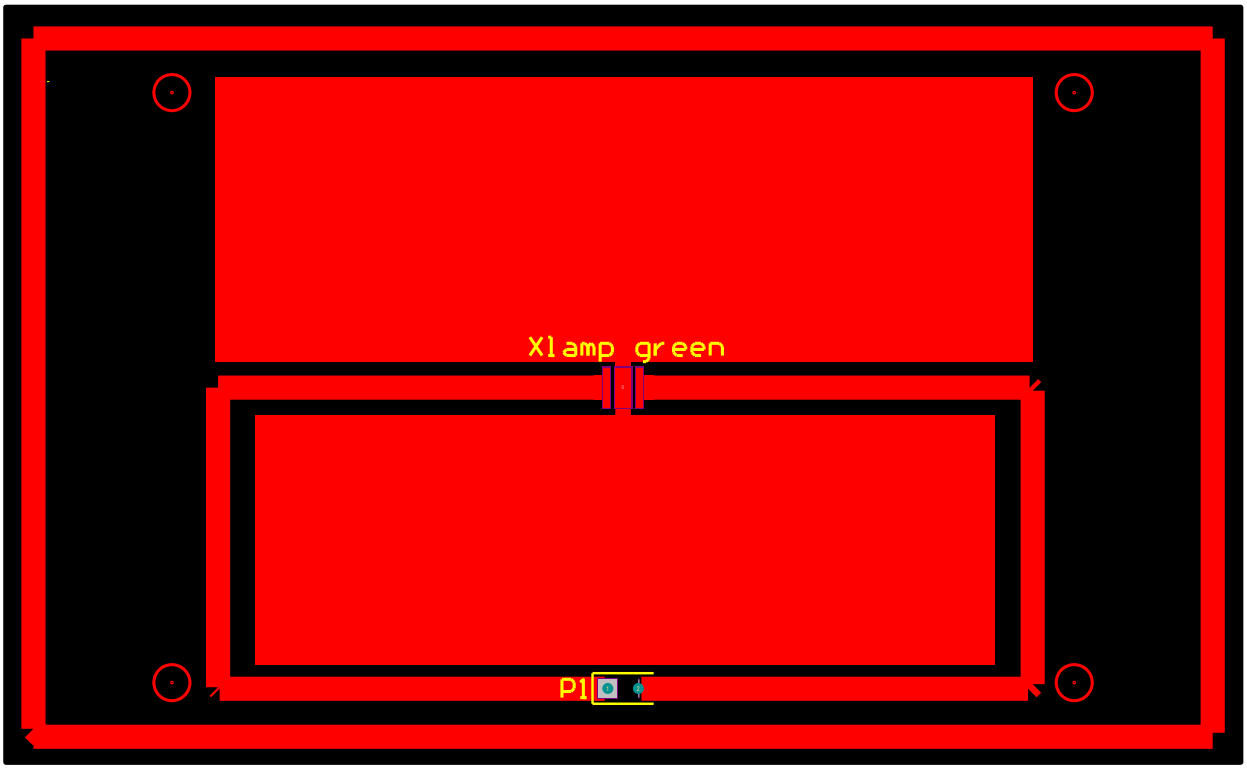

Appendix VI System Outputs

Feature Histograms

The features extracted from the different systems were normalised for sample size and presented as a histogram, so a comparison of range and value can be made visually. Features extracted from the presented system are in blue, conventional slide images are orange.

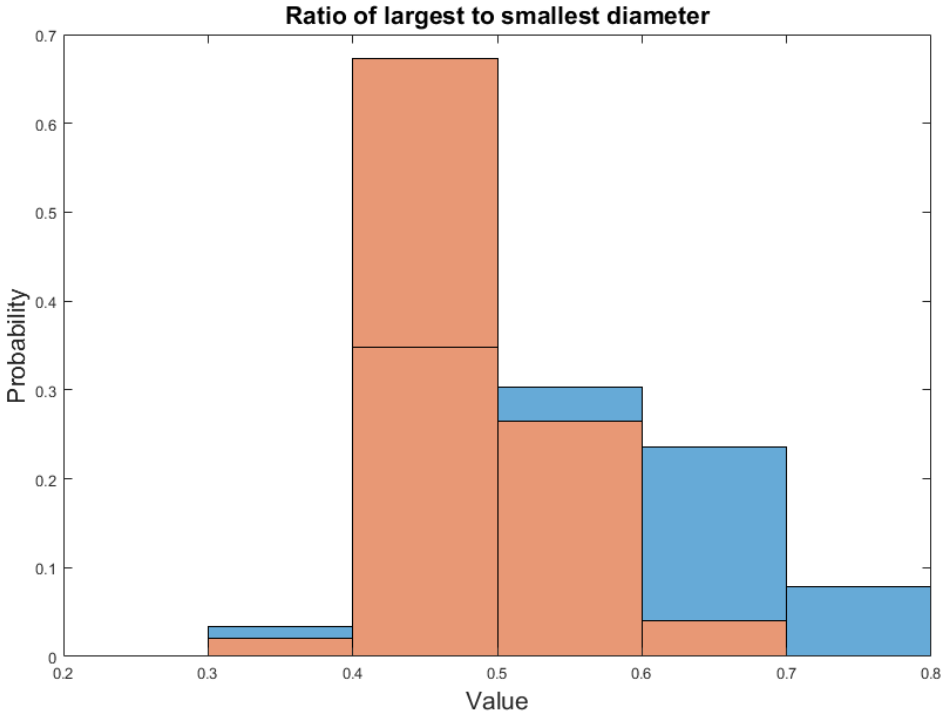

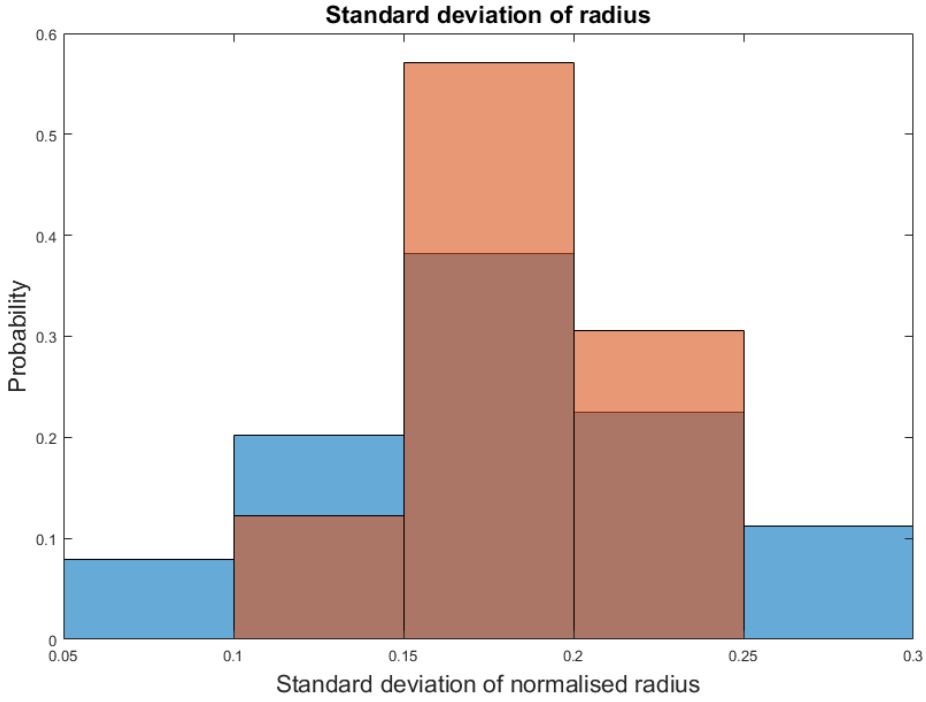
Standard deviation of radius
Probability
0.6
0.5
0.4
0.3
0.2
0.1
0
0.05
0.1
0.15
0.2
0.25
0.3
Standard deviation of normalised radius

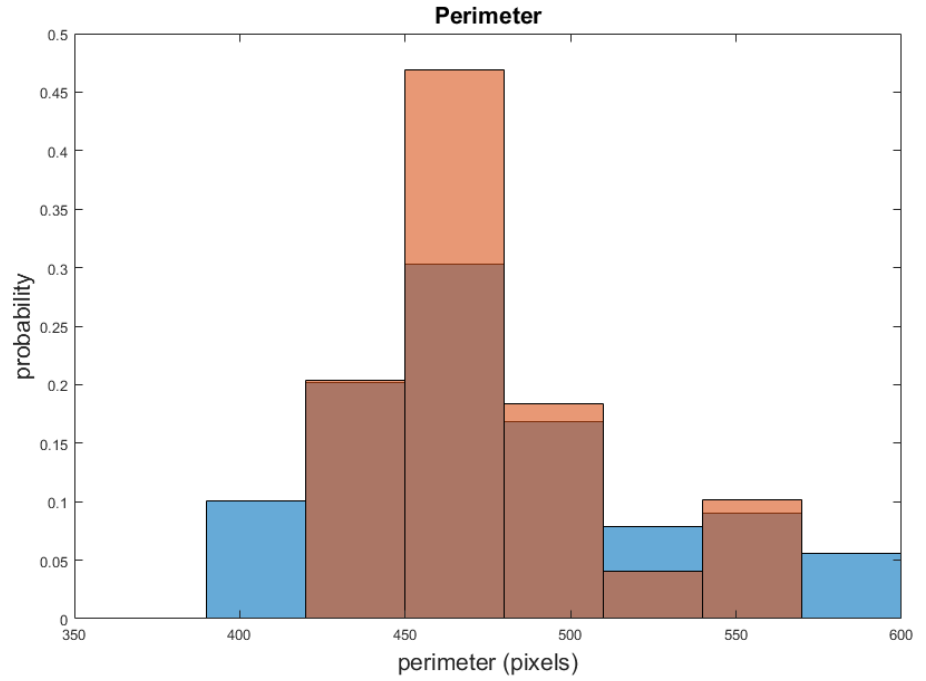
Perimeter
probability
0.5
0.45
0.4
0.35
0.3
0.25
0.2
0.15
0.1
0.05
0
350
400
450
500
550
600
perimeter (pixels)

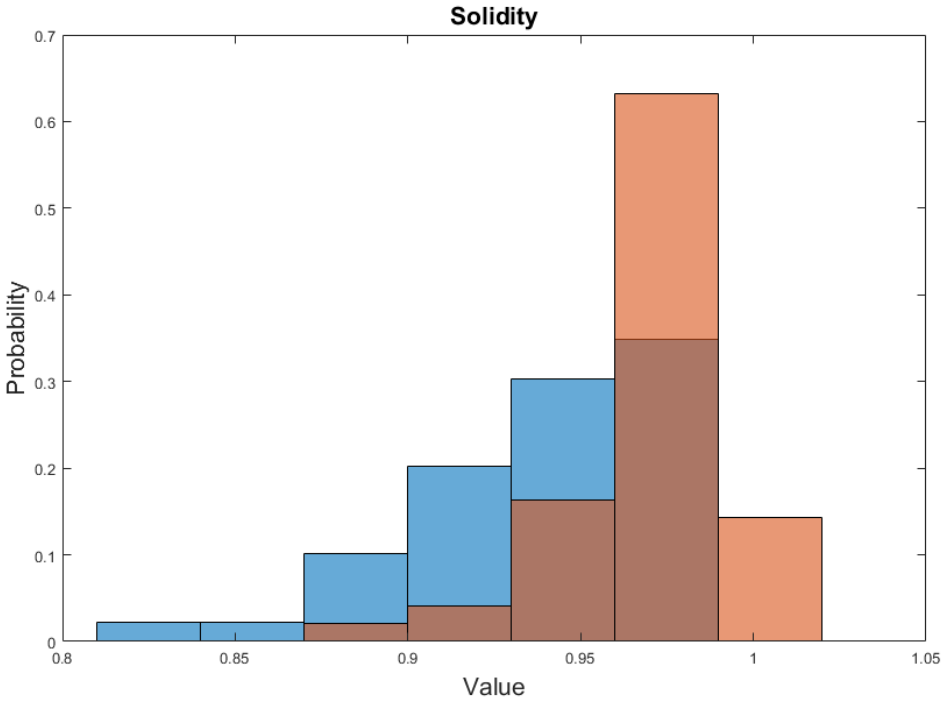
Solidity
Probability
Value
0.7
0.6
0.5
0.4
0.3
0.2
0.1
0
0.8
0.85
0.9
0.95
1
1.05

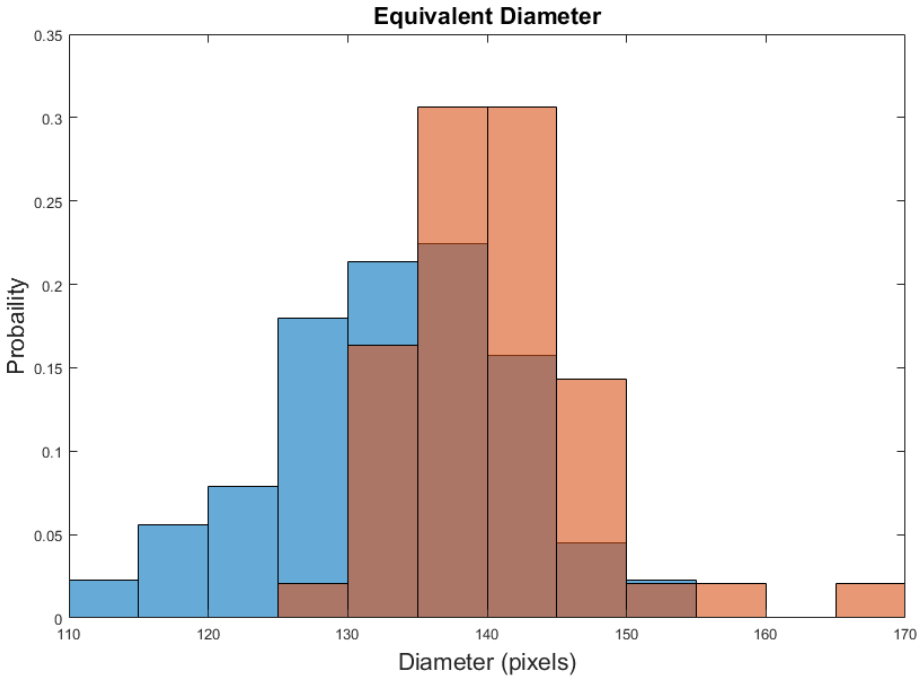
Equivalent Diameter
Probaility
Diameter (pixels)
0.35
0.3
0.25
0.2
0.15
0.1
0.05
0
110
120
130
140
150
160
170

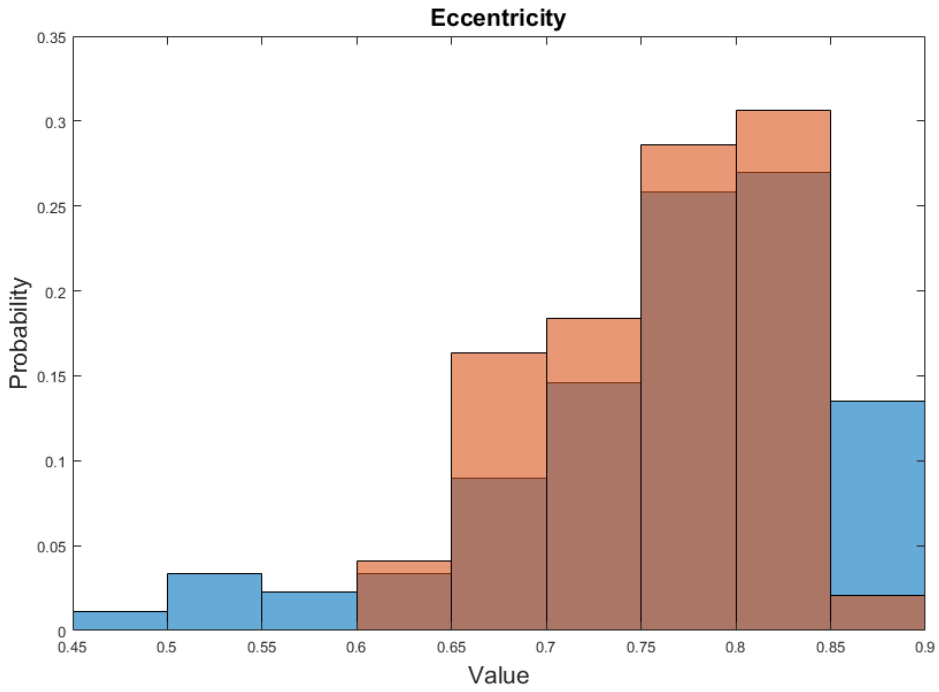
Eccentricity
Probability
Value
0.35
0.3
0.25
0.2
0.15
0.1
0.05
0
0.45
0.5
0.55
0.6
0.65
0.7
0.75
0.8
0.85
0.9

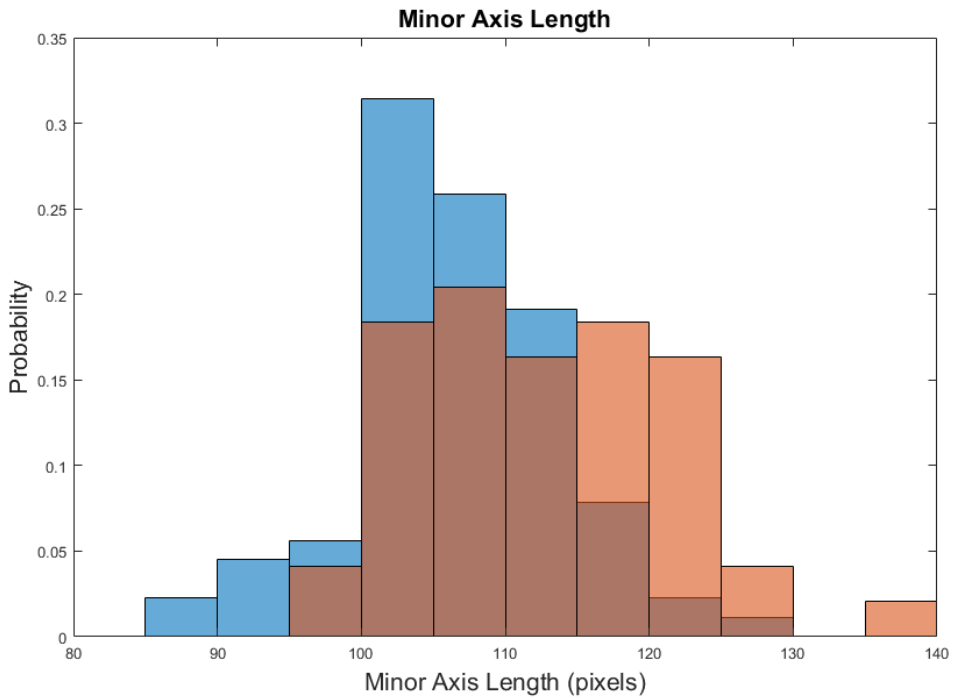
Minor Axis Length
Probability
Minor Axis Length (pixels)
0.35
0.3
0.25
0.2
0.15
0.1
0.05
0
80
90
100
110
120
130
140

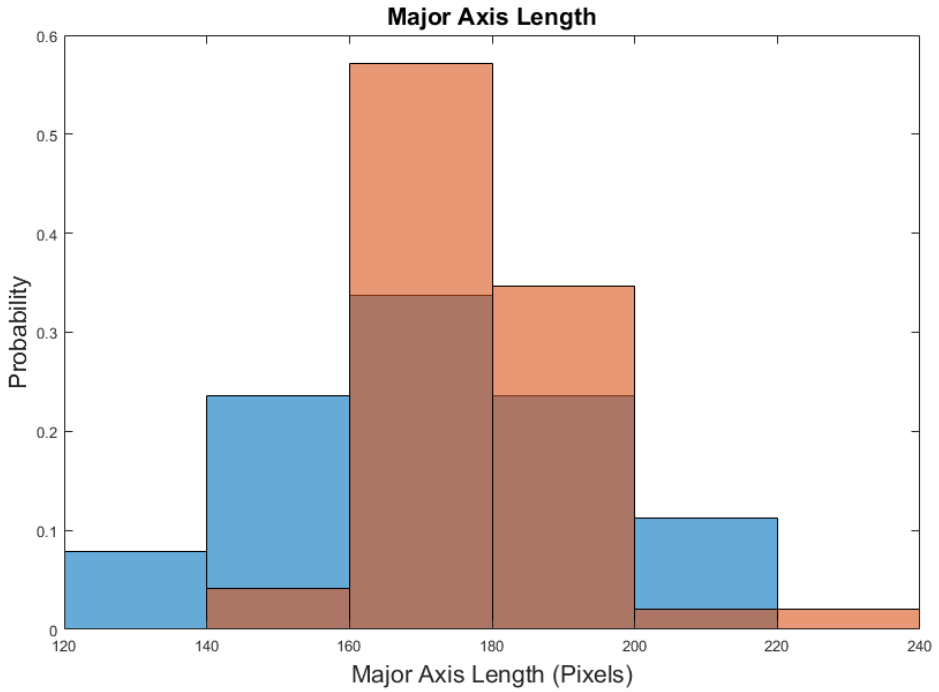
Major Axis Length
Probability
0.6
0.5
0.4
0.3
0.2
0.1
0
120
140
160
180
200
220
240
Major Axis Length (Pixels)

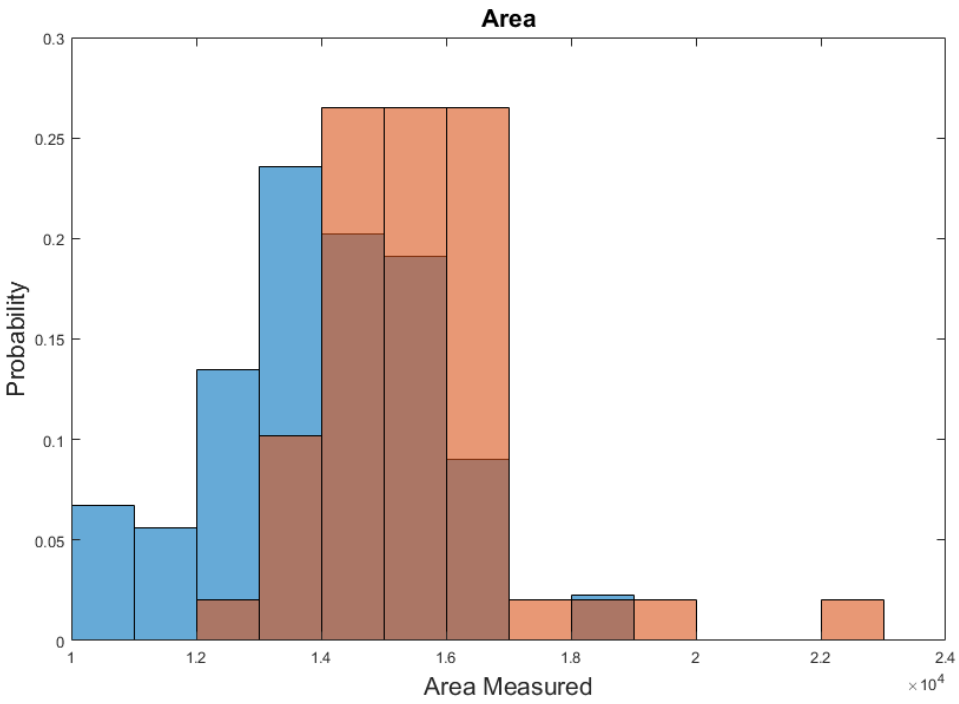
Area
Probability
0.3
0.25
0.2
0.15
0.1
0.05
0
1
1.2
1.4
1.6
1.8
2
2.2
2.4
Area Measured
×10^4

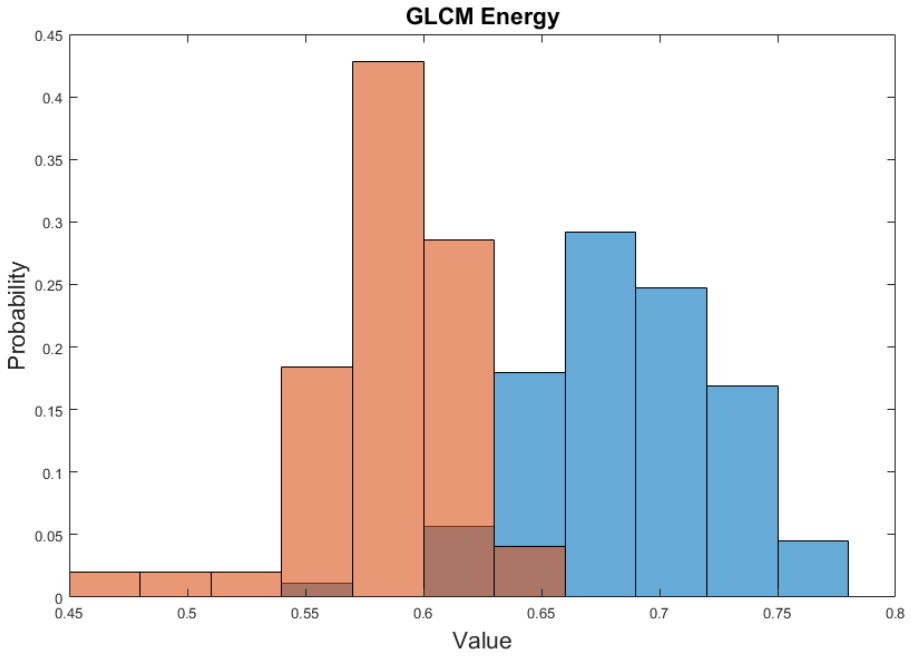
GLCM Energy
Probability
Value
0.45
0.4
0.35
0.3
0.25
0.2
0.15
0.1
0.05
0
0.45
0.5
0.55
0.6
0.65
0.7
0.75
0.8

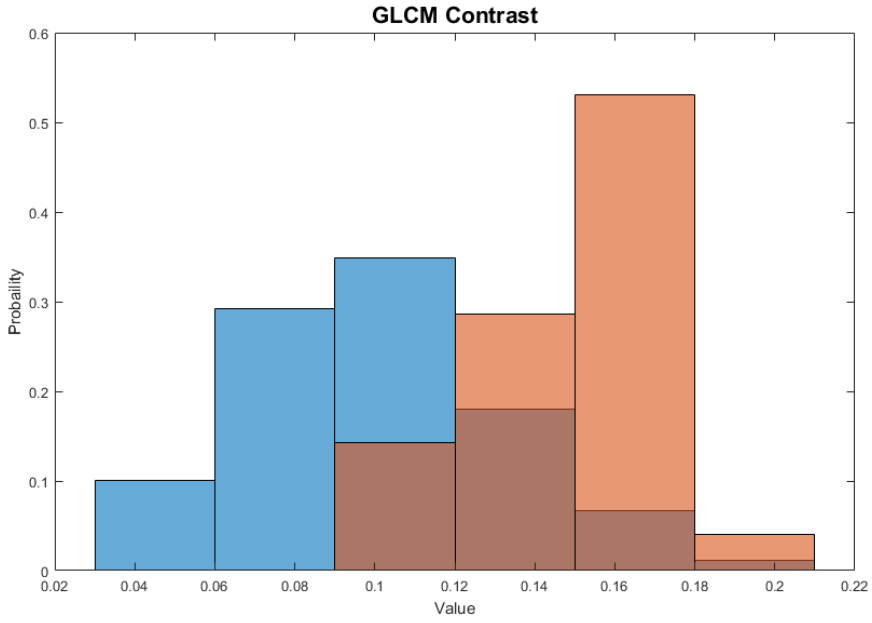
GLCM Contrast
Probaility
Value
0.6
0.5
0.4
0.3
0.2
0.1
0
0.02
0.04
0.06
0.08
0.1
0.12
0.14
0.16
0.18
0.2
0.22

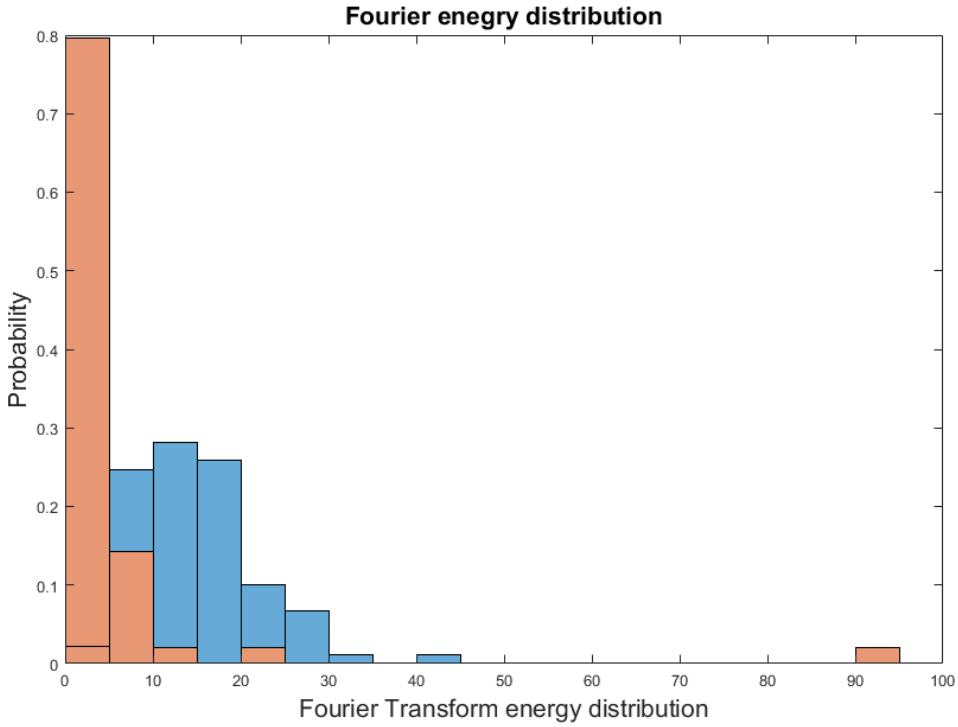
Fourier enegry distribution
Probability
Fourier Transform energy distribution
0
0.1
0.2
0.3
0.4
0.5
0.6
0.7
0.8
0
10
20
30
40
50
60
70
80
90
100

Sample Images